University of Alberta

Unsteady Spatially Varying Flow Control

I. 'Void' Structure in the Wake of a Self-Oscillating Flexible Cylinder
II. Design of a Backward-Facing Step Control Device

by

Stuart Karl Gilbert ©

A thesis submitted to the Faculty of Graduate Studies and Research
in partial fulfillment of the requirements for the degree of

Master of Science

Department of Mechanical Engineering

Edmonton, Alberta
Fall 2007

Library and
Archives Canada

Published Heritage
Branch

395 Wellington Street
Ottawa ON K1A 0N4
Canada

Bibliothèque et
Archives Canada

Direction du
Patrimoine de l'édition

395, rue Wellington
Ottawa ON K1A 0N4
Canada

Your file Votre référence
ISBN: 978-0-494-33247-4
Our file Notre référence
ISBN: 978-0-494-33247-4

NOTICE:
The author has granted a non-exclusive license allowing Library and Archives Canada to reproduce, publish, archive, preserve, conserve, communicate to the public by telecommunication or on the Internet, loan, distribute and sell theses worldwide, for commercial or non-commercial purposes, in microform, paper, electronic and/or any other formats.

The author retains copyright ownership and moral rights in this thesis. Neither the thesis nor substantial extracts from it may be printed or otherwise reproduced without the author's permission.

AVIS:
L'auteur a accordé une licence non exclusive permettant à la Bibliothèque et Archives Canada de reproduire, publier, archiver, sauvegarder, conserver, transmettre au public par télécommunication ou par l'Internet, prêter, distribuer et vendre des thèses partout dans le monde, à des fins commerciales ou autres, sur support microforme, papier, électronique et/ou autres formats.

L'auteur conserve la propriété du droit d'auteur et des droits moraux qui protège cette thèse. Ni la thèse ni des extraits substantiels de celle-ci ne doivent être imprimés ou autrement reproduits sans son autorisation.

In compliance with the Canadian Privacy Act some supporting forms may have been removed from this thesis.

While these forms may be included in the document page count, their removal does not represent any loss of content from the thesis.

Conformément à la loi canadienne sur la protection de la vie privée, quelques formulaires secondaires ont été enlevés de cette thèse.

Bien que ces formulaires aient inclus dans la pagination, il n'y aura aucun contenu manquant.

Canada

Reproduced with permission of the copyright owner. Further reproduction prohibited without permission.

Mistakes are the portal to discovery

James Joyce
Irish Author
(1882-1941)

To Kimberley and Isaac, whom I dearly love…

Abstract

This thesis concerns unsteady flow control in two different flow geometries. The first is an experimental study involving the discovery of a new large scale vortex “void” structure in the wake of cylinder undergoing vortex induced vibration that includes vortex pinch-off. We simulated the vibration of this cylinder from measurements of shedding frequency and cylinder tension. The structure’s span-wise location is correlated with an anti-node in the transverse vibration and a node in the stream-wise vibration. Hydrogen bubble flow visualization is shown to be well suited for cylinder research, as the bubbles directly visualize the vortex structure when they become trapped in the low pressure cores of the vortex street. Bubbles do not affect well known cylinder shedding and vibration characteristics. The second flow geometry involves the design and construction of a backward-facing step flow control device which, in addition to all other desirable characteristics, is capable of span-wise varying actuation not previously studied experimentally.

Preface

This thesis presents data from two research projects in unsteady flow control for two fundamentally different geometries. The first topic is related to the accidental discovery of a new large scale structure found in the wake of a rigidly mounted flexible cylinder undergoing vortex induced vibration. The second topic is the design of a backward-facing step control device with actuation attributes that are not yet experimentally implemented, which first choice for a masters project.

In the summer of 2004, my tenure at the University of Alberta started as a research assistant in the Vortex Fluid Dynamics Laboratory under the supervision of Dr. Sigurdson. During this time, I was asked to quantify the turbulence intensity value of the recently re-commissioned high speed flow visualization water tunnel. Shedding of the cylinder, which also acted as the electrolysis electrode, was allowed by mistake and we visualized the large scale 'void' vortex structure. A photograph of this structure received special attention at the American Physical Society Division of Fluid Dynamics meeting in Seattle in November 2004. This photograph ended up in the September 2005 edition of the Physics of Fluids Gallery of Fluid Motion. Encouraged by this result, Dr. Sigurdson offered me the opportunity to study this structure further and make this the focus of my masters degree. I decided to maintain the course toward completion of my backward-facing step flow control research having overly optimistic ideas about timelines for design, fabrication and experimentation while also working on a paper to report the information we know about the 'void'.

Due to the complexity of the design and usual complications of fabrication, the second year of my masters quickly passed. With loved ones moved from Edmonton and the side effects of being a long distance parent being ever prominent I decided to study the 'void' structure more completely. Hence, I have written a thesis in paper format based on data from a simply designed flexible cylinder experiment, and the mostly fabricated back step flow control pro

Acknowledgement

I would like to thank the Natural Sciences and Engineering Research Council (NSERC), for the CGS-M scholarship which supported me during my program. For the cylinder vibration project, Cessco Fabrication and Engineering Ltd., Andrew Coward, Terry Nord and Bernie Faulkner are gratefully acknowledged for their support. Special thanks to Charles Williamson for suggesting cylinder surface irregularities might serve as a perturbation and Ryan Tucker for his design of flexible wire support with controllable tension.

For the backward-facing step project, I would like to thank everyone in the Mechanical Engineering Machine shop, with special thanks to Rick Bubenko, Roger Marchand and Greg Miller whose help in the fabrication process was greatly appreciated.

Finally, I would like to thank my supervisor Dr. Lorenz Sigurdson whose enlightened methods and teaching will help shape my future engineering practice.

Contents

List of Tables

Chapter 3. Design of a Backward-Facing Step Control Device

List of Figures

Chapter 2. 'Void' Structure in the Wake of a Self-Oscillating Circular Cylinder

Chapter 3. Design of a Backward-Facing Step Control Device

Appendix A1: Derivation of Wave Equation Models for Vibration

Appendix B: Unsteady Bernoulli Equation and Fluid Dynamic Similarity

List of Symbols and Abbreviations

I. Vortex Induced Vibration of a Flexible Cylinder

A	Cylinder cross sectional area
A_y/D	Normalized peak transverse vibration Amplitude
A_z/D	Normalized peak stream-wise vibration Amplitude
c	Wave speed
C_A	Added mass coefficient
D	Wire diameter
D_b	Bubble Diameter
F_{dl}	Force transfer component for forces out of phase with cylinder motion
F_{ml}	Force transfer component for forces in phase with cylinder motion
F_y	Transverse oscillating forces
F_z	Stream-wise oscillating forces
f_{ex}	In water cylinder response frequency
f_n	Cylinder in water natural frequency (Hz)
f_s	Stationary cylinder shedding frequency
f_{vac}	In vacuum cylinder response frequency
f_{vs}	Vibrating cylinder shedding frequency
g	gravitational constant
L	span-wise length of cylinder
m^*	mass ratio of cylinder
n	mode index

T	applied cylinder tension
U_{bt}	terminal bubble velocity
U_c	vortex convection velocity
U_∞	mean tunnel velocity
V	bubble rise velocity
$w_y(x,t)$	transverse vibration distribution
$w_z(x,t)$	stream-wise vibration distribution
$X_n(x)$	mode shape function
x,y,z	co-ordinate system
X_{dl}	peak amplitude as calculated for F_{dl}
X_{ml}	peak amplitude as calculated for F_{ml}
x_t	void tolerance
$\Delta\rho$	density difference between water and hydrogen
$\Delta\rho_f$	added mass per unit area
γ_y γ_z	damping coefficients
λ	Karman vortex street wavelength
μ	water dynamic viscosity
ρ ρ_c	cylinder density
$\xi_{n,y,z}$	damping ratios
$\theta_{n,y,z}$	damping induced phase difference between forcing and cylinder motion
ω_n	cylinder in water angular velocity
ω_{vs}	angular velocity of vortex shedding

Subscripts

n	nth mode
y	transverse component
z	stream-wise component

Abbreviations

H_2	Hydrogen
ICV	Image Correlation Velocimetry
VIV	Vortex Induced Vibration

List of Symbols and Abbreviations

II. Design of a Backward-Facing Step Control Device

Symbols

a	wavelength coefficient L_z=ah
AR	Step Aspect Ratio
A_v	Peak angular velocity of servo
A_v^*	Normalized peak angular velocity of servo using the desired peak velocity
b	Number of wavelengths
c	Branch flow fraction
$C_{zp}(t)$	Number of slots in span-wise phase
D_A	Syringe piston diameter
D_j	j^{th} tubing network component diameter
ds	infinitesimal streamline length
ER	Step Expansion Ratio
f	Actuation frequency $\omega=2\pi f$
f^*	Normalized actuation frequency of servo using the desired frequency
f_h	Step mode instability frequency
f_θ	Shear layer mode instability frequency
h	Step height
L	Step span
$l_1, l_2, l_3, \theta_1, \theta_2$	linkage lengths and angles
L_a	Actuated span

L_j	j^{th} tubing network component length
L_z	Actuated span-wise wavelength
$L_{z,o}$	Fundamental span-wise actuation wavelength
n	Wave number, $L_z=nL_{z,o}$
N_f	Number of frequencies for multiple frequency forcing
P(t)	Time dependent actuation pressure in tubing network
Re_h	Reynolds number based on diameter
Re_θ	Reynolds number based on momentum thickness
R_{wave}	Resolution of span-wise wavelength
R_{zp}	Resolution of span-wise time varying phase
St_h	Strouhal number based on diameter
St_θ	Strouhal number based on momentum thickness
U_∞	Bulk tunnel flow velocity just upstream of separation
V(t)	Time dependent actuation velocity in tubing network
$V_A(t)$	Piston velocity
$V_{A,peak}$	Peak piston velocity
V_j	j^{th} tubing network component velocity
W_a	With of an actuation slot includes slot width and wall thickness
x,y,z	stream-wise, transverse and span-wise coordinate
X_R	Reattachment length
y_A, y_r, y_{tn}	Distances from the HSWT free surface as used in the Bernoulli Equation model
$z_p(t)$	Time varying span-wise phase

ρ	water density
ν	water kinematic viscosity
θ	Momentum thickness
$\theta(t), \dot{\theta}(t)$	angular position and velocity of servo motor
θ_{peak}	Peak angular position of servo motor
ϕ	Multiple frequency forcing phase

Subscripts

A	actuator quantity
j	tubing component index
r	extra tube reservoir quantity
RMS	root mean square of quantity
s	step quantity
tn	bulk flow quantity

Abbreviations

DAL	Discrete Actuation Location
FTS	Force Transmission System
ID	Inner Diameter
MEMS	Micro-Electro-Mechanical Systems
OD	Outer Diameter
SMA	Shape Memory Alloys
THD	Total Harmonic Distortion

Chapter 1. Introduction

The topic of unsteady flow control encompasses a wide variety of topics in Fluid Mechanics. A review of this immense literature is found in the review text of Gad-el-Hak (2000). Two such areas of flow control, which are the focus of the present discussion, are the control of the formation of large scale structures in the cylinder wake and the control of coherent structures which exist in reattaching shear layers behind a backward-facing step.

Although there are vast differences in the theory and research behind these two topics, we can draw certain similarities. Firstly, both topics involve open loop control schemes for controlling the vortex dynamics of the respective flows. For the oscillating cylinder flow the desired vortex dynamics in the cylinder wake correspond to the formation of a unique large scale vortex structure. For the backward-facing step flow the desired control objective is to promote the merging of shear layer vortices. This has the advantage of promoting rapid growth of the shear layer which in turn promotes enhanced mixing behind the step and reduces the length of the recirculation region. Control schemes for enhanced mixing would be of value in increasing the efficiency of ramjet combustors in aircraft.

One must determine the control variables that can be best manipulated to meet such a desired objective efficiently, consistently and with minimal control effort. For the oscillating cylinder wake we have two highly significant control variables. The first is the frequency of vortex shedding, which is dependent on the Reynolds number of the flow and can be manipulated simply by changing the bulk flow velocity. The second control variable is the fundamental and harmonic natural frequencies of the flexible cylinder response. This is controllable by applying a given tension value to the flexible cylinder. These two control variables must be set to very specific values in order to meet our desired control objectives.

The control variables used to promote vortex merging of the reattaching shear layer vortices of a backward-facing step flow are much more varied. The most influential control variable known to date is the frequency content of open loop forcing. If one does not use an optimal forcing frequency, the effectiveness of the control is greatly inhibited and very large amplitude actuations are required to create the same effect. While also being able to modify amplitudes and the frequencies of forcing, our control device is designed to explore the effects of adding a wide variety of span-wise variations of actuation to the control. Such actuations should energize the reattaching shear layer with all three components of vorticity to promote better mixing than just span-wise uniform forcing at optimum frequencies alone. After research on the backward-facing step is completed, the legacy of span-wise variation of actuation can be applied to numerous other flow geometries as the actuator is portable.

This thesis is written in paper format as defined by the Faculty of Graduate Studies at the University of Alberta. Chapter 2 describes the discovery of a new large scale vortex structure that we call a 'void' and the unique conditions for its formation. Chapter 3 discusses the design of the backward-facing step control device and its unique specifications and potential contributions to the existing literature. In Chapter 4, we summarize all conclusions from these two research studies into unsteady flow control.

References

Gad-el-Hak M (2000) Flow Control: Passive, Active, and Reactive flow management. Cambridge University press, Cambridge, UK.

Chapter 2. 'Void' Structure in the Wake of a Self-Oscillating Circular Cylinder[1]

2.1 Introduction

The study of vortex induced vibration (VIV) has seen much research over the years. The reader is referred to the text of Blevins (1990) and the review papers of Williamson and Govardhan (2004) and Sarpkaya (2004) for an in-depth review on the topic. From these reviews it is seen that the large majority of research into VIV cylinder flows is done for flexibly mounted rigid cylinders at high Reynolds numbers, based on diameter (Re_D). Only a few studies have been devoted to the study of low Re_D VIV of rigid and flexible cylinders. In the present study we focus on an area of VIV research that has not seen very much attention in the literature, and a specific type of vortex structure that is previously unreported.

2.1.1. Previous Research

A number of studies have shown the presence of complex large scale three-dimensional structures in the wake of a circular cylinder. Van Atta, Gharib and Hammache (1988) observed what they described as staggered "blobs" in smoke wire photographs 50 diameters downstream of a self-excited cylinder. The Reynolds number based on diameter (Re_D) was 68. No comment on vortex structure was given. Cimbala, Nagib and Roshko (1988) observed three-dimensional staggered patterns in the far wake of cylinders at Reynolds numbers of 140 and more than 200 diameters downstream of the cylinder with minimal

---

[1] Submitted to Experiments in Fluids as: Hydrogen Bubble Visualization of the 'Void' Structure in the Wake of a Self-Oscillating Circular Cylinder by Gilbert S, Sigurdson L.
Published in: Gilbert S, Sigurdson L (2005) Hydrogen bubble flow visualization of a self-oscillating cylinder vortex street "void". Gallery of Fluid Motion, Physics of Fluids 18:7.
Also Published in American Physical Society (APS) Abstracts for:
a) APS talk Nov 2004. Hydrogen bubbles as a Visualization tool in Cylinder Shedding by Sigurdson L, Gilbert S.
b) APS talk Nov 2004 Hydrogen bubbles as PIV/ICV tracers in Cylinder Shedding by Gilbert S, Sigurdson L.

vibration. Eisenlohr and Eckelmann (1989) showed the existence of 'vortex splitting' in the wake of both cylinders and flat plates using smoke wire visualization. Williamson (1992) found the existence of 'vortex dislocation' structures in the wake of a circular cylinder with controlled minimal vibration. His visualizations were completed using dye and smoke wire visualization and complemented with hotwire measurements for Re_D ranging between 180 and 260. Newman and Karniadakis (1996, 1997) see a "staggered pattern of vorticity that is connected in a woven lattice pattern" at a Re_D of 100 in their numerical experiments.

2.1.2. Unique Qualities of this Investigation and Overview

We present research into the formation of a large scale vortex structure, that we have called a 'void' due to the absence of bubbles directly downstream of it. The bubbles are present due to the use of hydrogen bubble visualization. This structure is found on a rigidly mounted flexible cylinder for Re_D less than 185. To our knowledge, we are the first to visualize the 'void' structure that we describe in Section 2.4. In this section we also present an idealized vortex skeleton model that describes the vortex dynamics of this structure. This structure has unique qualities that have not been documented in the literature.

In Section 2.5, we develop and use a vibration model to show how the structure closely corresponds to an anti-node in the transverse vibration, and a node in the stream-wise vibration. Such a vibration event has not been previously linked to any large scale structure in the wake of a cylinder and there are a variety of reasons why we believe that the void structure is a new discovery.

Firstly, such vibration events cannot occur in the flexibly mounted rigid cylinder results that dominate the literature as these cylinders only have a rigid body vibration mode of pure translation. Conversely, a rigidly mounted flexible cylinder has an infinite number of natural frequencies which each correspond to a very well known span-wise mode shape of vibration. It is these 'modal responses' that make the occurrence of span-wise nodes and anti-nodes possible. These mode shapes are given in Section 2.5.1, but they can also be found in the VIV text of Blevins (1990) or any textbook on vibration theory (Inman 2001).

Secondly, when we look to the very limited research into flexible cylinder vibrations, we can see that it is not likely that the researchers conducted experiments with the necessary conditions for observing 'void' formation. Van Atta et al (1988) conduct visualization experiments at the 14th and 28th modal responses of the flexible cylinder's transverse vibration. Van Atta and Gharib (1987) give a detailed study of cylinder oscillation and vortex shedding frequencies down to the 5th mode of transverse vibration, but provide no flow visualization. We did experiments up the 7th mode of transverse vibration. However, we found that our 'void' structures were quite difficult to find in any mode other than the 1st mode of transverse vibration. The 'void' structures we did find at higher modes of vibration are not well defined, and were quite unstable.

Although Newman and Karnaidakis (1996, 1997), Brika and Laneville (1993) and Willden and Graham (2001) publish data in the lower vibration modes, they all chose not to allow stream-wise vibrations. Stream-wise vibration nodes are a critical ingredient in the formation of other large scale structures (Van Atta et al, 1988). We will also show that they are also a critical ingredient in the formation of our very different 'void' structure. All other studies found for a rigidly mounted flexible cylinder do not present any details on vortex dynamics or flow visualization, and choose to focus on cylinder motions and lift and drag forces which are of great importance when modeling flexible cylinder vibrations (Huarte et al, 2006; Chang et al, 1997; Kin and Perkins, 2002; Skop and Balasubramanian, 1997).

Thirdly, hydrogen bubble visualization, which has not usually been used in cylinder shedding research, is used in the present study to visualize the cylinder flow up to a Re_D of 185. We show in Section 2.3 that the H_2 bubbles became trapped in the low pressure cores of the Karman vortex street, allowing us the unique opportunity to directly visualize the vortex structure. Such visualizations remain quite well defined until the cores become too diffuse for the dynamic pressure gradient to keep them there. Since the bubbles are formed and released from the vibrating cylinder itself, we provide data in Section 2.3 showing that this process does not influence the vortex shedding and vibration characteristics of the cylinder.

This paper is a more thorough treatment of the image and text presented by Gilbert and Sigurdson (2005) in the Physics of Fluids Gallery of Fluid Motion. In Section 2.3 we validate the use of bubbles in cylinder shedding research. We discuss observations; and we propose a vortex dynamics explanation for the structure in Section 2.4. We derive and solve a flexible cylinder vibration model in Section 2.5, which is used to comment on the perturbation which causes our large scale structure. We also compare our structure with other large scale structures found in the cylinder wake in Section 2.6.

2.2. Experimental Apparatus

In the present experiments, we used a closed loop water tunnel with a test section that is 2.1 meters long. The test section has a rectangular cross section of 0.27 m by 0.47 m. A schematic of the closed loop water tunnel is shown in Figure 2.1. We used a form of Image Correlation Velocimetry (ICV) as described in Apps (2001), and Apps, Chen and Sigurdson, (2003) to estimate the tunnel turbulence intensity and to quantify buoyant bubble rise velocities in the wake of the cylinder. The background turbulence intensity is less than 1%. Such a value is consistent with the cylinder oscillation investigations of Govardhan and Williamson (2000, 2004, 2006), Sarpkaya (1978) and Anagnostopoulos and Bearman (1992).

The stainless steel hydrogen bubble wire also served as the oscillating cylinder. Since we are using water, the mass ratio (m^*) is 8. The mass ratio is defined as the oscillated body mass divided by the displaced fluid mass. The cylinder is 0.02286 cm (0.009in) in diameter (D) giving an aspect ratio (L/D) of approximately 2000, where L is the cylinder length. Norberg (1994) states that such a large aspect ratio ensures shedding at mid-cylinder span that is independent of end conditions in the laminar flow regime. Therefore the use of endplates to remove boundary layer effects was not necessary (Hammache and Gharib 1991; Williamson 1989; Norberg 1994). The general layout of the cylinder apparatus is shown in Figure 2.2. The cylinder is rigidly mounted, with no structural damping or stiffness and is allowed to self-oscillate in both the transverse (y) and stream-wise (z) directions due to the vortex shedding forces.

In order to have control over the natural frequencies of the cylinder, the tension (to within +/- 0.1 N) in the wire was controlled by use of precision weights. As a result, the vacuum natural frequency (f_{vac}) was controlled to +/- 0.56 Hz. Due to the more pronounced effects of added mass in water, the actual body oscillation frequency will only be approximately equal to the vacuum natural frequency (Sarpkaya 2004).

We refer to f_{vs} and f_s as the shedding frequencies of the vibrating and stationary cylinder. The term f_{ex} denotes the actual body oscillation frequency. The values for f_s are taken from the correlation given by Williamson (1989). More details on this topic will be discussed when we compare vibration mode shape theory to our experimental results.

Image Correlation Velocimetry as developed by Apps (2001) and Apps, Chen and Sigurdson (2003) was used to quantify the velocity field behind the cylinder. An in-house fabricated power transformer was used to produce the desired power for electrolysis. The bubbles originate on the cylinder in a sheet and images of this sheet are taken using a Nikon D1x digital camera. For high resolution images, we used the D1x with a bellows with the lens mounted in the reversed position in order to obtain significantly larger magnification.

We decided to back-calculate the shedding frequency from high resolution measurements of the vortex street wavelength. These measurements were taken from calibrated flow visualization images. The shedding frequency can be described in terms of the wavelength and the vortex convection velocity (U_c) as:

$$f_{vs} = \frac{U_c}{\lambda}$$

or

$$f_{vs} = \frac{U_c}{U_\infty}\frac{U_\infty}{\lambda} \qquad [2\text{-}1]$$

Detailed values for U_c/U_∞ are given by Williamson (1989) for a stationary cylinder. When compared with the mechanically oscillated cylinder data from Griffin and Ramberg (1974, 1976) we can see that the stationary cylinder data gives a good estimate. The use of this approximation is necessary as the use of hot film probes to determine shedding frequencies is quite problematic in this water tunnel. Dissolved air tends to come out of solution on the probe making measurements inaccurate. Also, probes do not give instantaneous span-wise measurements of wavelength and frequency.

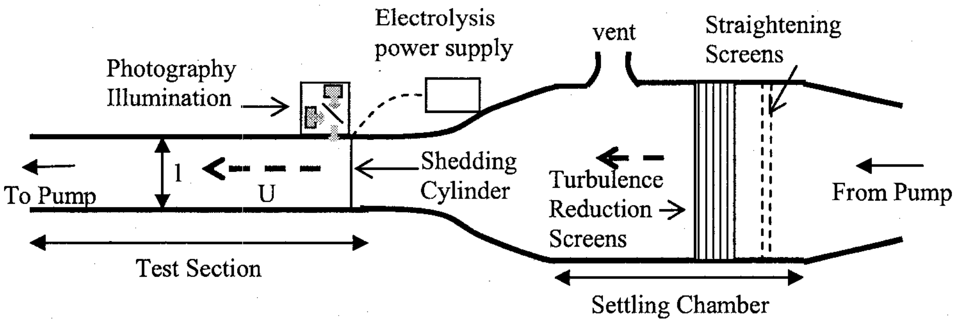

Figure 2.1. Closed loop Water Tunnel Schematic

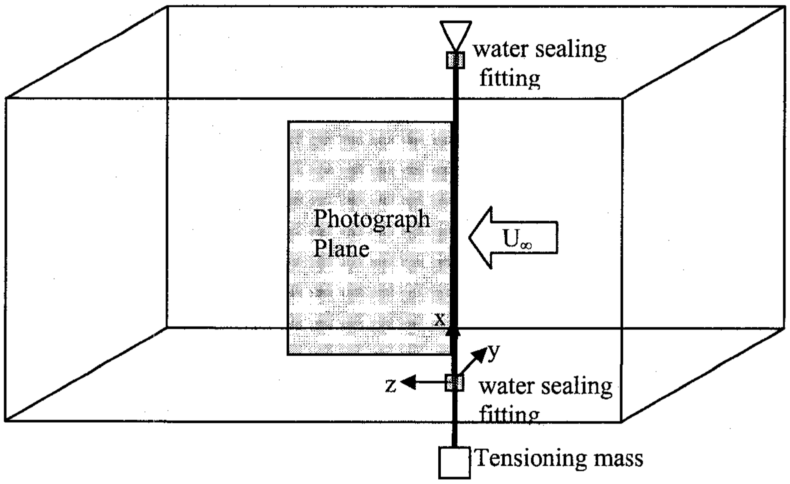

Figure 2.2. Wire Tensioning Apparatus Schematic

2.3. Validation of the Use of Bubbles in VIV Research

A potential issue with this apparatus is the possible disturbances generated by bubbles as they are being shed from the cylinder surface. To access the influence of the bubbles upon the experimental results we conducted 4 experiments. Firstly, we wanted to validate the stationary cylinder case by determining the critical Re_D for shedding. Secondly, we wanted to show that the vortex induced vibration process was not modified by bubbles. Thirdly, we want to show that bubbles do not interfere with the formation of large scale structures along the wake. Finally in the 4th experiment, we set out to quantify the buoyant bubble rise velocities and to get an idea of the diameters of the bubbles tracking the flow field.

In the first experiment, we set out to determine the onset of shedding from a stationary, or minimally vibrating, cylinder. To do this the cylinder was loaded heavily with precision mass so that vibration would be insignificant for Re_D between 30 and 60. The tunnel speed was slowly increased in increments until vortex shedding began. We found shedding to occur at Re_D of 46.5 +/- 1.7, a very typical value for stationary cylinders. Therefore, we can be confident that the hydrogen bubble visualization of the flow around a cylinder undergoing minimal vibration is unaffected by the bubbles being shed from the cylinder.

In the second experiment, we set out to reproduce commonly found results for VIV cylinders. The most widely agreed upon aspect of vortex induced vibration is the concept of synchronization or lock-in where the shedding frequency is locked-in to the natural frequency of the structure. We want to prove that synchronization still occurs with bubbles tracking the cores, and that it occurs within typical lock-in bands observed in the literature. From Figure 2.3a and b we can readily see that lock-in of the first mode of the flexible cylinder does occur very close to f_{vs}/f_n of 1. This lock-in, also commonly referred to as synchronization of the vortex shedding frequency (f_{vs}) with the cylinder in water natural frequency (f_n) is well documented in VIV and even mechanically induced oscillations of circular cylinders. Ability of a cylinder to remain locked-in is commonly quantified in terms of the ratio between stationary cylinder shedding frequency and cylinder natural frequency (f_s/f_n). Our lock-in band is between f_s/f_n of 0.92 and 1.32. This compares well with a lock-in band from Willden and Graham (2006) which is between f_s/f_n of 0.82 and 1.25 with peak transverse amplitude (A_y/D) of 0.35. Data compiled by Blevins (1990) related our lock-in band with a peak amplitude between $A_y/D=0.3$ and 0.4. This is below the absolute maximum Ay/D value of 0.6 for laminar VIV as given from the compiled sources in Williamson and Govardhan (2004). Since we calculate plotted shedding frequencies using the measured vortex wavelengths we can be certain that the bubbles are tracking the vortex cores. This is a unique advantage of hydrogen bubbles as the flow tracer, as we get a direct visualization of the vortex structure.

Since we are confident that bubbles are not modifying the vibration processes at lock-in, we can look at cases outside of lock-in. From Figure 2.3a and b we can see that the wavelength of the Karman street, and hence frequency, both return to the stationary cylinder case. This result is also common in the existing literature of low Reynolds number vortex induced cylinder vibration (Willden and Graham, 2006; Singh and Mittal, 2005). Since f_{vs} is calculated using [2-1], which has an approximation for U_c, and f_{vs} only deviates slightly from f_s in Figure 2.3b for non-locked in conditions we can be certain that the U_c correlation is performing well over a wide variety of Re_D. Therefore, we are confident that bubbles are tracking the cores and that they do not have any appreciable affect on typical vortex induced vibration events.

In our third experiment we want to show that the bubbles are not affecting the formation of large scale structures in the cylinder wake. To do this we reproduced the results of Van Atta et al (1988) . Van Atta et al used smokewire techniques to find their vortex “blob“ structures. We found these identical structures using hydrogen bubble visualization. Therefore, we can conclude that the bubbles are not effecting large scale vortex structure events.

Van Atta et al also stated that the vortex “blobs“ occur at nodes in both the stream-wise and transverse vibration. Due to this, we were able to validate the use of our vibration model as we were able to independently verify their results. In addition, we have indirectly shown that our turbulence intensity value could be as low as 0.05% since this was the value in the wind tunnels used by Van Atta et al.

The fourth experiment was designed to evaluate buoyant bubble rise velocities and diameters of the bubbles. We showed previously that the bubbles track the cores. This is a significant advantage over scalar tracers as they do not respond to the dynamic pressure gradients of the vortex structure. Unfortunately the value of scalar tracers is that they are not subject to the buoyant forces of bubbles. We calculate the bubble rise velocities using ICV with very small correlation windows so it is essentially a cross correlation particle tracking technique. In the calculations, rise velocities were taken from 5 different images at a given free-stream velocity. The velocity field data is then averaged over the span, and 2 stream-wise regions. The near wake region corresponds to $z/D < 20$, and the wake region corresponds to $20 < z/D < 120$. The Re_d range of the images is between 0 and 150.

In Figure 2.4a we plot the relative rise velocity (V_b/U_∞) versus the tunnel velocity U_∞. For region C the bubbles are fully trapped in the vortex cores and the tunnel velocity (U_∞) is between 25 and 65 cm/s. In this region, the relative rise velocities are below 5% showing that rise velocities are relatively insignificant. Region B, with V_b/U_∞ of 20%, is a region where bubbles are only partially trapped in the vortex cores. This region starts at the onset of shedding at Re_d of around 47 and ends at about 56. This corresponds to tunnel velocities of approximately 18 to 24 cm/s. In region A, where no shedding is occurring, we find that the bubble rise velocities increase drastically with decreasing tunnel velocity. Hence, bubble trapping effectively makes bubble rise velocities independent of the mean flow velocity.

Bubble diameters are obtained through theoretical calculation and by direct measurement from the calibrated images. Using the creeping flow assumption Jiang (1992) and Jiang et al (1993) equated the buoyant force to the total drag on a rising bubble. This gives a terminal velocity U_{bt} relation for which to calculate bubble diameters.

$$U_{bt}=\frac{g\Delta\rho D_b^2}{12\mu} \qquad [2\text{-}2]$$

Where g is the gravitational constant, $\Delta\rho$ is the density difference between liquid and gas, D_b is the bubble diameter and μ is the viscosity of the liquid. The rise velocity value obtained by ICV is taken as the terminal velocity, $U_{bt}=V_b$. Figure 2.4b shows bubble diameters estimated using [2-2] and the ICV bubble rise velocities. Bubble diameters as measured directly from high resolution images are also given in the figure. We can see that both calculated and measured bubble diameters are found to be about half of the wire diameter within the full bubble trapping of region C. The bubble diameters are much higher within the no shedding region A.

From these experiments, we can conclude that after the bubbles become fully trapped in the cores they behave in a quite similar way to scalar tracers. The added advantage is that the dynamic pressure gradient overcomes the hydrostatic pressure gradient and bubbles directly track the low pressure cores. Not only do we validate the use of bubbles in cylinder shedding research, we recommend their use for cases where detailed visualization of the vortex structure is required.

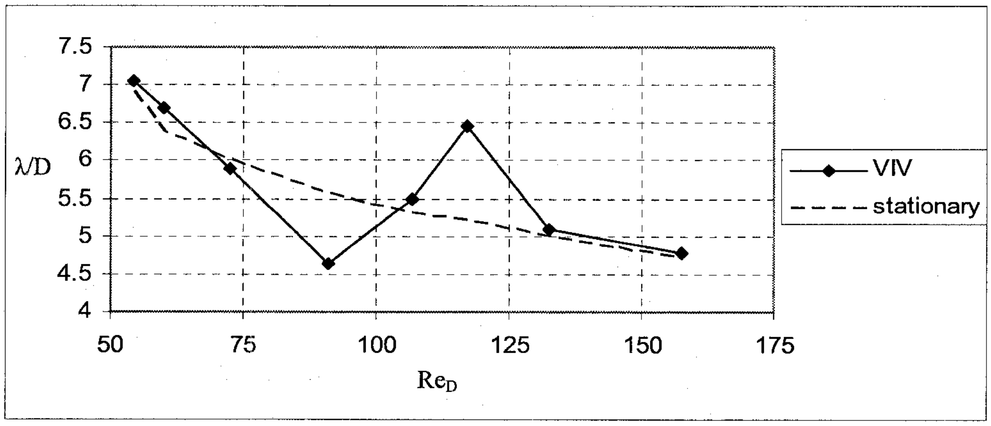

a) Karman Street wavelength normalized by diameter. Stationary data from Williamson (1989)

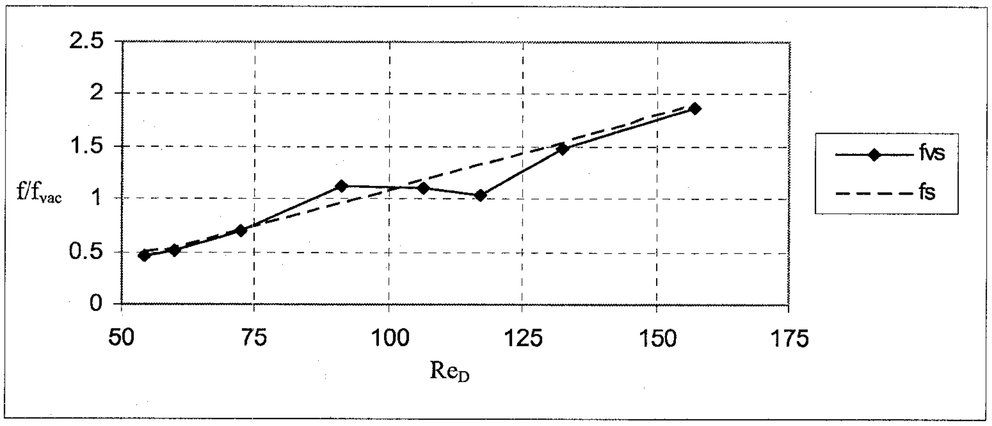

b) Vibrating cylinder frequency and ideal non-oscillating cylinder frequency normalized by f_{vac}.
Stationary data from Williamson (1989)

Figure 2.3. Verification of VIV data

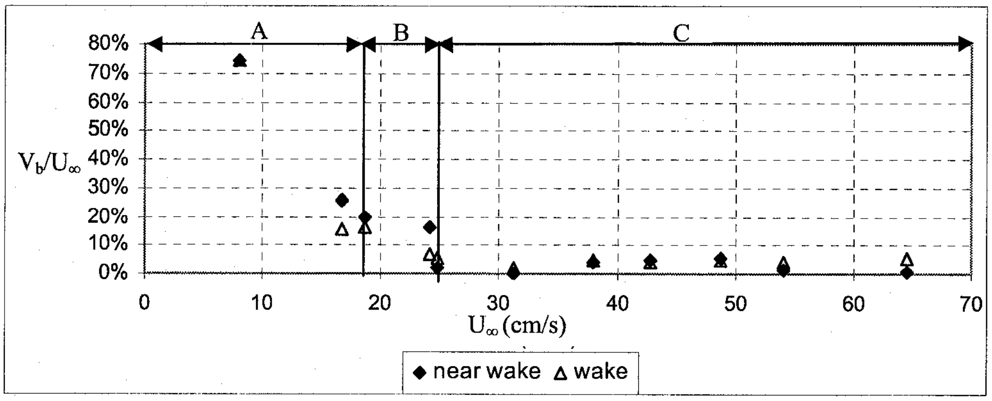

a) Relative Rise velocity of bubbles in the near and far wake

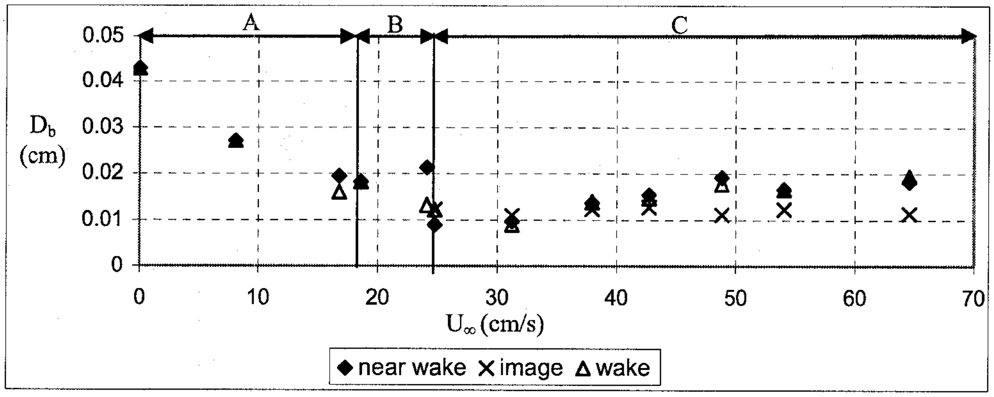

b) Calculated Bubble diameters from rise velocity using creeping flow assumption

Figure 2.4. Rise Velocity and Bubble Diameters (D=0.0228cm)

A- Region of No shedding
B- Shedding with Partial bubble trapping
C- Shedding with Full bubble trapping

2.4. 'Void' Structure

The full view of the large-scale vortex structure is shown in Figure 2.5. The z/D values are given in the Figure, where z is the downstream distance from the cylinder. A characteristic feature of a 'void' is the vortex pinch-off of adjacent Karman vortices of opposite-signed vorticity. This pinch-off is seen in the very high resolution image of Figure 2.6 and to some extent in the lower resolution photograph Figure 2.5. To show the vortex structure in greater detail, we haved overlayed line vortices on the high resolution photograph as shown in Figure 2.7. We suggest that the 'void' structure has two distinct regions. Firstly, very close to a wire (z/D less than 10) we have the vortex quadrupole structure. This structure then transforms into a vortex pinch-off structure where the primary pinch-off occurs at approximately z/D of 20. These primary pinch-offs convect downstream to z/D of approximately 75 where there may be a subsequent pinch-off, as seen in the bottom right corner of Figure 2.6. These pinch-offs propagate away from the primary pinch-off in the span-wise direction. This secondary vortex pinch-off may be due to the Crow instability (Crow 1970) acting on the opposite-signed pair of Karman vortices that were joined in the primary pinch-off. This instability appears to propagate via waves along the vortex cores. This creates a disturbed area that forms the turbulent wedge shape reminiscent of the bow waves formed by a ship at sea. A pinch-off of Karman vortices across the wake was originally suggested by Roshko (1976). To our knowledge, our visualizations are the first images of this actually occurring. Roshko proposed that a pinch-off of this type could explain earlier time-averaged results of other researchers.

It is this pinch-off which differentiates this structure from the 'stable (in-phase) symmetric two sided vortex dislocation structure' of Williamson (1992). His dislocation structures involved vortex interaction of like signed vorticity. The pinch-off seen here involves interaction between a vortex with positive vorticity and a vortex shed from the other side of the cylinder, which has negative vorticity.

2.4.1. Idealized Vortex Skeleton Models

Vortex skeleton models are shown in Figure 2.8a and b. These models are meant to indicate approximate geometries, but do not strictly indicate the actual line vortex shape. The dashed and solid vortices are shed from the bottom and top of the cylinder respectively.

It is apparent from Figure 2.5 that a 'void' is caused by a perturbation that occurs within a diameter or less of the cylinder. The perturbation has a portion of the core lagging behind, or upstream of, the span-wise adjacent portions. This is idealized in Figure 2.8a. The perturbation grows with advection downstream, and results in the production of what is effectively a counter-rotating stream-wise vortex pair. With the same perturbation growing on the opposite-signed vortex cores across the street, this essentially forms a vortex quadrupole. Although the vorticies in the quadrupole are shown as continuous line vortices, they are not thought to directly link up in this way. However, this quadrupole structure helps us to understand the dynamics of stream-wise vorticity.

Even before the pinch-off occurs, the quadrupole vortex cores would move closer to each other across the wake and in the span-wise direction convect away from each other. In the plane orthogonal to the stream-wise direction, the potential flow point vortex equivalent would be a counter-rotating vortex pair approaching a wall, where the vortices move away from each other as they approach the wall due to the influence of the image vortices. Even without any pinch-off occurring, this type of vortex structure would sweep the tracer bubbles out of this region creating an absence of bubbles, resulting in a 'void' appearance. It also produces a straining field which is a necessary condition for a pinch-off to occur (Schatzle 1987). The two-dimensional Karman vortex street also contains a straining field.

As the vortices move downstream they are advected toward each other until they "pinch-off", break and re-join with an opposite-signed vortex from the other side of the street as is idealized in

Figure 2.8b. This pinch-off further accounts for the removal of many of the tracer bubbles downstream of the cylinder as bubbles are swept away with the cores as they convect laterally. The vortex line shape begins to curl up as this is the self-induced motion of a hairpin "loop" line vortex. This curl up is not shown in Figure 2.8b.

All 'voids' are accompanied with a diffuse cloud of bubbles that originates at the pinch-off location and surrounds the region with no tracers. This further supports the pinch-off hypothesis, since some bubbles would be expected to escape the cores during this process. The modified dynamic pressure gradient within the pinch-off region allows bubbles to escape which are not reclaimed by the vortex cores.

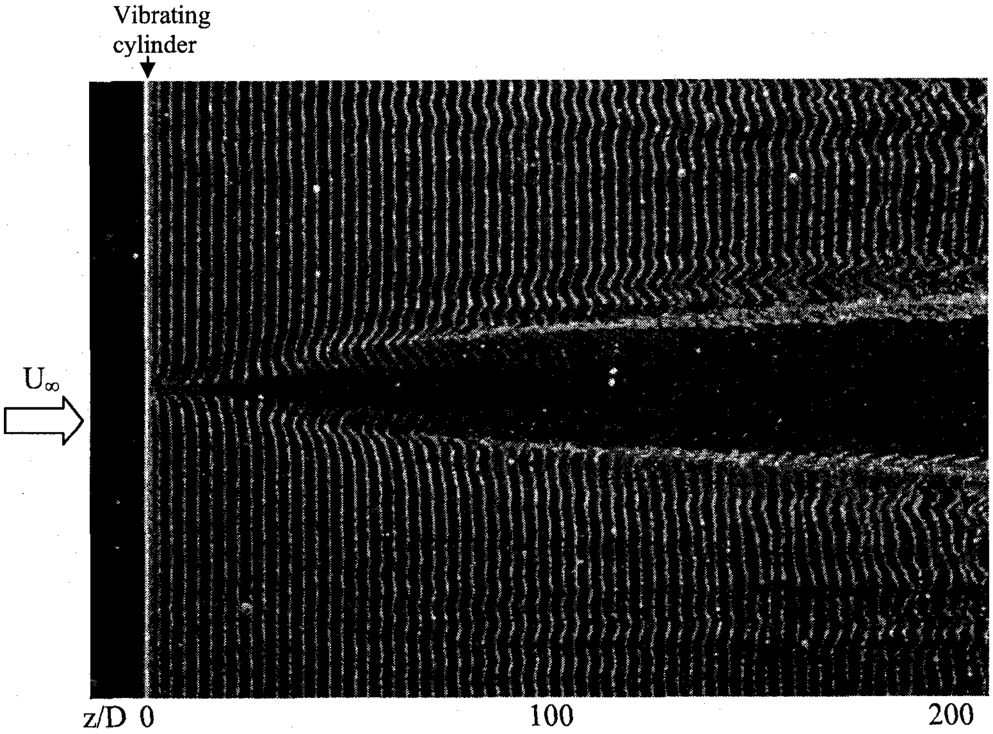

Figure 2.5. 'Void' Structure visualized behind a self oscillating circular cylinder at Re_D=70 and f_{vs}/f_n=0.8

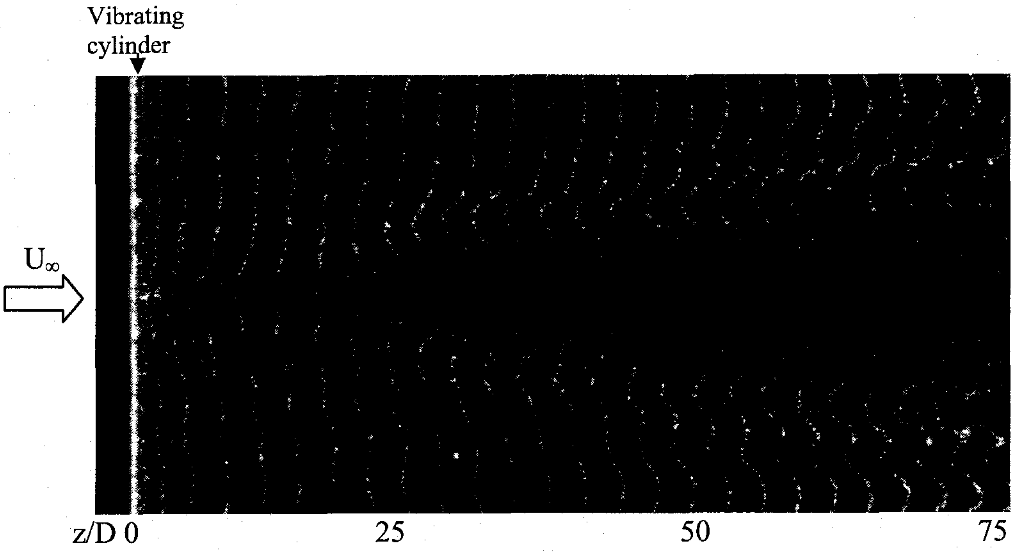

Figure 2.6. 'Void' Close up showing pinch-off structure at Re_D=84 and f_{vs}/f_n=0.85

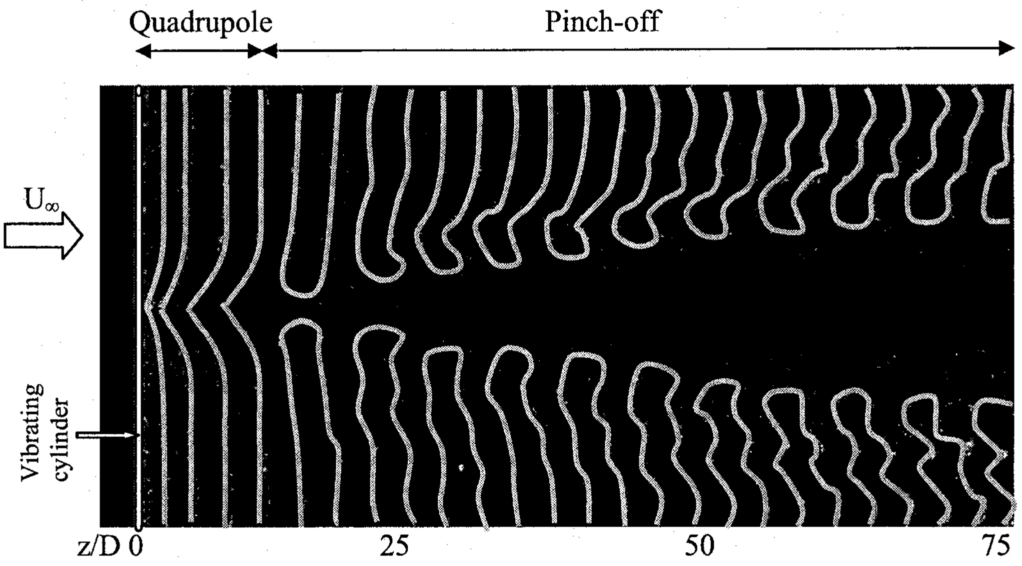

Figure 2.7. Vortex Skeleton Overlay for high resolution photograph at Re_D=84 and f_{vs}/f_n=0.85
Showing vortex quadrupole structure for z/D less than 10 and vortex pinch-off for z/D greater than 10.

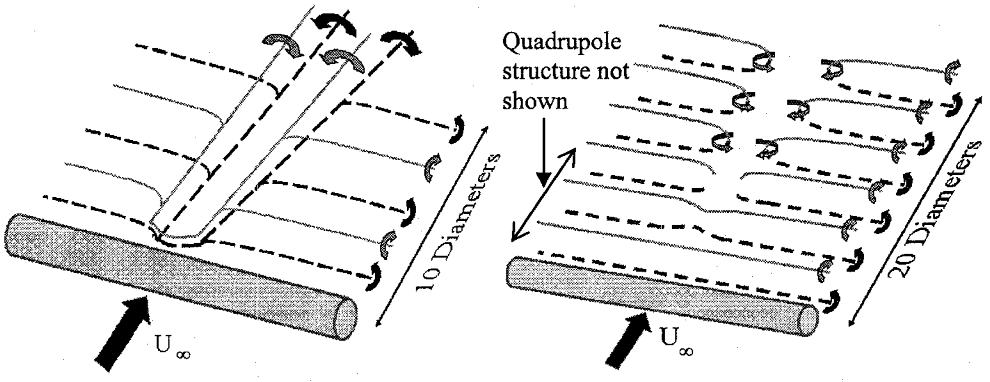

a) Vortex Quadrupole Model b) Vortex Pinch-off Model

Figure 2.8. Idealized Vortex Skeleton Models
Solid line indicates upper vortex cores which are shed from the top of the cylinder, dashed line lower vortex cores from the cylinders bottom.

2.5. Perturbations and Void Formation

Questions arise as to what conditions are necessary for the occurrence of voids. Clearly the Re_D is a factor, as shedding needs to be present and the dynamic oscillation forces must be great enough to trigger the instability producing the phenomenon. Another consideration is what determines the precise location of the voids along the span of the cylinder.

At first it was suspected that the structure was caused by a surface imperfection in the cylinder. If surface imperfections were causing the structure, the structure would always occur at the same location. This most definitely did not occur. Van Atta et al (1988) found large scale vortex 'blob' structures to exist at nodes in the wire vibrations. Hence a theory that 'void' structures occur in close proximity to a span-wise vibration event is reasonable.

In our very first experiments void structures were found to exist in a random manner on a wire with uncontrolled tension or even compression. Reynolds numbers for this experiment ranged between 110 and 185. Unfortunately no methods were available to quantify anti-node and node locations on the wire vibration in these early experiments. In the more recent experiments, which are the focus of this paper, tension is controlled and we can get a good estimate of node and anti-node locations through vibration theory. The theory was validated by reproducing the results of Van Atta et al (1988) and we will show that it is a very useful tool for predicting where a void will occur along the span of the wire. A condensed derivation of the theory will be presented next.

2.5.1. Vibration Theory for a Flexible cylinder

Our objective in this section is to calculate the locations of nodes and anti-nodes in the span-wise distribution of vibration. We will find that the actual amplitudes of the exciting forces do not influence these locations. Positions of nodes and anti-nodes are influenced most heavily by the shedding frequency (f_{vs}) and the closest cylinder natural frequencies (f_n) to the shedding frequency. The mode shapes ($X_n(x)$) associated with those natural frequencies will then determine where nodes and anti-nodes are located. These mode shapes are not unique to this discussion and can be derived through the solution to the wave equation model. They are also published in Blevins (1990) and Inman (2001).

The distributed vibration problem of a flexible cylinder is governed by the wave equation. The full derivation using Newton's second law is done in Appendix A.1. It is similar to the derivation in Inman (2001) but it is modified to allow for both transverse vibrations and stream-wise vibrations.

The wave equations governing this problem are:

$$\frac{\partial^2 w_y(x,t)}{\partial t^2} + \frac{\gamma_y}{\rho A}\frac{\partial w_y(x,t)}{\partial t} - c^2\frac{\partial^2 w_y(x,t)}{\partial x^2} = F_y(x,t,A_y,A_z,\mathrm{Re}_d) \qquad [2\text{-}3]$$

$$\frac{\partial^2 w_z(x,t)}{\partial t^2} + \frac{\gamma_z}{\rho A}\frac{\partial w_y(x,t)}{\partial t} - c^2\frac{\partial^2 w_z(x,t)}{\partial x^2} = F_z(x,t,A_y,A_z,\mathrm{Re}_d) \qquad [2\text{-}4]$$

The y and z subscripts denote transverse and stream-wise vibrations. The transverse and stream-wise vibration distributions are given by $w_y(x,t)$ and $w_z(x,t)$. The structural damping is denoted γ. On the left hand side of the equations we have the structural terms, and on the right we have the more complex fluid dynamic terms.

At first, the structural terms derived from Newton's second law have a definite coupling between the transverse and stream-wise vibration models. The structural parts of the model, associated with the internal tension, decouple by virtue of a small angle assumption. Such an assumption is valid since the amplitudes of vibration are not visible to the human eye. The wave speed (c) depends on the applied tension (T), the cylinder density (ρ_c) and cross sectional area (A). It also includes the added mass term ($\Delta\rho_f$) which is highly debated in the current literature. The wave speed is calculated using:

$$c = \sqrt{\frac{T}{(\rho_c + \Delta\rho_f)A}} \qquad [2.5]$$

For the purposes of our study we will use the added mass coefficient definition:

$$\Delta\rho_f A = C_a \rho_{water} A_{cylinder}$$

Therefore the effective density for calculating the wave speed is:

$$\rho_{effective} = \rho_c + C_a \rho_{water}$$

When using air as the working fluid, the added mass term is generally negligible. However, since the density of the steel is approximately 8000kg/m^3 and the water density is nominally 1000kg/m^3 the added mass term is important. Sarpkaya (1978, 2004) shows how the added mass could be between -0.5 and 1.5 depending on the experimental conditions encountered in our experiments. Similar results are reproduced by Zhou et al (2000) and Willden and Graham (2001). If we use an added mass coefficient of 1, as is commonly used, our effective density could have errors of 20%. Therefore using Sarpkaya's data to correct the effective density would be better than assuming C_A=1. Regardless, the point of this model is to calculate anti-node and node locations. When comparing node locations for stream-wise vibration as calculated separately using both values for added mass, the maximum shift of nodal locations is only 2% of the cylinder span

To calculate the natural frequencies of the flexible cylinder we require the span-wise length of the cylinder (L) and the wave speed. The infinite number of modal natural frequencies is calculated as:

$$\omega_n = \frac{cn\pi}{L}, \text{ n=1, 2, 3, 4 \dots} \qquad [2\text{-}6]$$

This term is used directly in the calculations to determine how much a vibration mode manifests itself in the span-wise distribution.

The fluid dynamics terms, found on the right hand side of [2-3] and [2-4], have the fluid dynamic forces that are created by the vortex shedding. The transverse and stream-wise components of these terms are most definitely coupled. In the interests of the continuity of this discussion, we will give the final fluid dynamic forcing model and provide the full derivation details in Appendix A.2. The final equations of forcing are:

$$F_y(x,t) = X(x)\left(-F_{dl,y}\cos(\omega_{vs}t) + F_{ml,y}\sin(\omega_{vs}t)\right) \qquad [2\text{-}7]$$

$$F_z(x,t) = X(x)\left(-F_{dl,y}\cos(2\omega_{vs}t) + F_{ml,y}\sin(2\omega_{vs}t)\right) \qquad [2\text{-}8]$$

The eigenfunctions of the homogeneous wave equation problem, also called the mode shape $X(x)$, are used to correct for span-wise variation in the forcing which are unique to the flexible cylinder as shown by Newman and Karnaidakis (1996, 1997), Huarte et al (2006), and Willden and Graham (2001). The angular frequency of vortex shedding ω_{vs}, has the characteristics as seen in Figure 2.3b of Section 2.3. The stream-wise vibration frequency is given by the well known frequency doubling effect (Jauvtis and Williamson 2004; Sarpkaya 2004). The force decomposition terms include the sine and cosine terms, along with their respective force transfer coefficients F_{dl} and F_{ml}, as developed by Sarpkaya (1978). Sarpkaya used experimental results to determine the force transfer coefficients at a wide variety of cylinder oscillation conditions.

We obtain the wave equation model for our cylinders vibration when we substitute [2-7] into [2-3] and [2-8] into [2-4]. These substitutions yield.

$$\frac{\partial^2 w_y(x,t)}{\partial t^2} + \frac{\gamma_y}{\rho A}\frac{\partial w_y(x,t)}{\partial t} - c^2\frac{\partial^2 w_y(x,t)}{\partial x^2} = X(x)\frac{\left(-F_{dl,y}\cos(\omega_{vs}t) + F_{ml,y}\sin(\omega_{vs}t)\right)}{\rho A}$$

[2-9]

$$\frac{\partial^2 w_z(x,t)}{\partial t^2} + \frac{\gamma_z}{\rho A}\frac{\partial w_z(x,t)}{\partial t} - c^2\frac{\partial^2 w_z(x,t)}{\partial x^2} = X(x)\frac{\left(-F_{dl,y}\cos(2\omega_{vs}t) + F_{ml,y}\sin(2\omega_{vs}t)\right)}{\rho A}$$

[2-10]

A very similar solution procedure as is required for [2-9] and [2-10] is given in many engineering vibrations textbooks the reader is referred to Inman (2001) for more details. The solution to the transverse vibration problem is:

$$w_y(x,t) = \sum_{n=1}^{\infty} w_{n,y}(x,t) = \sum_{n=1}^{\infty}\left[\sin\left(\frac{n\pi x}{L}\right)\left(X_{dl,n,y}\cos\left(\omega_{vs}t - \theta_{n,y}\right) + X_{ml,n,y}\sin\left(\omega_{vs}t - \theta_{n,y}\right)\right)\right]$$

$$X_{dl,y} = \frac{f_{dl,y}}{\sqrt{\left(\omega_n^2 - {\omega_{vs}}^2\right)^2 + \left(2\zeta_{n,y}\omega_n\omega_{vs}\right)^2}} \quad \theta_{n,y} = \tan^{-1}\left(\frac{2\zeta_{n,y}\omega_n\omega_{vs}}{\omega_n^2 - \omega_{vs}^2}\right)$$

$$X_{ml,y} = \frac{f_{ml,y}}{\sqrt{\left(\omega_n^2 - {\omega_{vs}}^2\right)^2 + \left(2\zeta_{n,y}\omega_n\omega_{vs}\right)^2}} \qquad [2\text{-}11]$$

Where $\zeta_{n,y} = \frac{\gamma_y L}{2cn\pi\rho A}, \omega_n = \frac{cn\pi}{L}, f_{dl,y} = \frac{-F_{dl,y}}{\rho A}, f_{ml,y} = \frac{F_{ml,y}}{\rho A}$.

Similarly for the z vibration, the solution to [2-10] is:

$$w_z(x,t) = \sum_{n=1}^{\infty} w_{n,z}(x,t) = \sum_{n=1}^{\infty}\left[\sin\left(\frac{n\pi x}{L}\right)\left(X_{dl,n,z}\cos\left(2\omega_{vs}t - \theta_{n,z}\right) + X_{ml,n,z}\sin\left(2\omega_{vs}t - \theta_{n,z}\right)\right)\right]$$

$$X_{dl,z} = \frac{f_{dl,z}}{\sqrt{\left(\omega_n^2 - \left(2\omega_{vs}\right)^2\right)^2 + \left(2\zeta_{n,z}\omega_n\left(2\omega_{vs}\right)\right)^2}} \quad \theta_{n,z} = \tan^{-1}\left(\frac{2\zeta_{n,z}\omega_n\left(2\omega_{vs}\right)}{\omega_n^2 - \left(2\omega_{vs}\right)^2}\right)$$

$$X_{ml,z} = \frac{f_{ml,z}}{\sqrt{\left(\omega_n^2 - \left(2\omega_{vs}\right)^2\right)^2 + \left(2\zeta_{n,z}\omega_n\left(2\omega_{vs}\right)\right)^2}}. \qquad [2\text{-}12]$$

Where $\zeta_{n,z} = \frac{\gamma_z L}{2cn\pi\rho A}, \omega_n = \frac{cn\pi}{L}, f_{dl,z} = \frac{-F_{dl,z}}{\rho A}, f_{ml,z} = \frac{F_{ml,z}}{\rho A}$

In Appendix A2 we derive the well known mode shape function:

$$X_n(x) = \sin\left(\frac{n\pi x}{L}\right) \qquad [2\text{-}13]$$

The n^th mode shape has a contribution to the total response when the excitation frequency (ω_{vs}) is in the proximity of the n^th natural frequency (ω_n). Under locked in conditions of f_{vs} with the n^th mode natural frequency (f_n) we will see that the transverse mode shape follows $X_n(x)$ closely. Due to the well known frequency doubling effect, the stream-wise mode shape closely follows $X_2(x)$. For non locked in vibrations we must use [2-11] and [2-12] to determine the steady state vibration response. From the vibration amplitude terms X_{ml} and X_{dl}, it is also seen that the force transfer coefficients F_{dl} and F_{ml} only affect the amplitudes of a mode's vibration slightly, as X_{ml} and X_{dl} are more strongly dependent upon $\left(\omega_{vs}^2 - \omega_n^2\right)$ and $\left(\left(2\omega_{vs}\right)^2 - \omega_n^2\right)$.

2.5.2. Span-wise Vibration Events and Void Formation

We will now apply the vibration theory that was developed in the previous section to the void structures. For the calculations, there is no applied structural damping ($\gamma=0$) and the inertial force transfer coefficient (F_{ml}) will dominate the responses for the typical f_{vs}/f_n values of void formation (Zhou et al, 2000; Sarpkaya, 1978; 2004).

Figure 2.9 shows the results of the theory as it is applied to void structures as they occur in non-locked in conditions and Figure 2.10 as they occur in locked in conditions. In Figure 2.9a and b we show maximum span-wise vibration distributions as calculated for the void structure seen in the photograph Figure 2.5. Due to the approximate values of the force transfer coefficients used in the calculations, we will not give vibration amplitudes in these figures. We have marked the void location, as determined from calibrated photographs with the vertical lines in Figure 2.9 and Figure 2.10. We can see that both cases of locked-in and non locked-in void formation can be closely correlated to a node in the span-wise distribution of stream-wise vibration, and an anti-node of transverse vibration. It is also apparent that this model based correlation is more accurate for locked in cases.

Looking more closely at Figure 2.10, in relation to the locked-in void structures, we can see that the span-wise distribution of transverse vibration is clearly:

$$X_y = X_1 = \sin\left(\frac{\pi x}{L}\right) \qquad [2\text{-}14]$$

We can also see that the span-wise distribution of stream-wise vibration is:

$$X_z = X_2 = \sin\left(\frac{2\pi x}{L}\right) \qquad [2\text{-}15]$$

Therefore, an anti-node of X_y occurs at x/L of 0.5, and the node of X_z occurs also at x/L of 0.5 and all locked-in 'void' structures appear very close to this value. Hence we only require mode shape equation of [2-13] to determine location of the 'void' structure formed under locked-in vibration. However, for the non-locked cases of void formation there are contributions from both X_1 and X_2 for the stream-wise and transverse vibration distributions.

To quantify the performance of our correlation, Figure 2.11a and b both plot the probability that a void will be formed at a theoretically predicted node in stream-wise vibration. Tolerance ranges, as shown visually in Figure 2.11c and given as a percentage of cylinder length, were set up to describe how close voids were formed to the theoretically predicted nodes. From Figure 2.11a, we show that the all void structures corresponding with locked-in cylinder vibrations occur within a tolerance region of 8% or +/- 1.83cm from the predicted stream-wise node. When we extend this calculation to voids formed under non-locked in vibration conditions, we determine that 83.3% of the voids are formed within a tolerance region of 10% or +/- 2.296cm.

Only one 'void' tends to occur on a cylinder undergoing locked in vibrations as seen in Figure 2.12a. Conversely, Figure 2.12b shows many 'voids' coexisting simultaneously on the span under unlocked vibration conditions. This interaction reduces the performance of our model and we can only speculate that there is some intricate vortex dynamics between the various structures that is allowed to occur at lower vibration amplitudes. Or there is un-modeled interaction between the 1st, 2nd and even 3rd modal responses of the flexible cylinder. A similar argument was given by Van Atta et al (1988) for their vortex 'blob' structures.

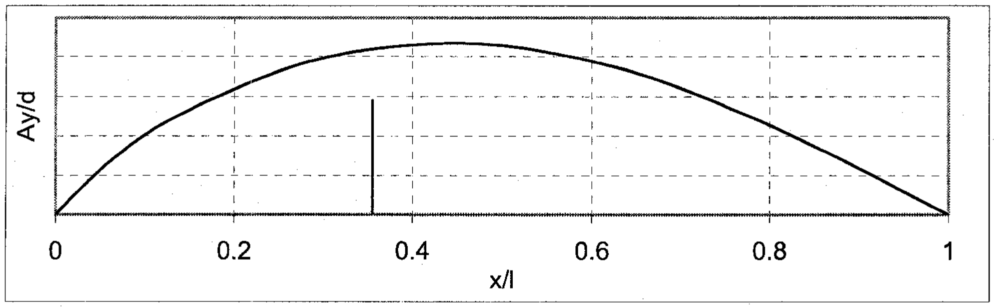

a) Transverse Vibration Distribution; $Re_d=70$ $f_{vs}/f_n=0.79$

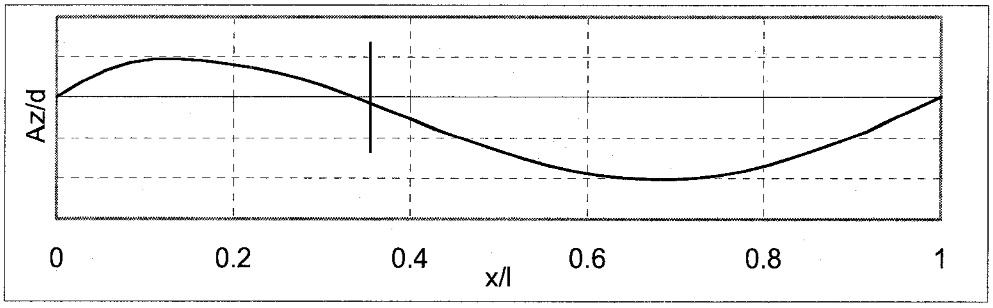

b) Stream-wise Vibration Distribution; $Re_d=70$ $f_{vs}/f_n=0.79$

Figure 2.9. Vibration Theory Applied to Void Structures outside lock-in

A_y/D is the transverse amplitude in the cross-stream direction and A_z/D is the normalized amplitude in the stream-wise direction. Void locations as determined from calibrated photographs are marked by vertical line segments

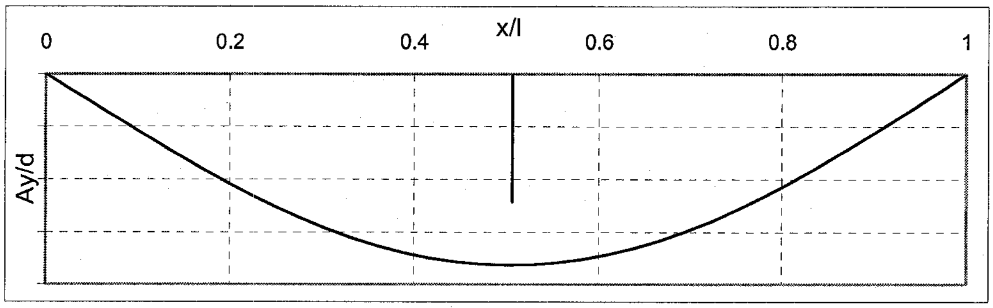

a) Transverse Vibration Distribution; $Re_D=60$ $f_{vs}/f_n=1.01$

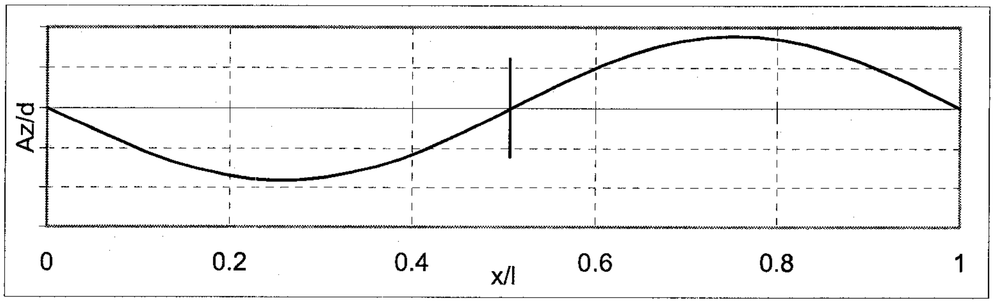

b) Transverse Vibration Distribution; $Re_D=60$ $f_{vs}/f_n=1.01$

Figure 2.10. Vibration theory Applied to Void Structures inside lock-in

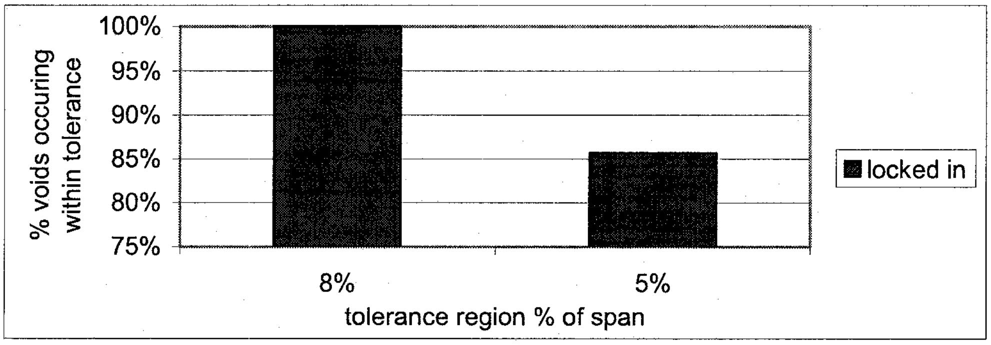

a) Probability of a void being found within a specified tolerance region surrounding a stream-wise vibration node along the span

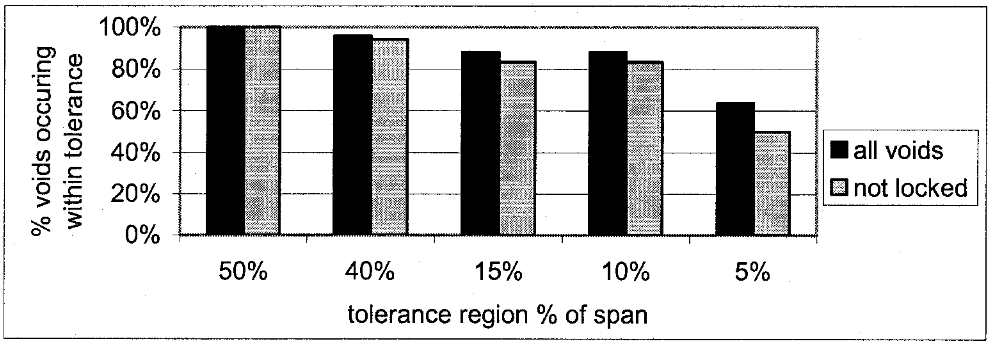

b) Probability of a void being formed within a specified tolerance region surrounding a stream-wise vibration node along the span

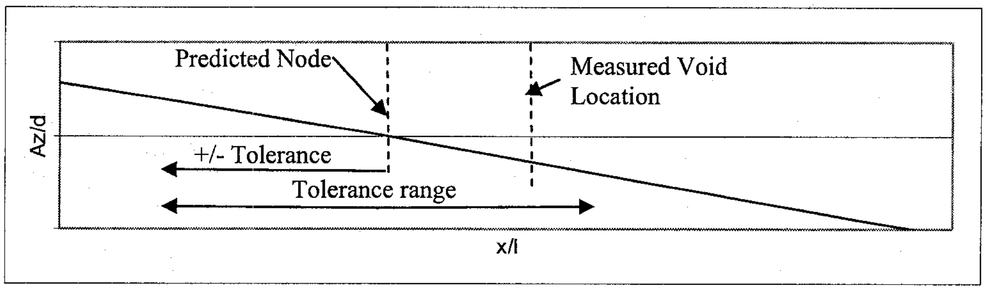

c) Tolerance range and +/- tolerance

Figure 2.11. Probability of Void occurrence within specified tolerances

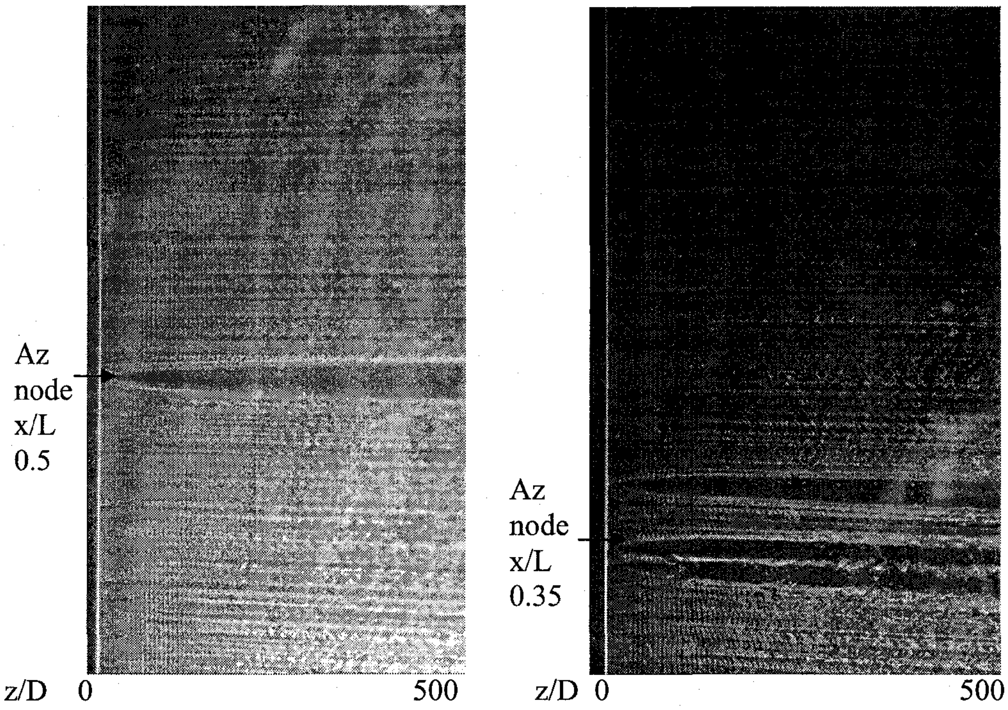

a) Locked in Re_D=72 f_{vs}/f_n=1 b) non-locked in Re_D=71 f_{vs}/f_n=0.8

Figure 2.12. Voids formed under locked-in and non-locked in vibration conditions

2.5.3. Combinations of Shedding and Natural Frequencies of Void Formation

As we just discussed, voids can occur under both locked-in and non-locked in conditions. For the void structures occurring within lock-in, we find that the structures can occur at the smallest values of f_s/f_n for the lock-in region, or initial branch using the terminology of Williamson and Govardhan (2004). This corresponds to a ratio of f_s/f_n of 0.87 to 0.88. All other void structures we found in the later regions of lock-in, or lower branch (Williamson and Govardhan, 2004), corresponding to f_s/f_n of between 1 and 1.09.

Low Re_d VIV studies, at a similar mass ratio, were completed by Singh and Mittal (2005), for both stream-wise and transverse cylinder vibrations, and Willden and Graham (2006), for transverse cylinder vibrations. They showed the existence of modulation of the cylinder response with both f_{vs} and f_n in the initial branch of lock-in. For the upper end, or lower branch of lock-in, they show that these modulations are not significant. This result has also been shown for high Re_D cylinder vibrations (Govardhan and Williamson, 2000). For our flexible cylinder with various mode shapes, such modulations would mean we would have significant modal content at two frequencies. In light of the vibration model, this would cause a complex steady state motion of the nodes and anti-nodes. We argue that this motion of nodal points would restrict the formation of void structures in the initial branch of lock-in. Conversely, it would not effect the formation of the structures in the upper end, or lower branch of lock-in. This can account for the larger ranges of f_s/f_n for void formation in the upper branch.

For non-locked in void structures, all of the void structures were formed near the peripheries of a lock-in region. Values for f_{vs}/f_n correspond to between 0.71 and 0.86 for pre-lock-in cylinder vibration and between f_{vs}/f_n of between 1.12 and 1.31 for de-synchronized vibration. Therefore, we can be certain that some level of vibration was required for the formation of these structures.

The 1st mode lock-in band was where we found the most stable and well defined void structures. We did find, with considerable difficulty, some cases where voids did occur at or near the 2nd and 3rd modal response regions but they were highly intermittent in nature. Once again, frequency modulations could be to blame. Such frequency modulations are caused at the higher modes due to the effects of mode competition between various natural frequencies of the flexible cylinder (Van Atta and Gharib, 1987).

2.5.4. Anticipated Amplitudes of Vibration

To finalize our description of the cylinder vibration, we must also comment on amplitudes of anti-node vibrations. Attempts to resolve such small vibration amplitudes encountered in this study were not successful. Without direct measurement of A_y/D, A_z/D or accurate Fourier averages of experimental cylinder forces f_{ml}, and f_{dl} we are forced to give probable vibration amplitudes based on published data.

In Section 3.3.2, we validated the use of bubbles in VIV research. In this section we used the width of our lock-in band to estimate our maximum transverse vibration amplitude (A_y) of 0.3 to 0.4D from the data in Blevins (1990). Willden and Graham (2006) support this estimate as they obtained maximum A_y/D of 0.35 for a very similar mass ratio and lock-in band. Singh and Mittal (2005) showed that A_y/D amplitudes can be as large as 0.48 in the lock-in band. Such amplitudes should be typical of lock-in vibration at transverse anti-nodes. An upper bound for these vibrations is given by the data compiled from Williamson and Govardhan (2004) which shows that laminar VIV amplitudes can not be in excess of A_y/D of 0.6 for our typical von Karman 2S shedding mode. This result is supported by the flexible cylinder DNS simulations of Newman and Karniadakis (1997) where a 2-D freely vibrating cable had A_y/D of 0.52. For void structures found off lock-in conditions, we expect that the cylinder will not be oscillating at the maximum amplitude. For the void formation frequency ranges discussed in the previous section, Willden and Graham (2005) and Singh and Mittal (2005) predict vibration transverse amplitudes of approximately 0.1D to 0.2D.

Published data on stream-wise amplitudes are not as common. Maximum A_z/D amplitudes of 0.1 are published by Jauvtis and Williamson, (2004) for high Re_d VIV under locked in conditions. Singh and Mittal (2005) publish a much lower maximum value of approximately 0.01 for the maximum amplitude for low Re_d VIV. This corresponds to A_z of 2.286μm for our 0.02286cm diameter cylinder. For non-locked in conditions, we could expect peak stream-wise anti-node amplitudes on the order of 0.004 which corresponds to amplitudes of 0.9144 μm for our cylinder. Such small amplitudes would not be measurable by photo detectors such as the one used by Van Atta et al (1988) and Van Atta and Gharib (1987). Their photo detector was capable of measuring amplitudes as low as 10μm.

2.6. Comparison of the 'Void' Structure with Previously Observed Structures in the Cylinder Wake

The three-dimensional structures seen by Cimbala, Nagib and Roshko (1988) are a secondary instability occurring in the far wake, and do not have the point position of growth at the cylinder that the current structure has. Occasionally, similar patterns have been observed in our experiment far downstream. There is no mention of the detailed vortex dynamics that produces the "blobs" reported by Van Atta, Gharib and Hammache (1988) for direct comparison. However, the appearance of these 'blobs' does not share the rapid downstream growth that the 'void' structure has, and the vibration mechanism required for a 'voids' formation is different.

When comparing the known previous work with our visualizations, there is only one paper that discusses structures that have some similarities. The visualizations of the present study resemble the 'stable (in-phase) symmetric two sided dislocation' of Williamson (1992) at a Re_d of 260. These similarities include growth with downstream distance and an equal in-phase shedding frequency on either side of the large scale dislocation structure. However, there are significant differences in the three-dimensional structure. Williamson observed 'vortex linking' as a division of a vortex of one sign and a linking of that divided vortex with two vortices of same- signed vorticity on the other span-wise side of the dislocation structure. This 'vortex linking' was suggested to be partially responsible for a 'Λ-structure' that was readily visible in Williamson's visualizations. With our cylinder vibrations and lower Re_d, both the 'vortex linking' and 'Λ-structure' were not observed. Instead, another structure is seen, defined by a 'void' of tracer bubbles. We can see that this unique 'void' structure involves a vortex pinch-off between opposite-signed vortices of the Karman vortex street, and not an interaction of like signed vorticity as observed by Williamson (1992).

To our knowledge, we are the first to visualize this 'void' structure and pinch-off in the cylinder wake. We suspect that the reason others have not observed the ‘void’ phenomenon is because such structures can only occur on a flexible wire due to the formation of nodes and anti-nodes. They are quite difficult to find at the very high vibration modes of the flexible cylinder experiments of Van Atta and Gharib (1987) and Van Atta et al (1988) and both Newman and Karnaidakis (1996, 1997) and Brika and Laneville (1993) did not allow stream-wise vibration. Even at very small amplitudes, such vibrations can create large scale structures in the cylinder wake as reported by Van Atta et al (1988) and our investigation.

Conclusions

Using the hydrogen bubble flow visualization technique we have observed a vortex structure in the wake of a cylinder that has many unique features not discussed before. In section 2.4 we showed that vortex structures in the wake of the cylinder can sometimes contain a large-scale three-dimensional vortex structure we have chosen to call a 'void'. This is in reference to the vast reduction in number of tracer bubbles located within the structure. The lack of bubbles can persist for hundreds of diameters downstream. We have suggested a skeleton vortex structure which shows the pinch-off between opposite-sign Karman vortex street vortices. To our knowledge no one has visualized pinch-off interactions between both sides of the Karman vortex street before. This may be the first visualization of the pinch-off suggested by Roshko in 1976. We were able to correlate the span-wise location of this structure with a specific vibration event. This formation mechanism has not been previously suggested for any large scale structure formed in the wake of a circular cylinder.

The structure appears to be formed as a result of self-oscillatory wire vibration perturbations and not cylinder surface imperfections. We determined that these void structures form at an anti-node in transverse vibration and a node of the stream-wise vibration. For both locked-in and non locked-in cylinder vibrations we can calculate the anti-nodes and nodes of the cylinders vibration through the use of equations [2-11] and [2-12] of the vibration model we derived in Section 2.5.1. These equations require knowledge of the cylinder excitation frequencies; namely the vortex shedding frequency (f_{vs}) for transverse vibration and twice the shedding frequency ($2f_{vs}$) for stream-wise vibration (Jauvtis and Williamson 2004; Sarpkaya 2004). The model also requires knowledge of the cylinder natural frequencies of vibration (f_n) which are calculated using the cylinder tension and added mass. Although it is not highly important in determining node and anti-node locations, the model does require some estimate of the magnitude of the oscillating vortex shedding forces to determine accurate vibration amplitudes. We experimentally reproduced the vortex 'blob' structures of Van Atta et al (1988). Our vibration model was validated by using our experimental results to verify the result of Van Atta et al that the 'blobs' do occur at nodes in both stream-wise and transverse vibration.

For locked-in cylinder vibration, we found that the calculation for nodes and anti-nodes can be made much simpler. The detailed vibration model predicted the same result as was obtained from the well known mode shape equation [2-13] which is published in Blevins (1990) and Inman (2001) as well as most other texts on vibration. For void structures occurring under non locked-in conditions we must calculate nodes and anti-nodes using the vibration model, since this model accounts for the contribution from many mode shapes. These models depend greatly on shedding frequency and the cylinders natural frequencies of vibration.

When we compare the measured locations of 'void' formation with calculated anti-nodes and nodes of vibration, we see that 'void' formation correlates well with a specific vibration event. All void structures found on locked-in cylinders occur within +/- 4% of the calculated node in stream-wise vibration and the calculated anti-node in transverse vibration. All tolerances we discuss are given as a percentage of the cylinder length. For void structures occurring under non-locked in vibration conditions, 83.3% of voids were found within +/- 5% of the calculated stream-wise vibration node. All of these 'void' structures occurred within +/- 25% of the calculated stream-wise vibration node. This is primarily because many 'voids' are allowed to coexist simultaneously in the region surrounding the stream-wise vibration node and transverse vibration anti-node. We speculate that this results from a vortex dynamics interaction between the large scale structures, or some interaction between adjacent modal responses of the cylinder vibration.

We determined that vibration must be occurring because voids occurred near, or inside lock-in. In addition, they were quite difficult to find beyond the 1st mode of transverse cylinder vibration. Due to the strong dependency of void formation on vibration mode shapes and their modal responses, we can conclude that void formation is most strongly dependent upon the excitation frequencies of vortex shedding, and their relation to the cylinders natural frequency. Our vibration model also shows that the location of nodes and anti-nodes is not strongly dependent on the magnitude of the dynamic forces imposed by vortex shedding. Since these forces are highly dependent on the Reynolds number, based on diameter (Re_D), this is supported by the finding that our 'void' structure was not highly dependent on Re_D. The most notable Re_D dependency is that oscillating forces must exist since Karman type vortex shedding must be occurring. Otherwise we found the structure between Re_D of 57 and the largest experimental Re_D of 185.

We should expect peak lock-in vibration amplitudes of A_y/D of 0.35 (80μm) and A_z/D of 0.01 (2.3μm). Peak vibration amplitudes outside of lock-in should be approximately A_y/D of 0.1 (23μm) and A_z/D of 0.004 (1μm). Unfortunately, we did not have sensitive enough instruments to directly measure such small distributed vibrations along the span of our wire in a water tunnel.

We also verified the use of hydrogen bubbles for seeding of VIV experiments in Section 2.3. The onset of shedding was reproduced at the typical Re_d value of 47. Typical characteristics of the wake inside and outside lock-in matched very well with results from VIV literature. In addition, we showed that the vortex street is capable of trapping the bubbles in their cores and that buoyant bubble rise is inconsequential after shedding has begun. We recommend the use of hydrogen bubble visualization for use in cylinder flow research.

References

Anagnostopoulos P, Bearman PW (1992) Response Characteristics of a vortex-excited cylinder at low Reynolds numbers. J. Fluids and Structures 6:39-50.

Apps C (2001) A Study of Synthetic Fence Jets Using I.C.V. Master's Thesis, University of Alberta, Edmonton.

Apps C, Chen T, Sigurdson L (2003) Image Correlation Velocimetry Applied to Discrete Smoke-wire streaklines in Turbulent Pipe Flow. Experiments In Fluids 35:288-290.

Blevins, R.D. (1990) Flow-Induced Vibration: Second edition. Von Nostrand Reinhold, New York.

Brika D Laneville A (1993) Vortex-Induced Vibrations of a long flexible circular cylinder J. Fluid Mechanics 250:481-508.

Chang WK, Pilipchuk V, Ibrahim RA (1997) Fluid Flow-induced nonlinear vibration of suspended cables. Nonlinear Dynamics 14: 377-406.

Cimbala JM, Nagib HM, Roshko A (1988) Large Structure in the far wakes of two-dimensional bluff bodies. J. Fluid Mechanics 190:265-298.

Crow SC (1970) Stability theory for a pair of trailing vorticies. AIAA Journal 8:12:2172-2179.

Eisenlohr H, Eckelmann H (1989) Vortex Splitting and its Consequences in the vortex street wake of cylinders at low Reynolds Number. Physics of Fluids A1 2:189-192.

Gilbert S, Sigurdson L (2005) Hydrogen bubble flow visualization of a self-oscillating cylinder vortex street "void". Gallery of Fluid Motion, Physics of Fluids 18:7.

Govardhan RN, Williamson CHK (2006) Defining the 'modified Griffin plot' in vortex-induced vibration:revealing the effect of Reynolds number using controlled damping. J. Fluid Mechanics 561:147-180.

Govardhan RN, Williamson CHK (2004) Modes of Vortex Formation and frequency response of a freely vibrating cylinder. J. Fluid Mechanics 420:85-130.

Griffin OM, Ramberg SE (1976) Vortex Street wakes of vibrating cylinders. J. Fluid Mechanics 66:553-576.

Griffin OM, Ramberg SE (1974) Vortex Shedding from a cylinder vibrating in line with an incident uniform flow. J. Fluid Mechanics 75:257-271.

Hammache M, Gharib M (1991) An Experimental Study of the Parallel and Oblique vortex shedding from circular cylinders. J. Fluid Mechanics 232:567-590.

Huarte H, Bearman PW, Chaplin JR (2006) On the force distribution along the anis of a flexible circular cylinder undergoing multi-mode vortex-induced vibrations. J. Fluids and Structures 22: 897-903.

Inman. D.J. (2001) Engineering Vibration: Second Edition, Prentice Hall, New Jersey. pp. 183-188, 433-487.

Jauvtis N, Williamson CHK (2004) The Effect of two Degrees of Freedom on Vortex-Induced Vibration at Low Mass and Damping. J. Fluid Mechanics 509:23-62.

Jiang B (1992) The Acceleration of a Single Bubble Rising from a Nozzle in Water. Masters Thesis, University of Alberta, Edmonton.

Jiang B, Varty RL, Sigurdson LW (1993) Acceleration of a single bubble rising from a nozzle in water. American Society of Mechanical Engineers, Fluids Engineering Division Gas-Liquid Flows 1993 165:161-169.

Kim W-J, Perkins NC (2002) Two-Dimensional vortex induced vibration of cable suspensions. J. Fluids and Structures 16:2:229-245.

Newman DJ Karniadakis GEM (1997) A direct numerical simulation study of flow past a freely vibrating cable. J. Fluid Mechanics 344:95-136.

Newman DJ Karniadakis GEM (1996) Simulations of flow over a flexible cable: A comparison of forced and flow-induced vibration. J. Fluids and Structures 10:439-453.

Norberg C (1994) An Experimental investigation of the flow around a circular cylinder: Influence of Aspect Ratio. J. Fluid Mechanics 258:287-316.

Ramberg SA (1983) The Effects of Yaw and Finite Length upon the Vortex Wakes of stationary and vibrating circular cylinders. J. Fluid Mechanics 128:81-107.

Roshko A (1976) Structure of Turbulent Shear Layer Flows: A New Look. AIAA J. 14:1349-1357.

Sarpkaya T (2004) A critical review of the intrinsic nature of vortex-induced vibrations. J. Fluids and Structures 19:389-447.

Sarpkaya T (1978) Fluid Forced on Oscillating Cylinders. J. of the waterway port coastal and ocean division WW4:275-290.

Schatzle P (1987) An Experimental Study of Fusion of Vortex Rings, Ph.D. Thesis, California Institute of Technology, Pasadena California.

Singh SP, Mittal S (2005) Vortex-Induced oscillations at low Reyonds numbers: Hysteresis and vortex-shedding modes. J. Fluids and Structures 20:1085-1104

Skop RA, Balasubramanian S (1997) A new twist on an old model for vortex-excited vibrations. J. Fluids and Structures 11:395:412.

Van Atta C, Gharib M (1987) Ordered and Chaotic Vortex Streets behind a circular cylinder at low Reynolds Numbers. J. Fluid Mechanics 174:113-133.

Van Atta CW, Gharib M, Hammache M (1988) Three-dimensional structure of ordered and chaotic vortex streets behind circular cylinders at low Reynolds numbers. Fluid Dynamics Research 3:127-132.

Willden RHJ, Graham JMR (2006) Three distinct response regimes for the transverse Vortex-Induced Vibrations of circular cylinders at low Reynolds numbers. J. Fluids and Structures 22:885-895.

Willden RHJ, Graham JMR (2001) Numerical prediction of VIV on long flexible circular cylinders. J. Fluids and Structures 15:659-669.

Williamson CHK (1992) The Natural and forced formation of spot-like ‘vortex dislocations’ in the transition of a wake. J. Fluid Mechanics 243:393-441.

Williamson CHK (1989) Oblique and Parallel modes of Vortex Shedding in the wake of a circular cylinder at low Reynolds Numbers. J. Fluid Mechanics, 206:579-627.

Williamson CHK, Govardhan RN (2004) Vortex Induced Vibrations. Annual Review of Fluid Mechanics, 36:413-455.

Zhou CY, So RMC, Mignolet MP (2000) Fluid Damping of an elastic cylinder in a cross flow. J. Fluids and Structures 14:303-322.

Chapter 3. Design of a Backward-Facing Step Flow Control Device

3.1. Introduction

Mankind has been involved in manipulating flows for centuries. A review of the immense flow control literature is given in the text by Gad-el-Hak (2000). The three fundamental types of flow control include passive, active and reactive control. Passive control typically involves the use of some time-invariant means for obtaining a control objective with no external energy input. Active control, also termed open-loop control, uses a pre-determined time-varying actuation to manipulate the flow with external energy input. Finally, reactive control uses a sensor measurement to calculate an open-loop feed forward actuation or a closed-loop feedback actuation. Our backward-facing step control device is designed as an active or open-loop control device. The actuator will be the first experimental use of span-wise variations in the actuation with various distributions, wavelengths and phase relationships that have been successful in numerical experiments of Kang and Choi (2002). Generic specifications of this actuator are given in Section 3.2. In this design procedure, we select the actuation technology in Section 3.3, and give a detailed description of the fabricated actuators in Section 3.4.

3.1.1. The Backward-Facing step

The backward-facing step geometry has been a benchmark flow in fluid mechanics for the study of recirculation bubbles. Advances in the control of this flow geometry can be applied to a wide variety of industrial and aeronautical flows. The recirculation bubble, more commonly described as a reattaching shear layer, has seen a vast amount of research. Studies into the classical flow configuration, without any type of control, are quite numerous. Adams and Johnston (1988a) measure both pressure and turbulence statistics and provide a correlation to relate measured pressure data into turbulent shear stress information in the near-wall region at reattachment. Adams and Johnston (1998b) provide experiments showing that the reattachment length of a separating turbulent boundary layer is longer than both transitional and laminar boundary layers.

Lee and Sung (2001) provide detailed measurements on the wall pressure fluctuations plotted versus the stream-wise and span-wise directions. They reproduced the result of Mabey (1972) that wall pressure fluctuations pass through a well marked maximum, just prior to reattachment. This result is widely used in feed-back control experiments (Becker et al, 2005; Henning and King, 2007) due to its relatively rapid nature for determining the reattachment length (X_R). In general, time mean values of the reattachment length ($\overline{X}_R$) are presented by researchers using a wide variety of measurement techniques. In addition to surface pressure fluctuations, laser Doppler anemometry (Armaly et al, 1983), surface oil techniques (Wengle et al, 2001; Hasan, 1992), particle image velocimetry (Yosioka et al, 2001a; Yosioka et al, 2001b), and tufts (Roos and Kegelman, 1986) are used to determine $\overline{X}_R$. However none of these measurements fully illustrate the features of the reattachment length which has been shown to have both span-wise and temporal fluctuations (Le et al, 1997; Armaly et al, 1983). Such span-wise variations are idealized by the dashed line for $X_R(z,t)$ in Figure 3.1.

Parameters used to describe a backward-facing step flow include:

$$\mathrm{Re}_h = \frac{hU_\infty}{\nu},\ St_h = \frac{f_h h}{U_\infty},\ \mathrm{Re}_\theta = \frac{\theta U_\infty}{\nu}, St_\theta = \frac{f_\theta \theta}{U_\infty},\ ER = \frac{H}{(H-h)},\ AR = \frac{L}{h}$$

These parameters are the Reynolds and Strouhal numbers based on momentum thickness θ and step height h. ER and AR is the expansion and aspect ratios of the step, where h is the step height, H is test section height after flow expansion and L is the span. These terms are shown in the backward-facing step schematic as shown in Figure 3.1. The backward-facing step geometry, as designed in Section 3.5 will be quite similar to the one illustrated in this figure.

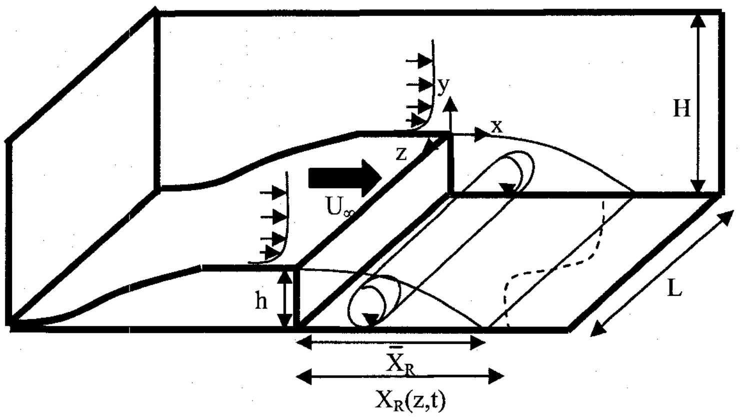

Figure 3.1: Schematic of Backward-facing Step flow

Dashed line shows span-wise variation in the reattachment length. The recirculation bubble denoted by the cylinder will also exhibit span-wise variations.

3.1.2. Previous Backward-Facing Step Flow Control

Passive control techniques are based on the realization that proper promotion of turbulence intensity in the inlet of a backward-facing step has been shown to have a reduce the reattachment length. Isomoto and Honami (1989) use tripping cylinders increase the turbulence intensity in the inlet flow. Similarly, Neumann and Wengle (2003) use a surface mounted control fence to promote turbulence intensity in the inflow to the backward-facing step. However, Neumann and Wengle concluded that their passive method was not as effective as active control methods.

Most of the open-loop and closed-loop strategies for the forcing involve using some type of single frequency forcing. There is a debate regarding whether St_h or St_θ is the proper dimensionless quantity for describing the optimal forcing frequency. The data does show two possible optimum instability frequencies, termed the shear layer mode and the step modes as stated by Hasan (1992). The shear layer mode has an optimum value determined by $St_\theta \approx 0.012$ and a step mode at $St_h \approx 0.2$. Hasan showed that the shear layer, (or Kelvin-Helmholtz), mode of instability is reduced to the step mode through a pairing of the original shear layer vortices. Sigurdson (1995), denoting this as the 'shedding'-type of instability, showed that this scaling is very prominent in many flow geometries. In this case, merged shear layer vortices interact with their images due to the wall and the instability is much like von Karman vortex shedding from a cylinder. Researchers have cited both of these frequencies to be optimal in reducing the reattachment length. Bhattacharjee et al (1986) cite that $St_h \approx 0.2 \sim 0.4$ is an optimum frequency range, which is consistent with the findings of Hasan. Yoshioka et al (2001), Roos and Kegelman (1986), Kang and Choi (2002) all cite the step mode as their optimum frequency for reducing the reattachment length. The shear layer or Kelvin Helmholtz mode has been cited by Chun and Sung (1996, 1998), Wengle et al (2001) as the optimal method for increasing mixing or reducing the reattachment length.

To combine these two instability modes into a single actuation, Kim et al (2007) used dual frequency forcing to reduce the reattachment length further. Kim et al. gave the following expression or this forcing:

$$V_A = V_{A,peak,1}\sin\left(2\pi f_1 t\right) + V_{A,peak,2}\sin\left(2\pi f_2 t - \phi\right) \qquad [3\text{-}1]$$

In this relationship, they combined the primary Helmholtz instability frequency with various sub-harmonics and harmonics. The two waveforms were offset by the phase ϕ.

The forcing amplitudes in the literature are quite varied. Blowing and suction type actuation studies found in the literature have peak velocities of between $0.02U_\infty$ to $0.3U_\infty$ for active control. For closed-loop systems, actuation peak velocities can be significantly reduced to $0.002U_\infty$ (Becker et al, 2005). Flapping amplitudes have been on the order of 1% of the momentum boundary layer thickness (Roos and Kegelman 1986; Lai et al 2002).

The use of span-wise variations in the actuation profile velocity is less prominent in the literature. In their numerical experiments using optimization based control of a backward-facing step flow, Kang and Choi (2002) found that they could prescribe an open-loop forcing that would closely mimic the results obtained from their optimization. Their span-wise variation in forcing was prescribed as:

$$V_A(z,t) = \sin\left[\frac{2\pi}{L_z}(z + z_p(t))\right] V_A(t) \qquad [3\text{-}2]$$

The optimal span-wise actuation wavelength is an L_z 4h and they prescribed various time varying phase relationships $z_p(t)$. This term was given 4 definitions by Kang and Choi. The most effective phase definition was a quasi-random phase definition which assigns a random value for $z_p(t)$ that has a dependency on its previous values. This result simulates the actuation profile they obtained in their closed-loop sub-optimal Navier Stokes based optimization technique. No experimental research has achieved this level of control over span-wise wavelengths and time varying phase relationships. Henning and King (2007) segment their forcing into 4 different actuation velocities controlled by individual loudspeakers. They find that they can maintain different span-wise reattachment lengths through the use of open-loop and closed-loop control. Chun and Sung (1999) created span-wise variation in their forcing by putting thin tape of different lengths to block segments of their uniform actuation slot of previous experiments (Chun and Sung, 1996, 1998). They stated that such variations proved to be no more effective than uniform forcing. The reason for this could have been that they appeared not to modify wavelengths and phase relationships of their selective taping of the actuation slot. Instead, they focused on the ratio of taped width, to the width of the open sections.

3.1.3. The Desired Actuation

In light of the current literature, it is advisable to design the actuator to be capable of creating the following actuation profile which is a combination of equations [3-1] and [3-2]. When we combine these relationships, we get an actuator capable of forcing with N_f different frequency contents, amplitudes (A_n) and phases (ϕ_n). The frequency contents would include harmonics and sub harmonics of the Kelvin Helmholtz shear layer instability mode (Kim et al (2007), where sub harmonics correspond to the step mode of instability. We can also add periodic span-wise distributions of this forcing as idealized as a sine wave in [3-3]. Ideally, it would be desirable to have real-time control over the span-wise distribution of velocity, span-wise wavelength (L_z), the time varying span-wise phase (z_p) and the various forcing frequencies (f_n), amplitudes ($V_{A,peak,n}$) and phases (ϕ_n). The expression for this ideal forcing is:

$$V_{act}(z,t) = \sin\left[\frac{2\pi}{L_z}(z + z_p(t))\right]\sum_{n=1}^{N_f} V_{A,peak,n}\sin(2\pi f_n t - \phi_n) \qquad [3\text{-}3]$$

As we stated earlier, when completed this actuator will provide the first experimental results for a wide variety of span-wise distributions, wavelengths (L_z), and time varying phase relationships. It could also combine these span-wise distributions with the advantages of forcing with multiple frequencies to provide even further contributions to the existing literature on reattaching shear layers of back step flows.

In the more distant future, we could use the optimization strategies of Koumotsakos and Milano (2002) or Navier-Stokes based optimal and suboptimal optimization based strategies (Bewley et al, 2001; Choi et al, 1999; Kang and Choi, 2002). It could also be used to further explore the effects of span-wise varying forcing in process control based optimal control techniques of Henning and King (2007). In addition, all such techniques could be applied to many other flow geometries if the actuator is portable.

3.2. Overview of Experiment Design

A schematic of the fabricated components of the experiment is given in Figure 3.2a. Firstly, the step module has a detailed profile with some technical content in its design. The details of this profile will be discussed in Section 3.5.1. The dye reservoir module and other visualization systems will be discussed in more detail in Section 3.5.2. The most intricate and detailed portion of the design is the Actuator Module. There is a wealth of knowledge surrounding the fabrication and operation of such modules, but there is still room for contributions to the current literature. In Section 3.3 we will discuss the technology selection process for the actuator. In Section 3.4 we will describe the attributes and details behind the actuator and its fabrication. We will also present data from the testing of a prototype actuator in Section 3.4.2.

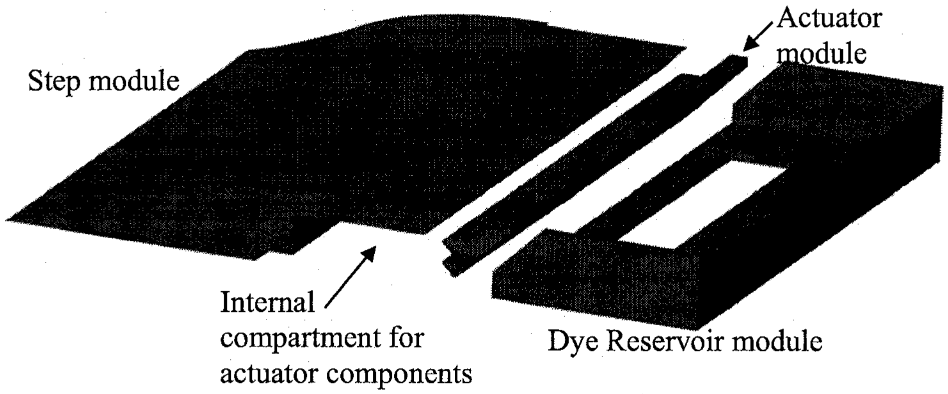

Figure 3.2. Experimental Components

The backward-facing step has a height h=5.54cm (2.18 in) and a span (h) of 45.72 cm (18 in). This gives an aspect ratio (AR=L/h) of the step of 8.25. Since the widely accepted aspect ratio to ensure 2-Dimensional flow over a step is 10, we expect our flow to have some degree of 3-Dimensional component. The width of the actuation slot is 44.45 cm (17.5 in) giving an actuation aspect ratio of 8. Where the actuation aspect ratio is defined in terms of the entire actuated span (L_a) and the step height (h) as:

$$AR_A = \frac{L_a}{h}.$$

The full height of the test section (H), after the expansion, is 25.4 cm (10 in). The expansion ratio (ER=H/H$_i$) is 1.25 where H$_i$ is the inflow test section height (H$_i$ =H-h).

Testing of a prototype actuator showed that the forcing frequencies with the purest frequency content lie below 3 Hz. We will show in Section 3.4.3 that this corresponds to a maximum Re$_h$ of 16,750 for forcing at the shear layer mode instability frequency and 46,100 for forcing at the step mode of instability. It is conceivable to force at up to 6.25 Hz, however at this frequency, the servo only receives 8 motion updates per cycle which results in relatively poor performance. Since the published data of forcing with multiple frequencies from Kim et al (2007) was not available during prototype testing, this potential use of the actuator was not tested. However, the testing that was done suggests that at frequencies lower than about 1.5 Hz the actuators should perform well under multiple frequency forcing conditions. This corresponds with a maximum Re$_h$ of 9,000 where the minimum Re$_h$ encountered in our study will be approximately 2000 to 3000 as this is the value where the reattachment length becomes relatively independent of Re$_h$ for our expansion ratio (Adams and Johnston 1998b). We will discuss the results of the prototype testing in Section 3.4.2.

The actuation system is designed to produce a discrete approximation to continuous span-wise actuation wavelengths (L$_z$) of 0.5h, 1h, 1.5h … 7.5h and 8h. It was designed to produce a resolution of 8 different velocities per wavelength. For some wavelengths it will be possible to obtain 16 different actuation velocities per actuation wavelength. In Figure 3.3, for a wavelength of 8h, we can see the improvement in the resolution of span-wise actuation when using 16 velocities as opposed to 8. Resolution of 16 trials can be done for L$_z$ values of 1h, 2h, 4h, 6h, and 8h. Small scale, relatively inexpensive, and easily fabricated upgrades could make it possible to control the 3h, 5h and 7h wavelengths with a span-wise wavelength resolution of 16. This actuator is not necessarily limited to the sinusoidal span-wise actuation distributions. Conceivably it can create any periodic waveform which can be adequately resolved in the discrete manner of the actuator. Combined with various relationships for the time varying phase, $z_p(t)$, we will be the first to experimentally implement such variations in an actuator on a backward-facing step flow. The value of such span-wise variations has been shown numerically by Kang and Choi (2002). It has also been shown to work well at experimentally modifying the vortex structure in a planar jet as done by Sakakibara and Anzai (2001)

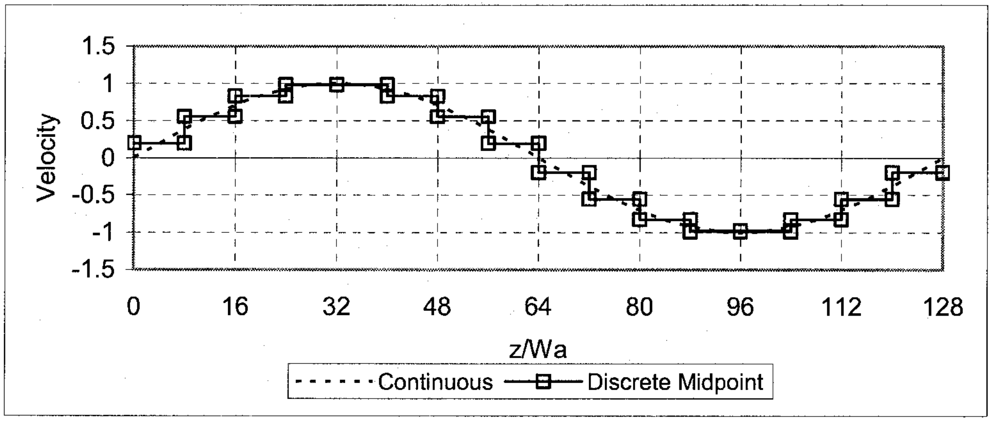

a) Resolution of 16 Different Velocities

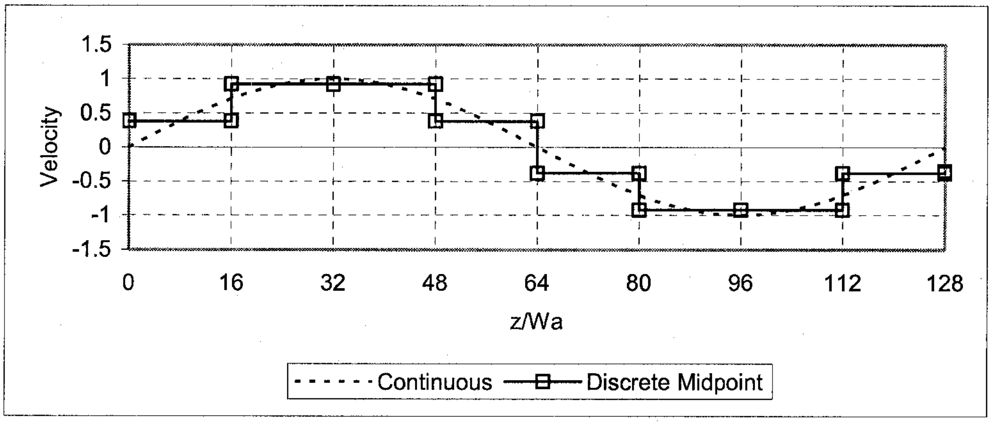

b) Resolution of 8 different Velocities

Figure 3.3. Span-wise Variation of Actuation

3.3. Actuation Technology and Selection

We first begin the design of our actuator by searching the current literature on effective means for actuation. In their backward-facing step experiments Roos and Kegelman (1986) used span-wise uniform flapping at the separation point with an amplitude of 2 mm. The flap was driven by electromagnetism, and the bulk fluid was air. Lai et al (2002) used a flap connected rigidly to a linear shaker driven with very similar amplitudes as Roos and Kegelman. Micro-Electro-Mechanical systems (MEMS) based flapping applications have not yet been applied to a backward-facing step. Due to their relatively cheap costs, and their inherent advantage for giving a high resolution span-wise distribution of forcing, they are quite attractive. A detailed review of MEMS based solutions to actuation and sensing problems is given by Lofdahl and Gad-el-Hak (1999). Peacock et al (2004) used the bi-layer technique as discussed by Lofdahl and Gad-el-Hak to manufacture arrays of flapping actuators. These arrays are capable of giving maximum flapping deflections of 25μm below 30Hz reducing to about 4μm at 200Hz.

The use of plasma actuation has received increased interest in the recent literature. Moreau (2007) gives a detailed description of the use of plasma actuators on various flow geometries. An electric or ionic wind is generated by plasma discharges that were generated in air. Such winds are easily installed to energize boundary layers, delay flow separation, or promote reattachment. Laberque et al (2007) use plasma actuators to induce separation at the outlet of a turbulent jet. With the typical construction used by Moreau and Laberque et al, the electric winds cannot completely reverse in direction but fluctuations from a mean velocity can be obtained. Such actuators can be built in very small scale and require no moving mechanical parts, so they are particularly suitable for MEMS based applications.

Blowing and Suction type actuation is the most widely used actuation type for the forcing of a backward-facing step experiments (Becker et al 2005;

Bhattacharjee et al 1986; Chun and Sung 1996, 1998, 1999; Hasan 1992; Henning and King 2007; Kim et al 2007; Wengle et al 2001; Yoshioka et al 2001a, 2001b). This is primarily due to the ease of construction and the wide frequency and amplitude ranges obtainable with this technique. In addition, this type of actuation has seen considerable attention in numerical simulations (Saric et al 2005; Dejoan et al 2005; Dejoan and Leschziner 2004; Choi et al 1999; Kang and Choi 2002). Both open-loop and closed-loop control techniques have been very successful at modification of the reattachment length using frequencies and amplitudes discussed in the previous section. Specialized techniques, termed zero-net mass flux (Gordon and Soria 2002) and synthetic jet actuators (Smith and Glezer 1998) have also been developed that have unique actuation properties. Design and modeling of MEMS based synthetic jets are discussed by Lockerby and Carpenter (2004). Lofdahl and Gad-el-Hak (1999) discuss a method to design a MEMS based actuator using reservoirs and micro valves to create blowing and suction type distributed actuations. Sakakibara and Anzai (2001) give distributed blowing and suction along the separation line of a planar jet. They use many small servo motors to drive syringes at different velocities to create a square-wave span-wise distribution of velocity which proves quite effective.

Smart materials are widely used in actuators. A detailed review of smart materials as used in sensors and actuators is discussed by Tzou et al (2004). Piezoelectric materials and shape memory alloys (SMA) are the most commonly used smart materials. Piezoelectric materials are used in the manufacture of synthetic jet actuators. These materials expand or contract in response to variations in the strength of an electric field. The actuation stroke of piezoelectric is relatively small but lever systems can be used to amplify oscillation amplitudes to millimeter scales (Tzou et al, 2004) with a flapping motion. Shape memory alloys drastically change shape when alloy temperature switches between the martensite or austenite phases. The phase transformations allow large forces and displacements. However, SMA's are limited to a maximum oscillation frequency of about 1Hz due to complexity of rapidly heating and cooling the alloy (Faulkner 2006). These alloys can also be subject to significant hysteresis as the transformation temperatures are not necessarily equal for martensite and austenite. (Tzou et al, 2004). Liang and Rogers (1997) discuss the use of SMA's in the design of actuators. Many other materials such as electrostrictive and magnetostrictive materials (Zhou 2004), or polymer hydrogels (Santulli et al 2005) show potential for use in future actuators. Unfortunately the use of these materials would require significant time and funds to develop the technologies into useful actuators.

3.3.1. Shortlist of Suitable Actuation Technologies

The first limiting design choice was the decision to use the High Speed Water Tunnel in the Vortex Fluid Dynamics Laboratory at the University of Alberta. In Section 3.4.3 we show how the use of water will decrease the required frequencies to within the limits of our actuators for a very wide range of Re_h. Lower frequency actuators tend to be cost effective and the researcher can get a great understanding of the flow by simple qualitative and quantitative visualization techniques.

Unfortunately, the choice of water immediately limits the types of actuators we can use. MEMS actuators would be problematic due to the oxidation of the silicon in water and plasma actuators can only form electric winds in air. Costly piezoelectric materials are limited in their actuation stroke and their relatively high voltages could be a safety concern in damp environments. Shape memory actuators are restricted to a maximum forcing frequency of 1Hz under ideal conditions. SMA use would be complicated further by the wide variety of water temperatures throughout the course of a calendar year. Therefore, the limitations of all these options outweigh their unique benefits. Hence, for our experiment we are limited to the more traditional actuation types. These actuation types are typically flapping, or blowing and suction.

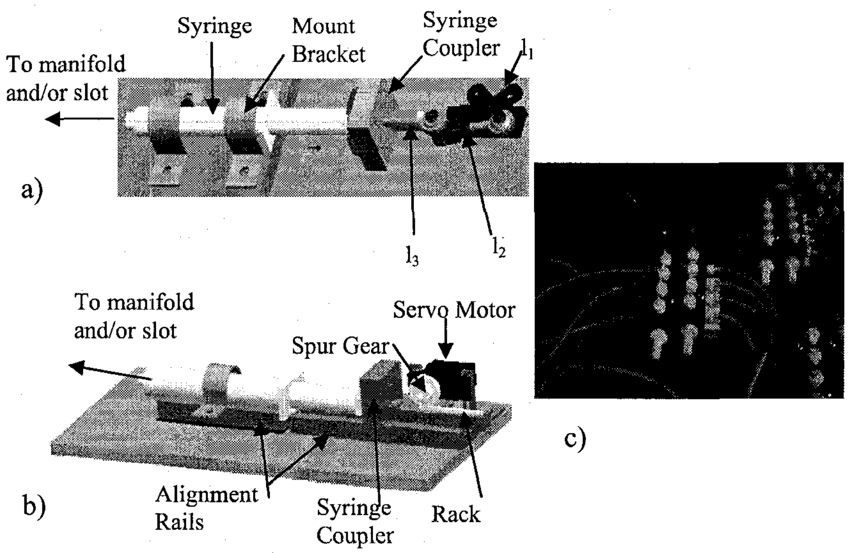

Figure 3.4: Potential Blowing and Suction Actuators

a) Slider-crank linkage based system
b) Rack and pinion based system
c) Potential Distribution manifold for forcing many slots with 1 actuator

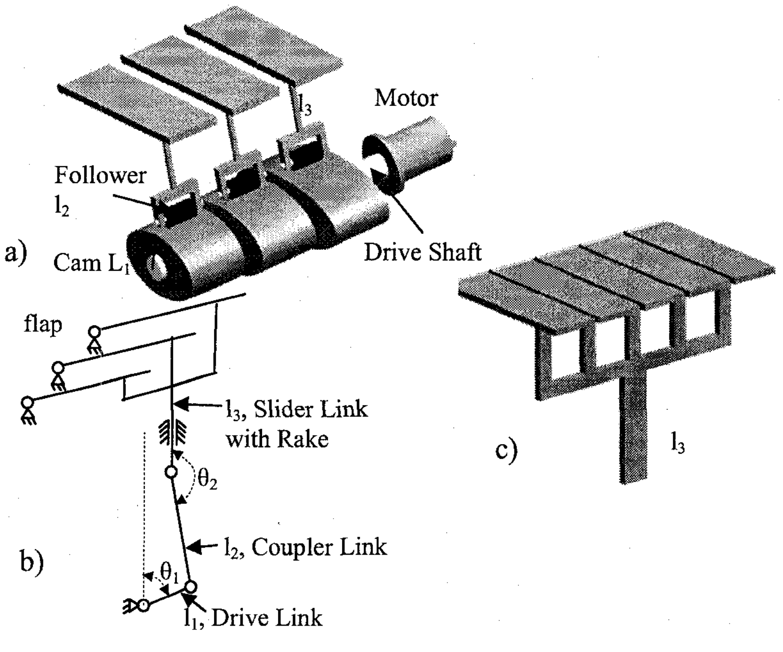

Figure 3.5: Potential Flap Designs for Actuation

a) Single motor driveshaft cam-follower system
b) Schematic Slider-crank linkage system with flap rake
c) A potential rake for forcing many flaps with 1 actuator

The mechanical systems used in the designs of these actuation types are quite similar. They generally have some type of oscillating motor, or shaker to create the oscillation. Connected to this motor, there is a mechanical force transmission system (FTS) which modifies the motion of the motor into a desired actuation. Typical FTS include rack and pinion, cam-follower and linkage systems. Then different FTS connect with their corresponding flap or blowing and suction slot, generically termed a discrete actuation location (DAL).

All of these systems can be applied to both the actuation types with their own relative advantages. Once we have selected the FTS, we must also select the number of servo motors used to drive the systems. Regardless of the number of motors, all designs would have real-time control over the oscillation amplitudes ($V_{A,peak,n}$), the relevant optimal frequency contents of forcing (f_n) and phase between the waveforms (ϕ_n). These terms are all described in the desired forcing function in equation [3-3] of section 3.1.3.

The number of motors used would decide whether we had real-time control over the span-wise wavelength (L_z) and time dependent span-wise phase (z_p). Motor design A, the most costly option, is to connect each DAL to its own FTS and servo motor. This would allow real-time control of all actuation parameters including the span-wise wavelength. Design C, the last design considered, involves using one servo motor to drive many DALs by use of a force splitter. For the blowing and suction type, a force splitter would be a distribution manifold, as seen in photograph of Figure 3.4c. For the flapping actuation type, a rake system can be used to split the linear motion into many equivalent DALs. This can be seen in the solid model of Figure 3.5c and idealized in the linkage schematic in Figure 3.5b. The number of DALs per servo is another design choice. These designs do not allow real-time control of the span-wise wavelength, but they do allow real-time control over the time varying span-wise phase.

3.3.2. Final Selection of Actuator Technology

As our final actuator, we will use the blowing and suction type, driven by rack and pinion force transmission systems. To drive all 128 slots, we require 22 rack and pinion systems to drive syringes as seen in Figure 3.4b. Each of these syringes will be connected to its own 8-outlet distribution manifold as seen in Figure 3.4c. The tubes will then go from the distribution manifold to the backward-facing step actuator module as shown in Figure 3.2 of Section 3.2. For certain wavelengths, tubes may go from the manifolds to an extra tube reservoir which will be discussed in Section 3.4.5. The detailed dimensions of the tubing network connecting the components are also discussed in this section. We discussed the specifications of this actuator in Section 3.2. To arrive at this decision, a decision matrix was applied to the designs to compare the various technologies and options. The criteria are summarized in Table 3.1.

Quality of Actuation	Score
time domain	
frequency limits	5
many freq contents	5
lack of nonlinearity	5
Actuation amplitude	5
span domain	
Lz	5
zp(t)	5
Subtotal	30

Operational	Score
Ease of Use	5
Ease of Maintenance	5
Subtotal	10
Fabrication	
cost	10
Ease of Fabrication	5
Subtotal	15
Max score	**55**

Table 3.1: Actuation Selection Criteria

Firstly, we found that flapping designs were found to score lower in the decision matrix than the blowing and suction designs. This is mainly because they performed poorly in the operational and fabrication related criteria. All the moving components of the flapping actuators must be placed in quite close proximity to force all 128x 2.5 mm wide flaps with great accuracy. Secondly, possible upgrades to the system would also be much more costly and may require a completely new design and fabrication process. Conversely, the blowing and suction type actuators can be placed almost arbitrarily as long as the tubing networks are fluid dynamically similar. Hence, fabrication, operation maintenance and even upgradeability are much simpler.

Secondly, we determined that a rack and pinion FTS scored higher than the linkage and cam-follower systems. They scored higher than cam-follower designs because of the complexity and costs associated with the fabrication of many different custom built cam profiles. When compared with linkages, the rack and pinion system improves the actuation quality as it eliminates the non-linearity of linkages. The non-linear relationship of the linkage system is derived in machinery design textbooks (Norton 2001):

$$V_{Link} = -|l_1|\dot{\theta}_1 \sin\theta_1 + |l_1|\dot{\theta}_1 \cos\theta_1 \tan\theta_2 \qquad [3\text{-}4]$$

Not only does the slider velocity depend on the angular velocity of the drive link $\dot{\theta}_1$, but it also depends on the actual angular positions θ_1 and θ_2 of the links L_1 and L_2 which have lengths of $|L_1|$ and $|L_2|$. These terms are shown graphically in Figure 3.5b. For a rack and pinion system, the velocity of the rack can be accurately described by the tangential velocity of the pinion gear of radius r:

$$V_{Rack} = r\dot{\theta}_1 \qquad [3\text{-}5]$$

Therefore, the rack and pinion will only have the non-linearity that exists due to the servo motor itself. This non-linearity is quite minimal at the lower frequencies where the bulk of the experiments will be completed.

Thirdly, as a compromise between cost and actuation functionality, it was decided to split the actuation flow from the rack and pinion syringes through 8-outlet distribution manifolds. In doing this we reduce the number of required motors from 128 to 22 at a significant cost savings. Since the actuators can be located somewhat arbitrarily we can upgrade this design to the motor design A, at the expense of fabricating 106 more rack and pinion actuators. This would allow our actuator to have real-time control over all terms of the desired forcing equation [3-3] as seen earlier in Section 3.1.1, and provide a discrete approximation of the continuous span-wise distribution of velocity. For the initial experiments, the manual plug and play design for changing the span-wise wavelength is deemed acceptable.

3.4. Actuator Components, Specifications and Features

In Section 3.3, we described in general the components of the actuation system. In this section, we will discuss in much more detail the components selected for the force transmission system and the tubing network. In Section 3.4.1 we discuss the dimensions and details of the rack and pinion actuator. Details of the tubing network which connects the rack and pinion actuator to the in-step actuator slot module are also given. We also discuss the communication and data gathering electronics use to control, monitor and power the 22 different servo motors. During the design phase, we tested a prototype actuator and got preliminary performance data. This data, along with a discussion is presented in Section 3.4.2. Since we know the actuator frequency limits from these tests, we can calculate that our maximum Re_h of 16,750 is possible when forcing at the Kelvin Helmholtz, or shear layer instability frequency. For the step mode of instability, our maximum Re_h is 46,100. The details of this calculation, and the value of using water as our experimental fluid, are presented in Section 3.4.3. In Section 3.4.4 we discuss the possible actuation amplitudes as they compare with published values. Finally, in Section 3.4.5 we discuss the span-wise variation of actuation velocity.

3.4.1. Overview of Actuator Components

In Figure 3.6a, we show the locations of actuator components as they relate to the layout of the other experimental components. From the figure we can see that each actuation system requires the actuator, a distribution manifold and the 2 possible final tube destinations. Namely, the actuator slot module or an extra tube reservoir required for certain wavelengths. Each component is connected by a network of flexible tubing. A photograph of a manufactured actuator is found in Figure 3.6b and a solid model is given in Figure 3.6c.

The rack and pinion force transmission system is driven by a Hitec® HS-225MG analog servo motor, selected for its superior performance when compared to the weaker and slower standard analog servos. The added expense of the digital servos, which could potentially have a much greater maximum forcing frequency and Re_h, was deemed unnecessary. The rack, which is driven at the tangential velocity of the 1" pitch diameter pinion gear, is mounted on a low friction slider. The slider allows the connection of coupler which forces the syringe piston to move with the same motion as the rack.

Low friction 20 mL glass syringes from Popper and Sons, Inc. are used in the actuator to give quite significant actuation velocities. These syringes have plungers with diameters of 1.958 cm. The syringe is mounted on an alignment rail using rigid tube clamps. The alignment rail was identical to the slider rail making it easy to ensure proper orientation of the syringe casing with its plunger. This avoids unnecessary radial forces between the syringe casing and the plunger. Such forces, if severe enough, cause the piston motion to lock-up and the servos to stall, stopping all actuation. Although lock-up was common in the initial prototypes, we were able to eliminate it completely using careful design, testing and fabrication techniques.

The syringe is then connected to the step or an extra tubing reservoir by a tubing network. The schematic of this network is seen by the schematic in Figure 3.7, and is not intended to be to scale or show experimental layout. The symbols and length and diameter values for this tubing network are given in Table 3.2. Re-enforced 3/8 inch inner diameter tubing is clamped to the metal luer lock fitting of the syringe. The other end of this tubing feeds into a commercially available 8 outlet manifold. The manifolds used are shown in the photograph in Figure 3.4c. These manifolds split the flow from the syringe into 8 branches of 1/8 inch inner diameter tubing. The 1/8 inch tubing connects with reducing tube fittings that are imbedded in the test section wall. In addition to giving a watertight test section wall, these tube fittings allow the plug and play modification of the span-wise wavelength. Nothing inside the test section wall needs to be changed or modified after the step is installed and the wall should remain watertight. On the inner side of the wall 3/32 inch inner diameter tubing connects with the other port of the embedded tube fittings. The other end of this tubing connects to the actuator slot module.

Various views of the actuator slot module are shown in Figure 3.8. In the exploded view of Figure 3.8a we can see that the flexible 3/32 inch inner diameter tubing connects to a rigid stainless steel tube of the same outer diameter. This rigid tube is bonded into the holes which are drilled at 45° angles into the actuation module as seen in Figure 3.8b. These holes had to be drilled in a staggered pattern to eliminate interference between adjacent flexible 3/32 inch inner diameter flexible tubing when they are connected. Slots 2.5mm in width are milled 1mm deep into the aluminum as seen in Figure 3.8b. The wall thickness between the slots is slightly smaller than 1mm. All 4 walls of the rectangular actuation slots are completed by compressing a very thin adhesive tape between a flat plate and the milled work piece. The sealing plate and a view of all 128 milled slots are shown in the exploded view of Figure 3.8a.

A close-up of the actuator slot module as it will be installed in the completed step assembly is seen in Figure 3.8c. From this figure we can also see how the slots issue out from the vertical section behind the step. This prevents the slots from exhibiting any passive control over the reattachment bubble. In certain wavelengths not all of the 8 tubes of a given manifold are connected to the step. Due to the continuity equation, the excess tubes must also be connected somewhere to maintain consistent velocities in the actuator tubes. A fluid-dynamically similar extra tube reservoir is designed for this purpose as seen in Figure 3.6a. The criteria for a fluid-dynamically similar reservoir design will be discussed in Section 3.4.6.

Signals are sent to the servo motors by the SSC-32 servo controller board from Lynxmotion Inc. The board accepts ASCII text strings from Labview®. These strings are converted by the board's firmware into pulse width modulated signals which it sends to the servos. The analog servos we used sample the pulse width from the servo every 20ms or 50 Hz which is termed the servo refresh rate. At this rate, the servo uses it's feedback circuit to calculate appropriate servo action based on the error between the position desired by SSC-32 signal and the servos own internal potentiometer measurement of its angular position. The details of the feedback algorithm are proprietary information not released by Hitec Inc. To extract performance data from the servos, the potentiometer signal is also sampled by a data acquisition system and the results fed into Labview® for analysis.

A parallel circuit was designed to power the actuators. A diode will be installed into the circuit to prevent damage that could otherwise result from applying reverse polarity to the servos, potentially destroying the internal circuitry of all connected servos. A half rack Kepco JQE 6-22M DC power supply was purchased to power the servos. The servos operate effectively between 4.8 and 6 V, the power supply is capable of giving 0-6V at up to 22 Amp. This should be sufficient to power all the actuators at high loads.

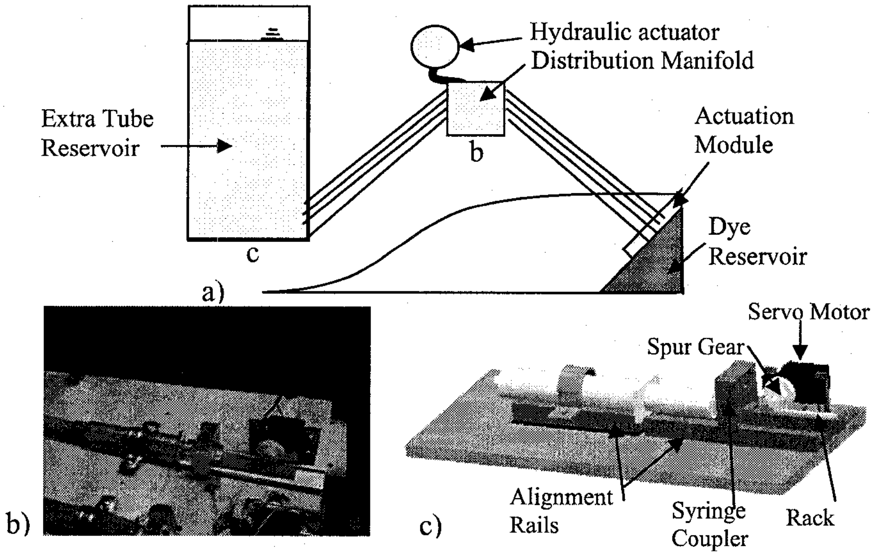

Figure 3.6. Experimental Layout of Actuator Components

a) Overview of experimental layout showing actuation components
b) Photograph of a manufactured rack and pinion actuator
c) Solid model of the designed rack and pinion actuator at the end of a suction stroke

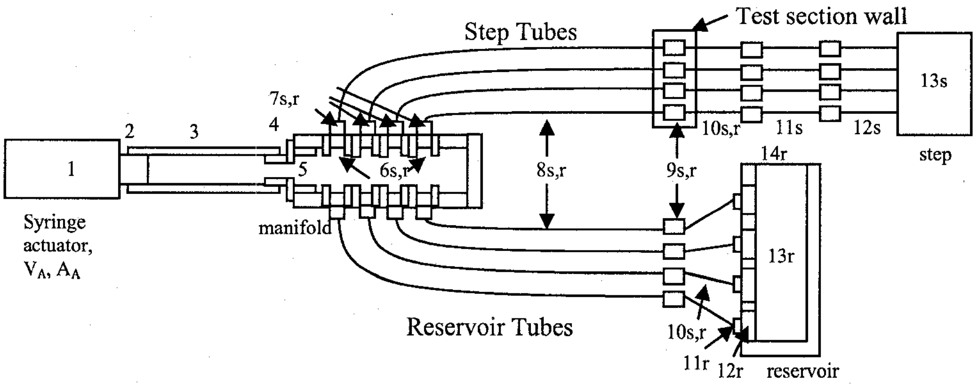

Figure 3.7. Components of the Tubing Networks

Component (j)	Diameter Symbol	Diameter (cm)	Length Symbol	Length (cm)	Tubing Network Description
Both Step and Reservoir Step tubes					
1	D_A	1.96	L_A	3.81	Syringe ID
2	D_2	0.476	L_2	0.635	Luer lock ID
3	D_3	0.952	L_3	243.84	3/8" tubing ID
4	D_4	0.610	L_4	2.794	Barbed fitting ID
5	D_5	0.965	L_5	1.27	Threaded fitting ID
6s,r	D_6	0.635	L_6	1.27	Threaded fitting ID
7s,r	D_7	0.190	L_7	2.794	Barbed fitting ID
8s,r	D_8	0.317	L_8	121.92	1/8" tubing ID
9s,r	D_9	0.165	L_9	0.508	Reducing fitting ID
Step Specific tube					
10s	D_{10}	0.238	$L_{10,s}$	30.48	3/32" tubing ID
11s	$D_{11,s}$	0.213	$L_{11,s}$	2.54	Stainless steel tube
12s	$D_{12,s}$	0.178	$L_{12,s}$	3.81	Actuation Slot
Reservoir Specific tube					
10r	D_{10}	0.238	$L_{10,r}$	32.01	3/32" tubing ID
11r	$D_{11,r}$	0.1524	$L_{11,r}$	3.302	Barbed fitting ID
12r	$D_{12,r}$	0.4318	$L_{12,r}$	1.27	Threaded fitting ID
13r	$D_{13,r}$	30.48	$L_{13,r}$	274.32	Reservoir

Table 3.2. Symbols for components in the Tubing Networks

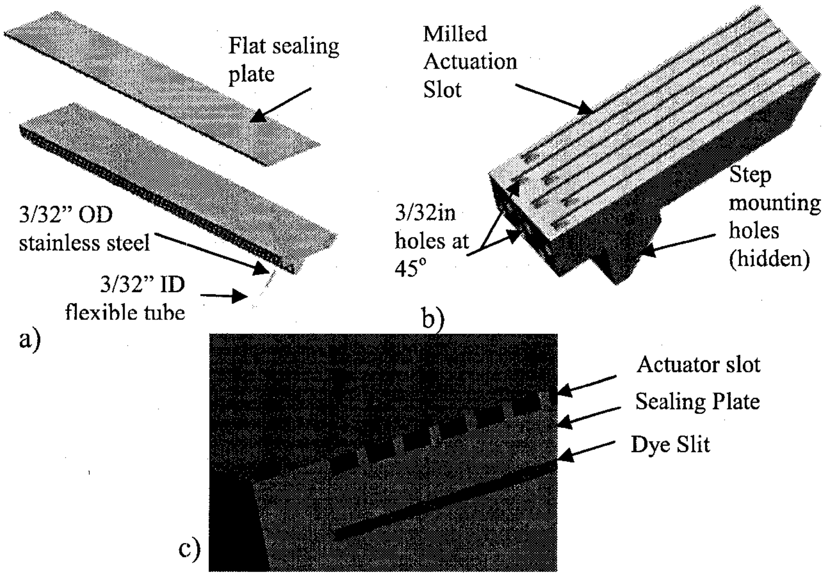

Figure 3.8. Views of Actuator Slot module

a) Exploded Slot Module
b) Segment of Actuator Slot
c) Slot Module Installed

3.4.2. Results from Prototype Actuator

A prototype actuator was built to experimentally test its performance. The servo motor was tested on its ability to track sinusoidal waveforms of the form

$$\theta = \theta_{peak} \sin(\omega t) \qquad [3.6]$$

Here, θ is the angular position of the pinion gear, θ_{peak} and ω are the amplitude and frequency of angular oscillation. Differentiating [3-6] we get the velocity

$$\dot{\theta} = A_v \cos(\omega t) \qquad [3.7]$$

The peak angular velocity is $A_v = \omega\theta_{peak}$. Servo communication and data sampling were done as described in the previous section. Angular position data was sampled from the potentiometer by a data acquisition system. A low pass filter was used to remove the 50Hz pulse width servo communication signal, which highly contaminated the position signal. This signal was then input into the harmonic analysis virtual instrument in Labview® to determine the fundamental oscillation frequency and total harmonic distortion. The peak amplitude θ_{peak} was determined by directly averaging the waveforms.

In Figure 3.9 we can see how the actuator performed in terms of the following criteria:

$$f^* = \frac{f}{f_{desired}} : A_v^* = \frac{A_v}{A_{vdesired}}.$$

In Figure 3.9a, we plot the normalized actuation frequency (f^*) versus the desired frequency. It is seen that the actuator gives the desired actuation frequency within 10% at all frequencies. Below 3.5Hz the actuator gives actuation at the desired frequency with minimal error. Hence frequency limitations do not seem to be a large.

In Figure 3.9b we have given a plot of the normalized actuation peak velocity (A_v^*) versus the desired frequency. For frequencies less than 2.5Hz the mean actuation peak compares well with the desired value with minimal error. The max and min peaks of the measured actuation are within 8% of the desired value. For the rest of the spectrum, the average actuation peak value decreases steadily to have an error of 20% at 6 Hz. Also, at 6 Hz, the fluctuation of the maximum and minimum peak values increase to have 16% error relative to the measured mean value.

In Figure 3.9c we plot the THD versus the desired actuation frequency for A_V=250deg/s. At 0.5 Hz the THD is a low 5%, raising in an almost linear fashion to 25% at 4.5 Hz. Between 4.5 and 6 Hz the distortion is much higher at values between 35 and 40%. Hence, total harmonic distortion limits our actuation to around 3Hz if we want to limit distortion effects. However, harmonic distortions have been shown to be beneficial (Kim et al, 2007) and the large distortions at the higher frequencies could actually be beneficial.

From this testing we can adequately say that an upper bound for good actuation would be no more than 3Hz. We found that excellent actuation performance occurs below 1.5Hz. We expect that multiple frequency forcing will be of good frequency content in this range. Unfortunately, the data on multiple frequencies forcing by Kim et al (2007) was not available prior to prototype testing.

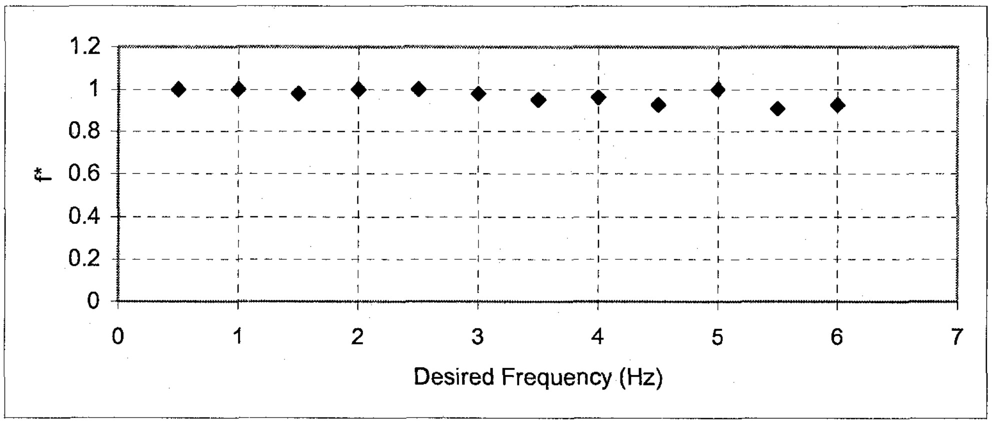

a) Normalized Frequency tracking

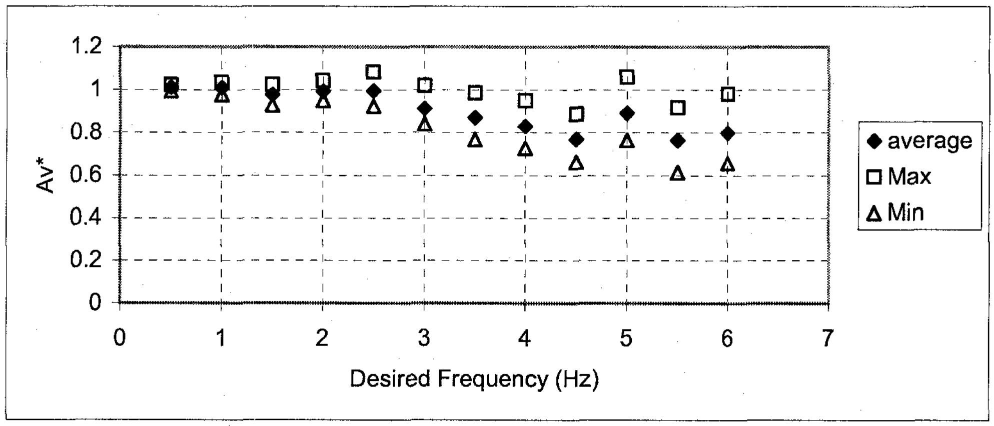

b) Normalized Peak Actuation Velocities

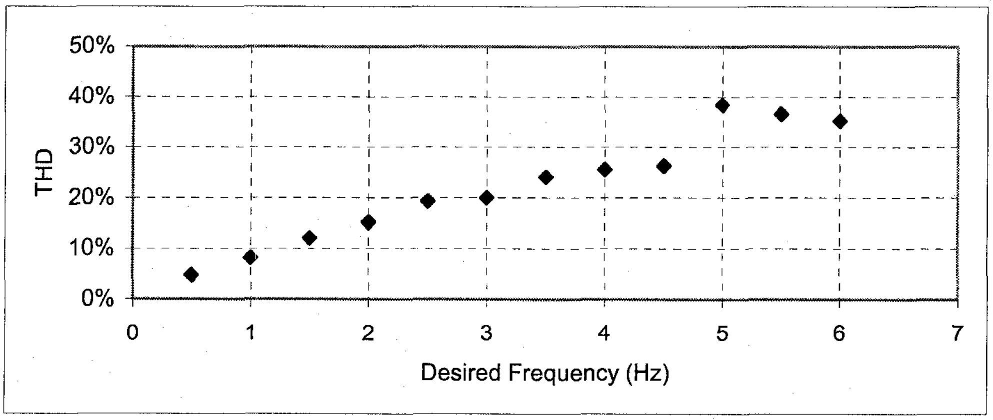

c) Total Harmonic Distortion

Figure 3.9. Prototype Actuator Performance

3.4.3. Actuation Frequency and Reynolds Number

The use of water as the working fluid is not arbitrary. Using water we can get a much lower tunnel velocity for a given Reynolds Number, based on step height. This term is defined as:

$$\mathrm{Re}_h = \frac{U_\infty h}{\upsilon} \qquad [3\text{-}8]$$

Setting the ratio of Reynolds numbers to be unity we get a relationship for water velocity in terms of air velocity at a temperature of 20°C.

$$\frac{\mathrm{Re}_{h,water}}{\mathrm{Re}_{h,air}} = \frac{U_{water} h}{\upsilon_{water}} \frac{\upsilon_{air}}{U_{air} h} = 1$$

$$U_{water} = \frac{\upsilon_{water}}{\upsilon_{air}} U_{air} \approx \frac{1}{14.8} U_{air} \qquad [3\text{-}9]$$

Relationships for the optimum frequencies can be determined from the Strouhal numbers based on step height (h) and momentum thickness (θ) as given by:

$$f_h = \frac{St_h U_\infty}{h} \text{ and } f_\theta = \frac{St_\theta U_\infty}{h} \qquad [3\text{-}10]$$

The Strouhal numbers, St_h and St_θ, have optimum values of 0.2 and 0.012 for step mode and shear layer mode respectively. It can be seen from [3-10] that lower tunnel velocities and higher step heights result in lower optimal forcing frequencies. Maximum obtainable Reynolds numbers, based on the absolute maximum (< 6.25 Hz) and the low total harmonic distortion actuation range (< 3 Hz) are tabulated in Table 3.3. Hence the step mode instability can be forced up to a Re_h of 46,100 and the shear layer instability can be forced up to Re_h of 16,750.

Frequency Range (Hz)	Re_h Range (max U_∞ cm/s)	
	Based on f_θ	Based on f_h
0-6	0-33,000 (0.6)	0-92,200 (1.7)
0-3	0-16,750 (0.3)	0-46,100 (0.83)

Table 3.3. Reynolds numbers and frequency ranges of actuation

3.4.4. Actuation Amplitudes

For multiple frequency oscillations, which have their own different prescribed amplitudes and phase relationships, there will be various modulations to the amplitude. In term of the single frequency actuation case, which will make up a large portion of the experimental results, the temporal part of the forcing is:

$$V_A(t) = V_{A,peak}\cos(2\pi ft) \qquad [3\text{-}11]$$

The peak angular velocity is $A_v = \omega\theta_{\max}$. Using the tangential velocity relation $V_{A,peak} = rA_v$ of the rack and pinion system, the temporal portion of the forcing can be written as:

$$V_A(t) = rA_v\cos(2\pi ft) \qquad [3\text{-}12]$$

The servo, using a spur gear with a radius (r) of 1.27 cm (0.5 in), is limited to a peak angular velocity $A_v = 1.39\pi$ rad/s (250 deg/s). This was determined in the testing of the prototype as a conservative upper bound to prevent overworking when forcing the fluid system. This corresponds to a velocity in the syringe of 5.54 cm/s and an ideal slot exit velocity of $V_{12,s} = 83.5\text{cm/s}$ out of each of the 8 tubes.

We use the RMS value of our span-wise variations to compare with the existing uniform actuation amplitudes. If we assume a sinusoidal span-wise distribution of velocity, then the RMS value of actuation is:

$$V_{12,s,RMS} = V_{12,s}/\sqrt{2} = 59cm/s.$$

To keep step mode actuation frequencies below 3 Hz, tunnel speeds will range between 13 cm/s and 83 cm/s for Reynold's numbers (Re_h) of between 7000 and 46,100. These velocities correspond to $V_{12,s,RMS}/U_\infty$ range of 453% to 71%, where typical values from studies are 2% to 30%. We can reproduce these values simply by changing the A_v value, by modifying the experimental parameters r, θ_{peak} and ω.

3.4.5. Span-wise Wavelengths of Actuation

Since the span-wise variation has the greatest potential to contribute to the literature, it is the most important aspect of the design. There is no particular reason why the periodic span-wise distribution of actuation must be sinusoidal. It can be any arbitrary distribution, as long as it can be adequately resolved using 8 or 16 different actuation velocities and has the designed wavelengths. As we saw earlier in Figure 3.3, the continuous span-wise distribution of velocity is approximated by a discrete distribution. The shortest wavelength case is $L_{z,o}$ of 0.5h, which has a maximum resolution (R_{wave}) of 8 velocity types per wavelength. A plot of the actuation profile versus the z/L_a is given in Figure 3.10a. L_a is the full span-wise width of the actuation slot module. From the figure we see 16 identical wavelengths resolved by 8 different velocity types per wavelength. Figure 3.10b shows only one wavelength of this actuation where the span-wise co-ordinate z is normalized by the width of a discrete actuation slot (W_a). This width includes both the open slot width and the width of the wall and is approximately 3.5mm. It is clearly seen in the figure that each discrete velocity in the L_z of 0.5h wavelength is created by only 1 actuator slot. This actuation wavelength is the fundamental wavelength of all the possible wavelengths with a resolution of 8 velocity types. To use the frequency analogy, L_z of 1h, 1.5h, 2h ... are "harmonic" wavelengths or integer multiples n of 2, 3, 4 of the fundamental wavelength $L_{z,o}$. The term n, denoted the wave number, also describes the number of adjacent actuation slots that must have the same velocity. Plots of various span-wise wavelengths versus z/W_a are given in Figure 3.11.

Since the continuous velocity signal is approximated by discrete velocities of varying width, we try to improve the accuracy by calculating the discrete velocity based on the midpoint equation. Each velocity level i, is calculated as:

$$V_A(z) = \sin\left(\frac{2\pi}{L_z}\left[\frac{z_i + z_{i+1}}{2} + z_p(t)\right]\right) \quad \text{For i=1, 2, 3...8} \qquad [3\text{-}13]$$

Where $z = W_a \times \begin{bmatrix} 0 & n & 2n & 3n & 4n & 5n & 6n & 7n & 8n \end{bmatrix}$

Therefore, the resolution of a given wavelength is 8 but the physical widths of the regions of equal velocity depend on the wave number (n) of the wavelength being used.

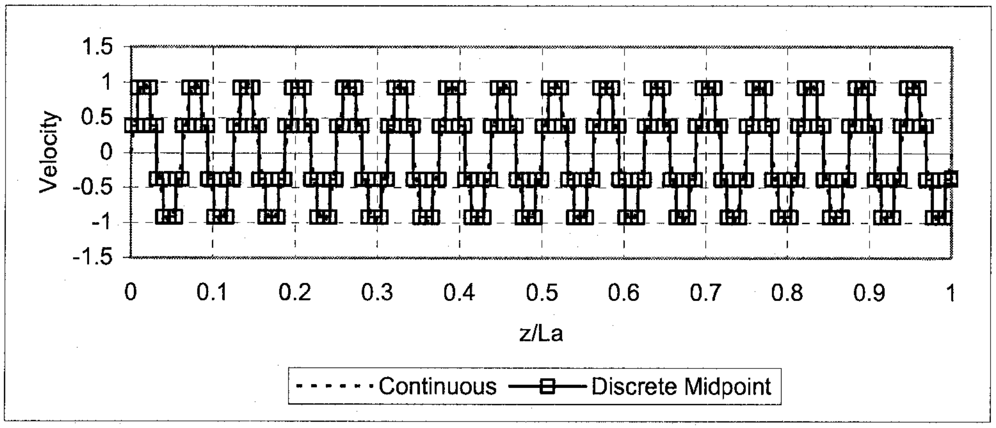

a) All 16 wavelengths of actuation normalized by the width of the actuator module L_a

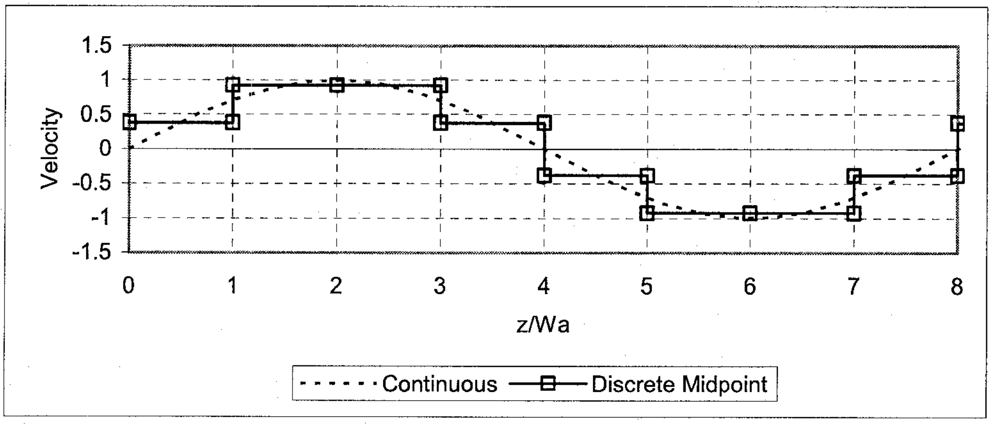

b) One wavelength with the span-wise co-ordinate normalized by actuator slot width W_a

Figure 3.10. L_z=0.5h, the fundamental wavelength

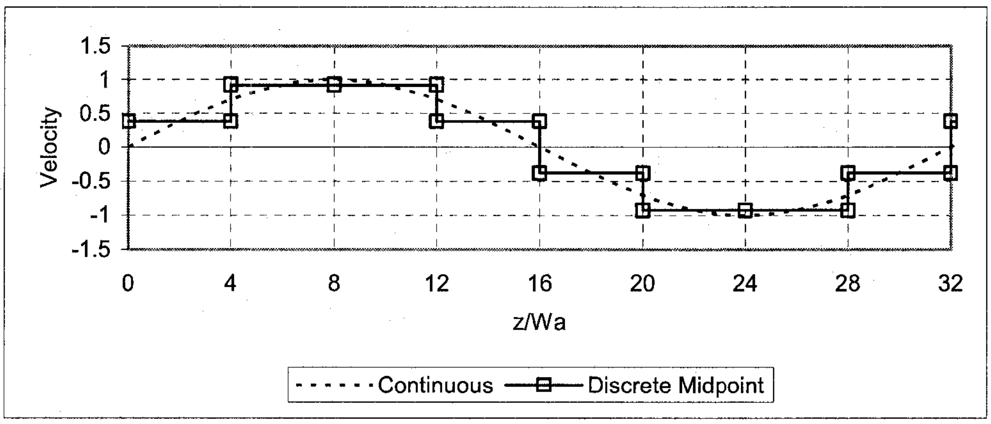

a) L_z=2h showing n=4 adjacent tubes of equal velocity

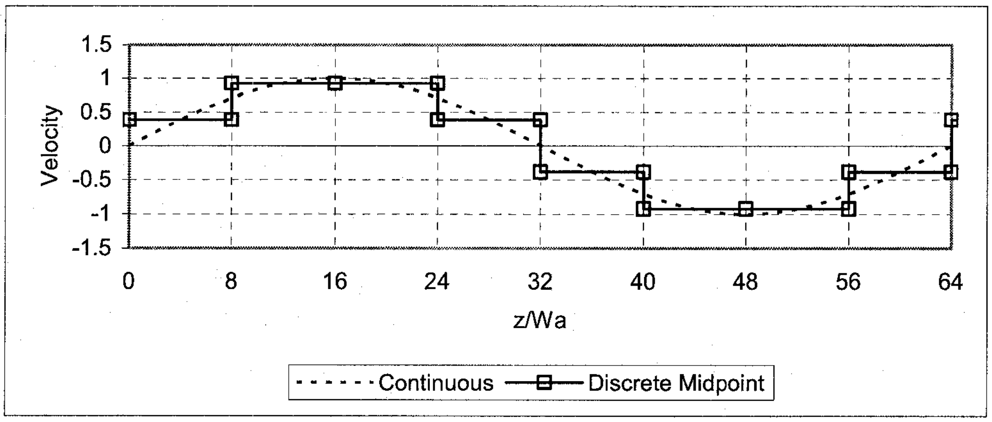

b) L_z=4h showing n=8 adjacent tubes of equal velocity

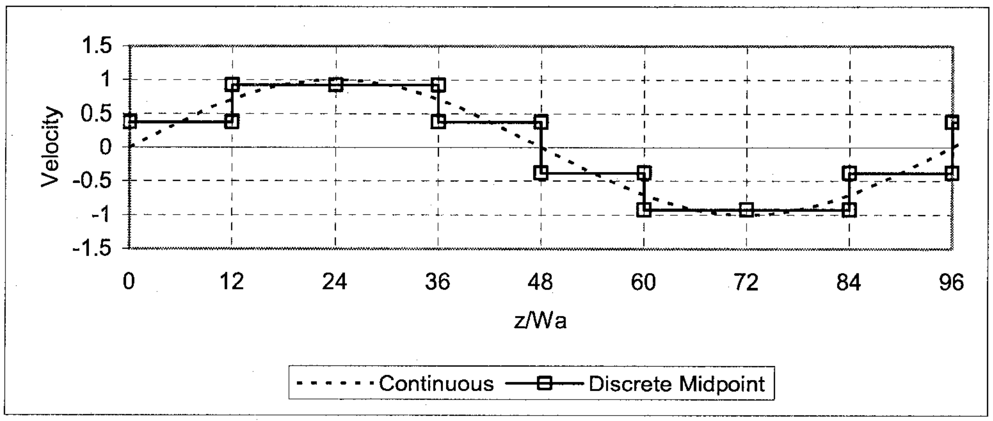

c) L_z=6h showing n=12 adjacent tubes of equal velocity
Figure 3.11. Harmonic Wavelengths

In addition to the span-wise distribution the time varying phase of the distribution was found to be very necessary in optimal open-loop forcing of the backward-facing step (Kang and Choi, 2002). As with the wavelength, this time varying phase is also discretized by the slot width W_a. The time varying phase term is calculated as:

$$z_p(t) = c_{zp}(t)W_a \qquad [3\text{-}14]$$

$C_{zp}(t)$ is the number of slots which are offset by the phase $z_p(t)$. The resolution of the phase (R_{z_p}) in terms of degrees, is calculated as

$$R_{z_p} = 360\frac{W_a}{L_z} \qquad [3\text{-}15]$$

In Figure 3.12 we have plotted the span-wise resolution versus the wavelength. The phase resolutions are much larger for the shorter wavelengths as a direct consequence of the relative size of W_a to L_z. Therefore, modifications of time varying phase will probably be more effective for wavelengths greater than 2h.

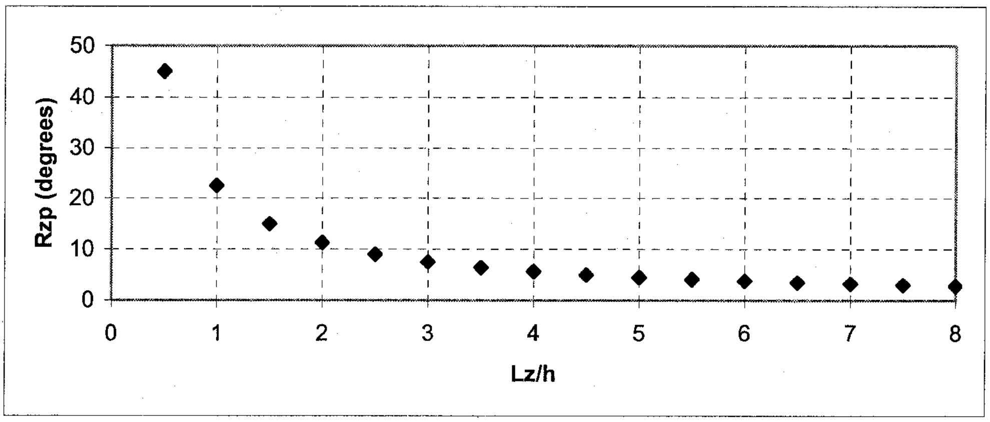

Figure 3.12. Resolution of Span-wise Phase

Earlier we made a reference to an extra tube reservoir that was required for certain wavelengths. Consider any wavelength L_Z divided into the entire span-wise actuation width which has a design value of L_a=8h. If L_a/L_Z is an integer (b) then no reservoir is required, but if b is not an integer, then a reservoir is required. We tabulate the values of b as they depend on the span-wise wavelength coefficient (a; $L_z = ah$) in Table 3.4. The reason for this can be found with reference to Figure 3.13. In figure a, we plot L_Z of 4h with L_a/L_z=2. From this figure we can see that the groupings of discrete actuation slots, or velocity regions, have been numbered from 1 to 8. We see that each region requires the full 8 slots, and there are 2 regions of each type. This requires exactly 16 tubes of each velocity to create the actuation profile. Since the manifolds split the actuation from 1 syringe into 8 tubes, the 16 required tubes is an integer multiple of this. The required tubes for the actuation and the available tubes from the servo motors for all instances where b is an integer are tabulated in Table 3.5a.

With reference to Figure 3.13b we have a case where L_z=4.5h. The value of L_a/L_z=1.78 is not an integer, and a reservoir must be used. For these types of wavelengths, the number of tubes required per actuation region is not generally equal to an integer multiple of 8. Hence, extra tubes will occur. The number of extra tubes for the L_a/L_Z wavelength is calculated and tabulated in Table 3.5b.

To mathematically show the importance of using the reservoir, consider the continuity equation as applied through the manifold.

$$V_{outlet} = V_{inlet} \frac{A_{inlet}}{A_{outlet} N_{outlet}} \qquad [3\text{-}16]$$

If we simply block manifold outlets we reduce the number of connected outlets (N_{outlet}) where other unblocked manifolds will have N_{outlet}=8. This will have drastic effects on the velocity of the unblocked outlets. Hence we need to have all the extra tubes connected to a reservoir by a tubing system that is fluid-dynamically similar to the systems connecting the manifolds to the actuation module in the step.

Up to this point we have been discussing actuations with only 8 different velocities per wavelength in span-wise actuation profile. Although it was not a designed feature of the actuation, we can increase the resolution from 8 to 16 simply by taking the L_z=1h as the fundamental wavelength for 16-resolution tests. In this case the possible wavelengths would be 1h,2h,3h,...8h with wave numbers n_{16}=1,2,3...8. We saw how such an increase in resolution is beneficial to the L_z=8h case earlier in Figure 3.3 of Section 3.2.2. From equation [3-15] the increase in wavelength resolution would not influence the resolution of the time varying span-wise phase.

Since the actuator was designed with a wavelength resolution of 8 using only 22 different servo motors and rack and pinion, some resolution 16 wavelengths will not be possible without a small upgrade. Doing a similar analysis as was done for the extra tube reservoir calculations, Table 3.6 shows that only wavelengths 3h, 5h and 7h are not possible without upgrading the actuator to have 4 more rack and pinion actuators. Such an expense would not be very substantial and it may be desirable depending on the results of the wavelength resolution 8 actuator trials.

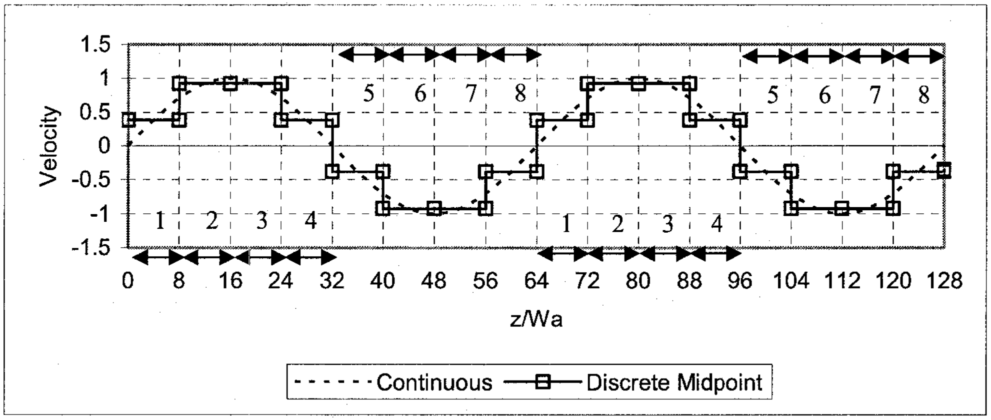

a) L_z=1h L_z/L_a=2, integer divisor reservoir not required

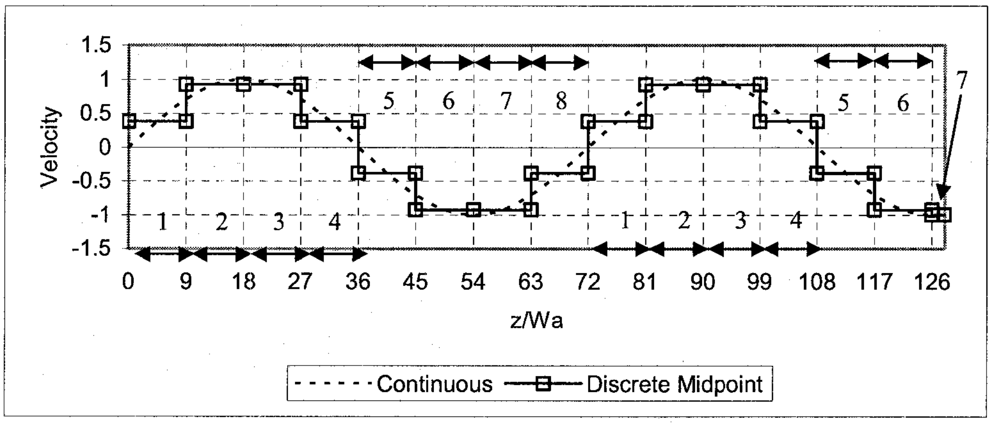

b) L_z=4.5 L_a/L_z=1.78, non-integer divisor reservoir is required

Figure 3.13. Comparison of integer and non-integer divisor span-wise wavelengths

a[1]	b[2]	Reservoir
0.5	16	No
1	8	No
1.5	5.33	Yes
2	4	No
2.5	3.2	Yes
3	2.67	Yes
3.5	2.29	Yes
4	2	No

a[1]	b[2]	Reservoir
4.5	1.78	Yes
5	1.6	Yes
5.5	1.45	Yes
6	1.33	Yes
6.5	1.23	Yes
7	1.14	Yes
7.5	1.07	Yes
8	1	No

Table 3.4. Tabulated values wavelength terms a and b

[1] Lz=ah
[2] $b=L_a/L_z$

Velocity Region	Tubes				Extra Tubes per Servo
	Required	Available	extra	# servo	
1	16	16	0	2	0
2	16	16	0	2	0
3	16	16	0	2	0
4	16	16	0	2	0
5	16	16	0	2	0
6	16	16	0	2	0
7	16	16	0	2	0
8	16	16	0	2	0
Column sum	128	128	0	16	---

a) table of tubing requirements for all integer divisor wavelengths L_z=0.5h,1h,2h,4h,8h.

Velocity Region	Tubes				Extra Tubes per Servo
	Required	Available	extra	# servo	
1	18	24	6	3	2
2	18	24	6	3	2
3	18	24	6	3	2
4	18	24	6	3	2
5	18	24	6	3	2
6	18	24	6	3	2
7	11	16	5	2	2.5
8	9	16	7	2	3.5
Column sum	128	176	48	22	---

b) table of tubing requirements for the non-integer divisor wavelength L_z=4.5h

Table 3.5: Tubing Requirements for integer and non-integer divisor wavelengths

wavelength	# servo	wasted tubes	<= 22 servos
1h	16	0	Yes
2h	16	0	Yes
3h	26	80	No
4h	16	0	Yes
5h	25	72	No
6h	21	40	Yes
7h	19	24	No
8h	16	0	Yes
	Experiments possible with 5 of 8 wavelengths		

Table 3.6. Possible Resolution of 16 experiments with the Resolution 8 design

3.4.6. Condensed Derivation of Fluid Dynamic Similarity

In this section we use an unsteady Bernoulli equation model that is derived fully in Appendix B. This model allows us to quantify fluid-dynamic similarity conditions for the design of the step and extra tube reservoir branches.

Since the equation is based on the unsteady Bernoulli equation, flow must be assumed inviscid or along a stream-line. Water itself is essentially incompressible; however the amount of trapped air in the actuation networks must be minimized to retain incompressibility. All other assumptions in the calculation are discussed in great detail in Appendix B.

We write the unsteady Bernoulli equation for the one of the step tubes along a stream-line through the actuator (A) and a point (t_n) as described in Figure 3.14. In doing this we get

$$P_A(t)+\frac{\rho V_A^2(t)}{2}+\rho g y_A=P_{tn}+\frac{\rho V_{tn}^2}{2}+\rho g y_{tn}+\rho\int_A^{tn}\frac{\partial V}{\partial t}ds \qquad [3\text{-}17]$$

At this point the unknowns are the actuation pressure $P_A(t)$ and the branch flow fractions c_s and c_r for step and reservoir tubes. These branch flow fractions are contained within the integral term. In Appendix B we show how conditions in the bulk tunnel flow reduce [3-17] to:

$$P_A(t)+\frac{\rho V_A^2(t)}{2}=\rho\int_A^{tn}\frac{\partial V}{\partial t}ds \qquad [3\text{-}18]$$

Similarly, the unsteady Bernoulli equation along a stream-line between the actuator (A) and the free surface of the reservoir is

$$P_A(t)+\frac{\rho V_A^2(t)}{2}+\rho g y_A=\rho g y_r+\rho\int_A^{r}\frac{\partial V}{\partial t}ds \qquad [3\text{-}19]$$

Also in Appendix B we show that an ideal, experimentally set value of $y_A = y_r$ is desirable. Note, this co-ordinate is the distance from the free surface as seen in Figure 3.14, and is not to be confused with the y step co-ordinate as shown in Figure 3.1. Therefore, [3-19] simplifies to:

$$P_A(t) + \frac{\rho V_A^2(t)}{2} = \rho \int_A^r \frac{\partial V}{\partial t} ds \qquad [3\text{-}20]$$

Subtracting [3-20] and [3-19] we eliminate the unknown $P_A(t)$ and get:

$$0 = \rho \int_A^{tn} \frac{\partial V}{\partial t} ds - \rho \int_A^r \frac{\partial V}{\partial t} ds \qquad [3\text{-}21]$$

These integral terms are expanded in Appendix B and [3-21] simplifies to:

$$0 = \left[\sum_6^{12} \frac{A_A}{A_j} L_j c_s + \frac{A_A}{A_{13}} L_{13} \right] - \left[\sum_6^{12} \frac{A_A}{A_j} L_j c_r + \sum_{13}^{14} \frac{A_A}{A_j} L_j \right] \qquad [3\text{-}22]$$

The continuity equation provides another equation for us to solve for c_s and c_r. In doing so we get:

$$c_r = \frac{\sum_6^{12} \frac{A_A}{A_{j,s}} L_{j,s} - N_s \sum_{13}^{14} \frac{A_A}{A_{j,r}} L_{j,r}}{N_s \sum_6^{12} \frac{A_A}{A_{j,r}} L_j + N_r \sum_6^{12} \frac{A_A}{A_{j,s}} L_{j,s}} \qquad [3\text{-}23]$$

$$c_s = \frac{\sum_6^{12} \frac{A_A}{A_{j,r}} L_{j,r} + N_r \sum_{13}^{14} \frac{A_A}{A_{j,r}} L_{j,r}}{N_s \sum_6^{12} \frac{A_A}{A_{j,r}} L_{j,r} + N_r \sum_6^{12} \frac{A_A}{A_{j,s}} L_{j,s}} \qquad [3\text{-}24]$$

All additional symbols in these equations were tabulated and described in Table 3.2. To force c_s to be very close to the ideal value of 1/8 we must ensure the following fluid-dynamic similarity conditions occur.

$$\sum_{13}^{14} \frac{A_A}{A_{j,r}} L_{j,r} \approx 0 \qquad [3\text{-}25]$$

$$\sum_6^{12} \frac{A_A}{A_{j,r}} L_{j,r} = \sum_6^{12} \frac{A_A}{A_{j,s}} L_{j,s} \qquad [3\text{-}26]$$

To satisfy the condition in [3-25] we simply select the area of the reservoir A_j to be very large relative compared with the area of the syringe piston A_A. To satisfy the condition in [3-26] we can cut the 3/32 inch reservoir tubes a slightly different length than the step tubes. An equation for the required length of reservoir 3/32 inch tubing can be derived from the condition as:

$$L_{10,r} = \frac{A_{10,r}}{A_A}\left(\sum_{j=6,s}^{12,s}\frac{A_A}{A_j}L_j - \sum_{j=6,r;j\neq 10,r}^{12,r}\frac{A_A}{A_j}L_j\right)$$

From Table 3.2 we can see that the reservoir 3/32 inch tubing is almost 1.5cm longer than the step tubing. Using this tubing length the error in the fluid dynamic similarity is very small:

$$\frac{c_s - 0.125}{0.125}100 = \frac{0.125007 - 0.125}{0.125}100 = 0.0056\%$$

The error results from the fact that condition of [3-25] cannot be exactly equal to 0.

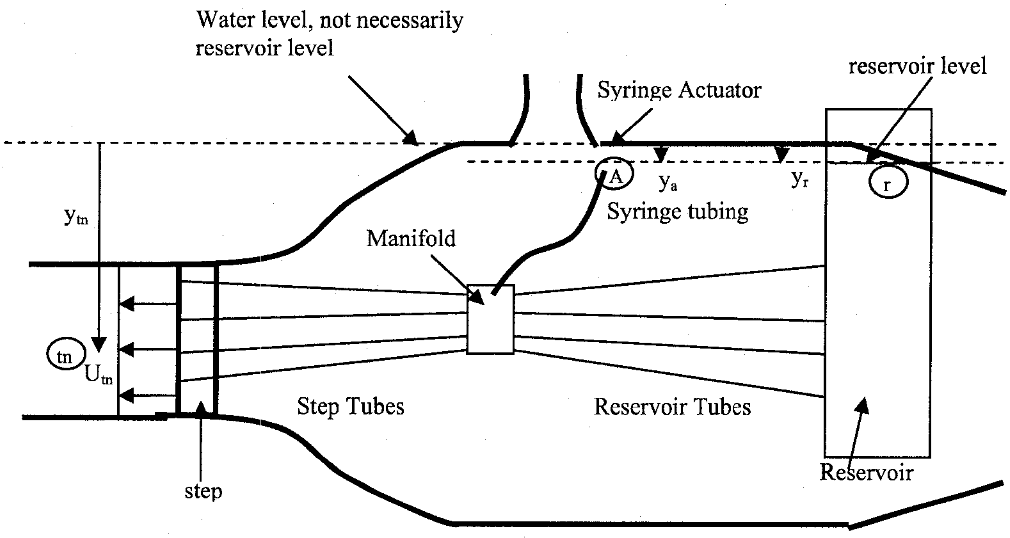

Figure 3.14. Schematic of the Tubing network for 1 actuator

3.5. Step Design

The Step portion of the apparatus is designed to be modular. As shown in Figure 3.15, it is comprised of the main step portion, actuator slots and dye reservoir. The dye reservoir portion also seals the module, with the exception of the actuation tubing clearance slot in its base. The entire module was anodized black to prevent corrosion, harden the thin and extremely sharp leading edge and to minimize reflected light from its surface when doing flow visualization. The actuator module is removable and can be applied to other flow. Hence, in the future we could apply this type of actuation to other flow geometries (forward facing step, planar jets, wing sections etc.). In this chapter we will discuss the design details of the step profile in section 3.5.1 and dye reservoir modules section 3.5.2.

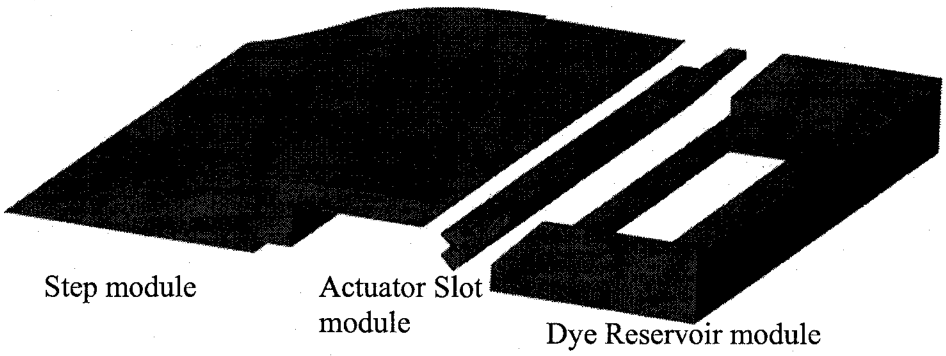

Figure 3.15: Exploded View of the Backward-facing Step

3.5.1. Design of the Step Module

The step module as seen in Figure 3.15 is one solid piece of anodized aluminum. It mounts directly to the test section wall. The design problem here was to quantify the step profile so that separation would not occur. The step profile includes 3 portions as laid out in Figure 3.16. These include a fillet which removes the possibility of separation from the leading edge of the ellipse section as a result of the test section wall. At no point along this profile does the slope of the profile exceed the slope of the tunnel contraction located just upstream of the test section. So flow separation is not expected to be an issue. The fillet and ellipse sections are followed by a horizontal section which is 2h in length. To some extent, this section isolates the influence of the fluid acceleration over the fillet and ellipse from the separation point.

The fillet is designed using a collocation-polynomial curve fit using 5 conditions. The five term, 4th order polynomial fillet is given by:

$$f(x) = a_0x^4 + a_1x^3 + a_2x^2 + a_3x + a_4 \qquad [3\text{-}27]$$

The coefficients a_4 to a_0 are determined by solving a system of linear equations in the form:

$$\begin{bmatrix} x_1^4 & x_1^3 & x_1^2 & x_1 & 1 \\ 4x_1^3 & 3x_1^2 & 2x_1 & 1 & 0 \\ 12x_2^2 & 6x_2 & 2 & 0 & 0 \\ 4x_3^3 & 3x_3^2 & 2x_3 & 1 & 0 \\ x_3^4 & x_3^3 & x_3^2 & x_3 & 1 \end{bmatrix} \begin{bmatrix} a_0 \\ a_1 \\ a_2 \\ a_3 \\ a_4 \end{bmatrix} = \begin{bmatrix} f(x_1) \\ f'(x_1) \\ f''(x_2) \\ f'(x_3) \\ f(x_3) \end{bmatrix} \qquad [3\text{-}28]$$

Position and derivative boundary conditions were prescribed for the ends of the fillet x_1 and x_3 respectively. To smooth the curve, an inflection point was prescribed at the midpoint (x_2) of the fillet. The values used to calculate the polynomial spline coefficients are:

$[x_1\ x_2\ x_3]$=[0 8.77 8.77/2] cm and

$[f(x_1)\ f(x_2)\ f(x_3)]$=[0 1.41 3.28] cm.

The conditions for solving the polynomial curve fit are:

$[f(x_1)\ f'(x_1)\ f''(x_2)\ f'(x_3)\ f(x_3)]$=[3.28 0.532/2 0 0.532 0].

The solution vector to the matrix system is:

$[a_o\ a_1\ a_2\ a_3\ a_4]^T=[0.394\ -6.26\ 36.9\ 266\ 0]^T\ 10^{-3}$.

The slope of the ellipse at $x_3=8.77$ cm is 0.532, so the fillet and the ellipse join smoothly. The slope at the leading edge was assumed to be half of this value.

The ellipse is designed to be a 3:1 ratio between major and minor diameter, where the minor diameter is aligned parallel with the bulk flow direction. The flow over such an ellipse has been shown not to separate without a smoothing fillet (Sigurdson, 2005). The minor diameter of the ellipse (b) is the step height h. The major diameter (a), due to the 3:1 relationship, is 3h. The profile is calculated using the equation:

$$y=\sqrt{\left(1-\left[\frac{(x-x_c)}{a}\right]^2\right)b^2}+y_c \qquad [3\text{-}29]$$

The values of x, for the ellipse section, range between x_3 of the fillet to $x_4=x_c=h+a$, the start of the horizontal section. The x_4 term has a value of 4h (22.16 cm), where the start of the unused section of ellipse starts at x=h. The center of the ellipse is at (x_c, y_c) The ellipse then joins smoothly with the horizontal section at x_4.

The horizontal section is 2h in length, plus the added thickness of the actuator module width (approx 0.230h). The underside of this horizontal section is milled out to give clearance for the actuation tubing as seen in Figure 3.15. The reservoir module fastens this region to provide an enclosed cavity, which is ideally watertight stopping leaks from the bulk flow.

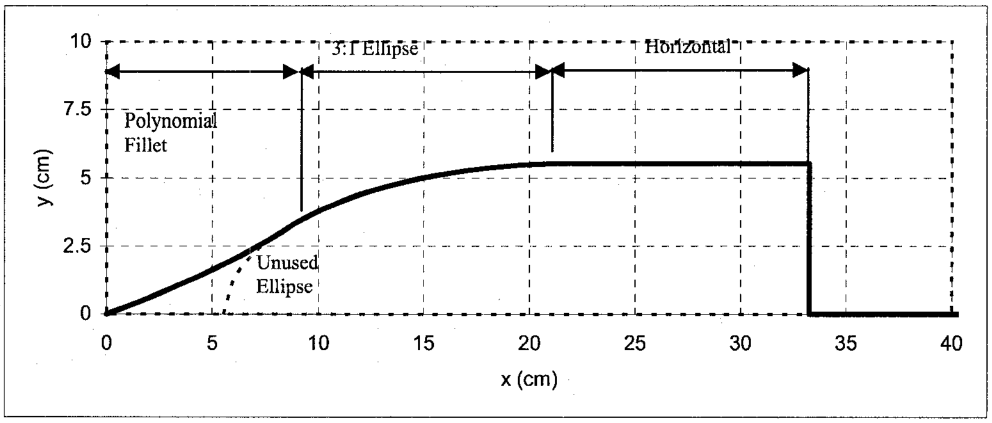

Figure 3.16. Step Spline Design Components

3.5.2. Dye Reservoir Module and Modifications for Flow Visualization

An exploded view of the dye reservoir module is seen in Figure 3.18a. The large rectangular slot in the base plate gives clearance for the actuation tubes. All 5 plates of this module are used to enclose the in step dye reservoir. Dye is supplied via 3 dye entrance ports as labeled in Figure 3.18, where the flow of dye is controlled by a gate valve as shown in Figure 3.2a. Dye is allowed to slowly leak into the flow through a very small gap between the dye plates #1 and #2. This gap, and its nominal dimensions are shown in Figure 3.18b. Since the dye leaks out 6 mm below the separation point, the dye will be drawn up into the recirculation bubble to directly track the vorticity.

Clearance for our hydrogen bubble wire was drilled through both the step module and the reservoir base plate 1.3 step heights (h) upstream of separation. In addition to pitot tube traverses, we can quantify the momentum thickness of the boundary layer using the bubbles and image correlation velocimetry (ICV) as developed by Apps, (2001) and Apps, Chen and Sigurdson, (2003). Therefore, we can accurately calculate St_θ.

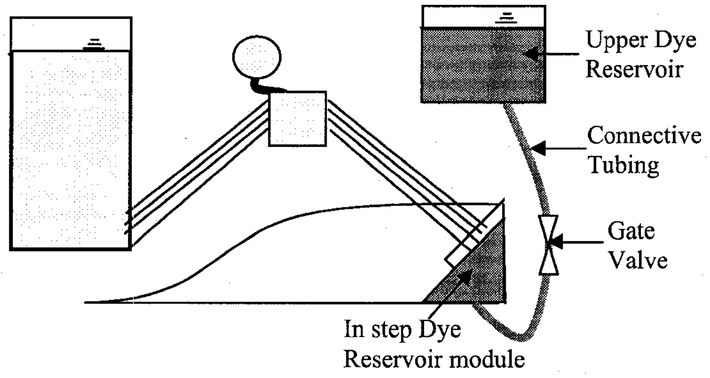

Figure 3. 17. Layout of Dye Reservoir Components

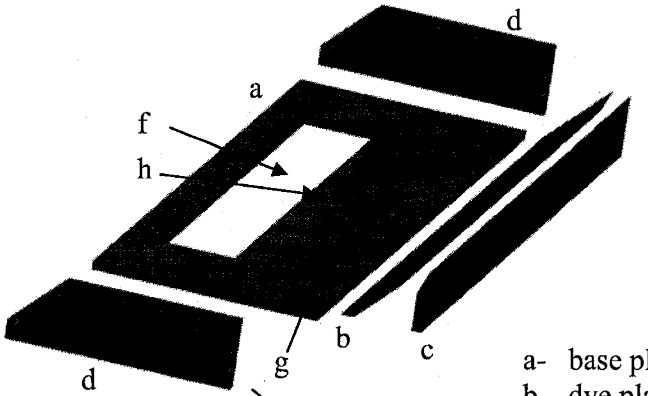

a) Exploded View

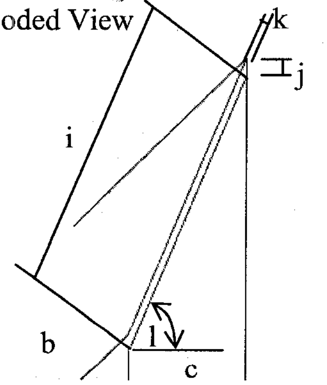

b) Close-up of Dye Slit

a- base plate
b- dye plate #1
c- dye plate #2
d- Side Plates
e- Dye Slit
f- Tube Exit
g- Dye ports
h- H_2 wire hole
i- 1.7 cm
j- 1 mm
k- 0.4 mm
l- 67.5°

Figure 3.18. Views of the In Step Dye Reservoir Module

Conclusions

The major motivators of our research were the success of using span-wise variations in the numerical experiments of Kang and Choi (2002) and the experimental use of a similar linkage-based actuator to force a planar jet by Sakakibara and Anzai (2001).

We have designed a backward-facing step control device that can immediately contribute to the existing literature regarding active control of a reattaching shear layer behind a backward-facing step. After considering many different actuator technologies and designs we selected a blowing and suction type actuator using 22 servo motors. Each motor is connected to rack and pinion force transmission systems. The rack is connected to the plunger of a syringe which pumps fluid in an out of the syringe at the prescribed tangential velocity of the pinion gear; therefore, the inherent non-linearity of linkages is removed and only the non-linearities of the servo motor feedback response exist. At higher actuation frequencies, compensation for these non-linearities would be more difficult for our servo motors. Each of the 22 syringes is connected to a distribution manifold which supplies fluid to the actuation slots.

The actuator is quite easy to use as its motion is prescribed by pulse width signals that can be controlled by Labview® or other related software. Since the actuator is connected to the flow geometry by an easily modifiable tubing network, actuator updates are easy to fabricate and the actuators can force a wide variety of other flow geometries.

The major design feature of this actuator is span-wise variation of the actuation magnitude. These variations can be any periodic waveform, provided the waveform can be adequately resolved by the 8 or 16 different magnitudes of actuation. Each of these magnitudes is created by a different servo motor actuator. Optimal wavelengths for forcing have dimensionless values that are scaled by the step height. This was found by Kang and Choi (2002) in their numerical simulations as they obtained an optimal span-wise wavelength (L_z) of 4 step heights (h). Our actuator will be the first to reproduce their result experimentally, as we will be able to test L_z/h of 0.5, 1, 1.5, 7.5 and 8 when each wavelength is resolved with 8 actuation magnitudes. For wavelengths resolved by 16 actuation magnitudes we will be able to test L_z/h of 1, 2, 4, 6, 8. Wavelengths of 3h, 5h and 7h can be tested with a small system upgrade. Kang and Choi (2002) found the time varying phase relationship was found to be beneficial in the forcing. With our discretized method of realizing their span-wise distributions we can get resolutions of this phase that correspond to 10% of the wavelength at $L_z/h=2$. Therefore, we expect that our realizations of this feature will be good for wavelengths of L_z/h of 2 to 8. Up to this point, no researchers have implemented such span-wise variations experimentally on a backward-facing step.

The actuator has a maximum Re_h value of 16,750 for forcing at the shear layer mode of instability and a maximum Re_h of 46,100 for forcing at the step mode of instability. These Reynolds numbers correspond to an actuation frequency of 3Hz. Although it was not tested, the actuator is anticipated to also yield publishable results using span-wise variations and newly found advantages of multiple frequency forcing (Kim et al, 2007) for Re_h less than about 9,000. This number corresponds to a forcing frequency of 1.5 Hz where exceptionally good single frequency forcing was found using the prototype. The minimum Re_h of our experiments is approximately 2,000 as this is where reattachment lengths become independent of Re_h for our expansion ratio (Adams and Johnston 1998b).

In addition to designing the actuator module in Sections 3.3 and Sections 3.4, we also designed the backward-facing step module in Section 3.5. Here we carefully designed the step profile so that it would join with the test section wall. The step profile was carefully designed such that it avoided the occurrence of premature flow separation along its surface. We also designed 2 imbedded visualization systems into the step. The most simple of these systems is the hydrogen bubble wire which will be used to determine the highly important inflow boundary layer quantities. The second is a dye reservoir that leaks dye out just below the line of separation where it will track the evolution of vorticity in the flow field. Because of this, we should be able to visualize the span-wise variations in vortex merging process and growth of the shear layer as it moves toward reattachment.

If experiments suggest that upgrade costs for real-time control of the wavelength are justified, then the fabrication of such an upgrade would be quite easy and feedback control schemes could be applied to all features of this actuator. The lessons learned from the various flow control projects on the backward-facing step can then be applied to various other flow geometries since the actuator is portable. This opens up unimaginable possibilities of research projects for the future.

References

Adams EW, Johnston JP (1988a) Effects of the separating shear layer on the reattachment flow structure Part 1: Pressure and turbulence quantities. Experiments in Fluids 6:400-408.

Adams EW, Johnston JP (1988b) Effects of the separating shear layer on the reattachment flow structure Part 2: Reattachment length and wall shear stress. Experiments in Fluids 6:493-499.

Apps C (2001) A Study of Synthetic Fence Jets Using I.C.V. Master's Thesis, University of Alberta, Edmonton.

Apps C, Chen T, Sigurdson L (2003) Image Correlation Velocimetry Applied to Discrete Smoke-wire streaklines in Turbulent Pipe Flow. Experiments In Fluids 35:288-290.

Armaly BF, Durst F, Pereira JCF, Schonung B (1983) Experimental and theoretical investigation of backward-facing step flow. J. Fluid Mechanics 127:473-496.

Bewley TR, Moin P, Temam R (2001) DNS-based predictive control of turbulence: an optimal benchmark for feedback algorithms. J. Fluid Mechanics 447:179-225.

Bhattacharjee S, Scheelke B, Trout TR (1986) Modification of Vortex Interactions in a Reattaching Separated Flow. AIAA Journal 24:4:623:629.

Choi H, Hinze M, Kunisch K (1999) Instantaneous control of backward-facing step flows. Applied numerical Mathematics 31 133-158.

Chun KB, Sung HJ (1996) Control of turbulent separated flow over a backward-facing step by local forcing. Experiments in Fluids 21:417-426.

Chun KB, Sung HJ (1998) Visualization of a locally-forced separated flow over a backward-facing step. Experiments in fluids 25:133-142.

Chun KB, Lee I, Sung HJ (1999) Effect of spanwise-varying local forcing on turbulent separated flow over a backward-facing step. Experiments in Fluids 26:437-440.

Dejoan A, Leschziner MA, (2004) Large Eddy simulation of periodically perturbed separated flow over a backward-facing step. Int. J. Heat and Fluid Flow 25:581-592.

Dejoan A, Jang Y-J, Leschziner MA, (2005) Comparative LES and Unsteady RANS Computations for a Periodically-Perturbed Separated Flow over a Backward-Facing Step. J.Fluids Engineering: Transactions of the ASME 127:872-878.

Faulkner (2006) Private Communication

Gad-el-Hak M (2000) Flow Control: Passive, Active, and Reactive flow management. Cambridge University press, Cambridge, UK.

Gordon M, Soria J (2002) PIV measurements of a zero-net-mass-flux jet in cross flow. Experiments in Fluids 33: 863-872.

Hasan MAZ (1992) The flow over a backward-facing step under controlled perturbation: laminar separation. J. Fluid Mechanics 238:73-96.

Henning L, King R (2007) Robust Multivariable Closed-Loop Control of a Turbulent Backward-Facing Step Flow. J. Aircraft 44:1:201-208.

Kang S, Choi H, (2002) Suboptimal feedback control of turbulent flow over a backward-facing step. J. Fluid Mechanics 463:201-227.

Kim S, Choi H, Yoo J-Y (2007) Effect of Local Forcing on Backward-facing step flow with laminar separation. J. Turbulence 8:6:1-23.

Laberque A, Moreau E, Zouzou N, Touchard G (2007) Separation control using plasma actuators: application to a free turbulent jet. J. Physics D: Applied Physics 40:674-684.

Lai JCS, Yue J, Platzer MF (2002) Control of backward-facing step flow using a flapping foil. Experiments in Fluids 32:44-54.

Le H, Moin P, Kim J (1997) Direct numerical simulation of turbulent flow over a backward-facing step. J. Fluid Mechanics 330:349-374.

Lee I, Sung HJ (2001) Characteristics of wall pressure fluctuation in separated and reattaching flows over a backward-facing step: Part I: time-mean and cross-spectral analyses. Experiments in Fluids 30:262-272

Liang C, Rogers CA (1997) J. Intelligent Material Systems and Structures 8: 303-313.

Lockerby DA, Carpenter PW (2004) Modeling and Design of Microjet Actuators. AIAA Journal 42:2:220-227.

Lofdahl L, Gad-el-Hak M (1999) MEMS applications in turbulence and flow control. Progess in Aerospace Sciences 35:101-203.

Mabey DG (1972) Analysis and Correlation of Data on Pressure Flucturation in Separated Flow. J. Aircraft 9:9:642-645.

Milano M, Koumoutsakos P (2002) A Clustering genetic algorithm for cylinder drag optimization. J. Compuational Physics 175:79-107.

Moreau E (2007) Airflow control by non-thermal plasma actuators. J. Physics D: Applied Physics 40:605-636.

Neumann J, Wengle H (2003) DNS and LES of Passively Controlled Turbulent Backward-Facing Step Flow. Flow, Turbulence and Combustion 71:297-310.

Peacock T, Elizabeth B, Hertzberg J, Lee Y-C (2004) Forcing a planar jet flow using MEMS. Experiments in Fluids 37:22-28.

Roos F, Kegelman JT (1986) Control of Coherent Structures in Reattaching Laminar and Turbulent Shear Layers. AIAA Journal 24:12:1956-1963.

Sakakibara J, Anzai T, (2001) Chain-link-fence structures produced in a plane jet. Physics of fluids 13:6:1541-1544.

Santulli C, Patel SI, Jeronimidis G, Davis FJ, Mitchell GR (2005) Development of smart variable stiffness actuators using polymer hydrogels. Smart Materials and Structures 14: 434-440.

Saric S, Jakirlic S, Tropea C (2005) A periodically perturbed backward-facing step flow by means of LES, DES and T-RANS: An example of Flow separation control. J. Fluids Engineering Transactions of the ASME 127:879-887.

Sigurdson LW (1995) The Structure and control of a turbulent reattaching flow. J. Fluid Mechanics, 298:139-165.

Sigurdson LW (2006) Private communication

Smith BL, Glezer A (1998) The formation and evolution of synthetic jets. Physics of Fluids 10:9:2281-2297.

Tzou HS, Lee H-J, Arnold SM (2004) Smart Materials, Precision Sensors/Actuators, Smart Structures, and Structronic Systems. Mechanics of Advanced Materials and Structures 11:367-393.

Wengle H, Huppertz A, Barwolff G, Janke G (2001) The manipulated transitional brackward-facign step flow: and experimental and direct numerical simulation investigation. European Journal of Mechanics B- Fluids 20:25-46.

Yoshioka S, Obi S, Masuda S (2001a) Turbulence Statistics of periodically perturbed separated flow over backward-facing step. Int. J. of Head and Fluid Flow. 22:393-401.

Yoshioka S, Obi S, Masuda S (2001b) Organized vortex motion in periodically perturbed turbulent separated flow over a backward-facing step. Int. J. Heat and Fluid Flow. 22:301-307.

Chapter 4. Conclusions

In the previous sections we discuss two problems in unsteady flow control. In the research into these problems we determined the actuation parameters that provide the best currently known methods for promoting a desired evolution of vorticity. We can draw certain overlapping conclusions. For both cases, span-wise variations in actuation or vibration cause a desired control objective. It can also be concluded that the mode shape of the vortex induced vibration or actuation distribution is the most important factor in the performance of the span-wise features in our control studies. The span-wise variations can be controlled indirectly through wire tension and tunnel velocity in the case of the wire vibration, and directly in the form of prescribed velocity distributions in the backward-facing step. Therefore, the methods for creating the actuation for these two flows are as unique as their control objectives. The same is true regarding the conclusions made from these research studies.

For the flexible cylinder undergoing vortex induced vibration, we were able to correlate the formation of a new large scale vortex 'void' structure with a span-wise vibration event. The span-wise location of these structures was found to closely correlate with an anti-node in transverse vibration and a node in stream-wise vibration. By selecting appropriate tunnel velocities and cylinder tensions, we could control the span-wise locations at which these nodes and anti-nodes would form. Appropriate tunnel velocities and cylinder tensions can be calculated with the aid of a flexible cylinder vibration model that we developed. Hence, the creation of such span-wise vibration events is an open-loop flow control problem. The values of the vortex shedding frequency and the cylinders natural frequency must be delicately controlled to produce such events.

The structure and the vibration event which causes it are found to be unique. There are a few reasons for this. Firstly, other researchers have not previously published results of flexible cylinder vibrations that are near the required conditions for our 'void' structure. Secondly, the structure includes a pinch-off process involving opposite signed vorticity from other sides of the cylinder wake. To our knowledge, our visualizations are the first presented of interaction of opposite signed vorticity in cylinder flows. This vortex pinch-off process separates our structure from the similar structures of Williamson (1992) as his structures were interaction of same signed vorticity.

Contrary to what is normally done in industrial application of vortex induced vibration, lock-in of the cylinder wake to the 1st mode of the transverse cylinders vibration was desired. This resulted in a highly predictable and reproducible flow configuration where a void structure is always caused at mid cylinder span. By exploiting the well known mode shape theory for a flexible cylinder, existence and span-wise location of the 'void' structure can be correlated to a node in stream-wise vibration and an anti-node in transverse vibration. The result is also calculated by our vibration model.

The hydrogen bubble technique, which has seldom been used in cylinder research, worked well to visualize the wake structures behind the self oscillating wire. We found that the bubbles became trapped in the low pressure cores of the von Karman vortex street, providing excellent visualizations of the vortex structure. Bubbles being shed from the vibrating cylinder provide no measurable disturbance upon the shedding and vibration processes. To prove this we determined that the critical Reynolds number, based on diameter, for the onset of shedding was a very typical value of 47. Common vortex induced vibration results, such as lock-in or synchronization, were not affected by the bubble flow visualization. We also reproduced the large scale vortex "blob" structures of Van Atta et al (1988), showing that their large scale vortex structures are not influenced by the bubbles. Buoyancy related effects of bubbles were also shown to be inconsequential as long as the bubbles are trapped in the vortex street. From these experiments we concluded that bubbles have a little to no influence on the flow and we highly recommend their use in cylinder flows.

For backward-facing step flow control, our control objective was to promote more mixing and rapid growth of the reattaching shear layer. The problem has seen considerable attention in the literature. The actuator was modeled closely after the span-wise variation actuator of Sakakibara and Anzai (2001) which was used experimentally on a planar jet.

This actuator will be the first experimental investigation of adding span-wise variations to a backward-facing step flow, to complement the simulations of Kang and Choi (2002). With the actuator being capable of all testing all of the desired actuation features under open-loop conditions, it will make a significant contribution to the literature with the current design. In the future elaborate feedback control schemes can be applied which use real-time modification all the actuation features. In the current design, actuation wavelength is the only feature not real-time controlled. However, if the costs of the upgrade are deemed acceptable, the actuator could be easily fabricated to include real-time control of this term as well.

The most unique feature of the actuation is the span-wise actuation distribution. This can be any periodic waveform, and it is discretely approximated using 8 or 16 different velocities. A wide variety of span-wise wavelengths, and time varying span-wise phase relationships will be applied as was done by Kang and Choi. Experimental use of this type of actuation on a backward-facing step flow would be the first and would test the conclusions from the numerical experiments of Kang and Choi. Combined with the benefits of multiple frequency forcing (Kim et al, 2007), we would have an actuator that can provide truly unique experiments. The lessons learned from the various flow control projects on the backward-facing step can then be applied to various other flow geometries since the actuator is portable. This opens up unimaginable possibilities of research projects for the future.

In summary, we completed experimental research into two studies regarding unsteady flow control. In both these studies, we found that span-wise variations in vibration or actuation are desirable. For a vibrating cylinder it resulted in the discovery of a completely new large scale vortex structure in the wake. For the control of a backward-facing step, it presents a research opportunity that we will be the first to implement experimentally.

References

Kang S, Choi H, (2002) Suboptimal feedback control of turbulent flow over a backward-facing step. J. Fluid Mechanics 463:201-227.

Kim S, Choi H, Yoo J-Y (2007) Effect of Local Forcing on Backward-facing step flow with laminar separation. J. Turbulence 8:6:1-23.

Sakakibara J, Anzai T, (2001) Chain-link-fence structures produced in a plane jet. Physics of fluids 13:6:1541-1544.

Van Atta CW, Gharib M, Hammache M (1988) Three-dimensional structure of ordered and chaotic vortex streets behind circular cylinders at low Reynolds numbers. Fluid Dynamics Research 3:127-132

Williamson CHK (1992) The Natural and forced formation of spot-like 'vortex dislocations' in the transition of a wake. J. Fluid Mechanics 243:393-441

Appendix A. VIV Model for a Flexible Cylinder

This document outlines the creation of a model for the vortex induced vibration (VIV) of a taut string in a uniform steady cross-flow. In Section A.1, we use Newton's second law to derive the model. After we have discussed the structural components of the model, we talk about the more complex fluctuating lift and drag forces created by vortex shedding. In Section A.2 we show the solution process for the wave equation problems. A similar derivation and the solution procedures can be found in vibration textbooks (Inman 2001), with the exception of the fluid mechanics behind vortex shedding forces. The derivation for these forces comes from various sources.

Appendix A1. Derivation of the Wave Equation Models for Vibration

Fluctuating lift (F_y) and drag (F_z) forces created by vortex shedding result in vortex induced vibration of a flexible cylinder in both the transverse direction (w_y) and the stream-wise direction (w_y). A schematic of this vibration is shown in Figure A1.1.

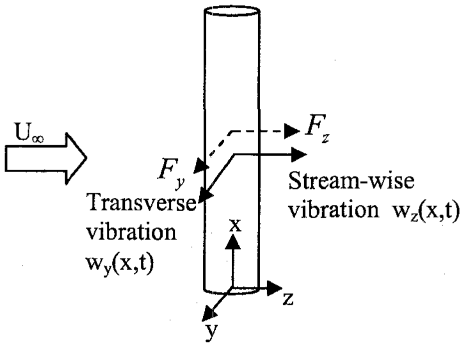

Figure A1.1: General Schematic of Vibration

A1.1. Forces Acting on the Cylinder

To Derive the Wave equation model, not solution at this point, for this 2-D forcing we use a similar derivation to that given by Inman (2001). This derivation starts by taking an Infinitesimal Element of the Wire as in Figure A1.2. We consider differential forces of tension (T; Figure A1.2a), damping forces (f_{damp}; Figure A1.2b) and fluctuating lift and drag forces (f_{lift}; f_{drag}; Figure A1.2c). These forces are decomposed into their respective components in the x, y, and z coordinate system. This is seen in their respective illustrations in Figure A1.2.

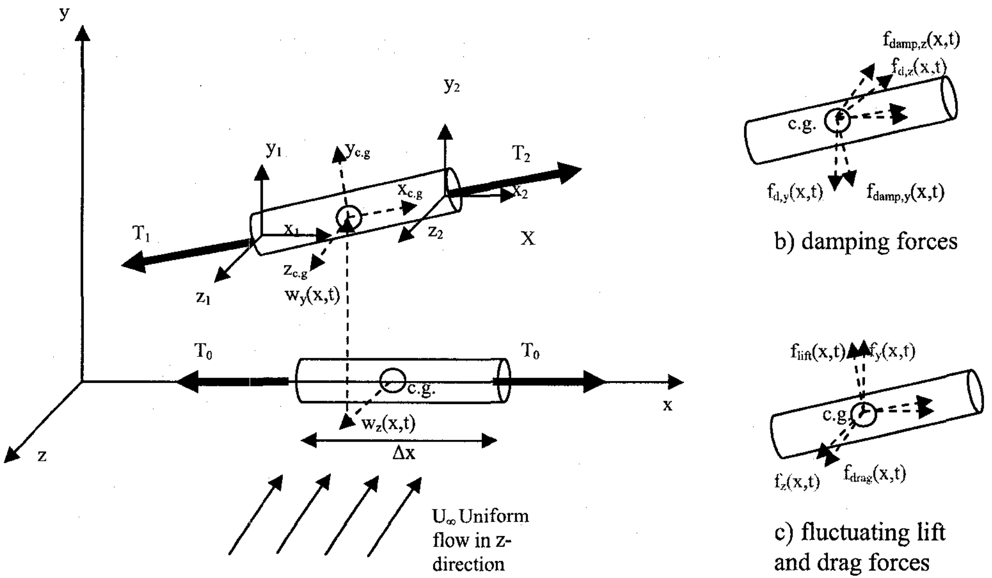

a) initesimal wire element Δx with internal Tension

b) damping forces

c) fluctuating lift and drag forces

Figure A1.2: Infitesimal element of wire and applied forces

From Figure A1.2 we can write force summations using Newton's Second Law along the 3 co-ordinate directions to get:

x-component; $-T_{1x}+T_{2x}-f_{d,x}(x,t)\Delta x+f_x(x,t)\Delta x=\rho A\Delta x\dfrac{\partial^2 w_x(x,t)}{\partial t^2}$ [A-1a]

y-component; $-T_{1y}+T_{2y}-f_{d,y}(x,t)\Delta x+f_y(x,t)\Delta x=\rho A\Delta x\dfrac{\partial^2 w_y(x,t)}{\partial t^2}$ [A-1b]

z-component; $-T_{1z}+T_{2z}-f_{d,z}(x,t)+f_z(x,t)\Delta x=\rho A\Delta x\dfrac{\partial^2 w_z(x,t)}{\partial t^2}$ [A-1c]

where:

Variables defined as components in fixed x,y,z co-ordinate system

T_{1x}, T_{1y}, T_{1z}, T_{2x}, T_{2y}, T_{2z},	internal tension and components
$f_y(x,t)$, $f_z(x,t)$	components of fluctuating $f_{lift}(x,t)$, $f_{drag}(x,t)$
$f_{d,y}(x,t)$, $f_{d,z}(x,t)$	fluid damping components $f_{damp,y}(x,t)$, $f_{damp,z}(x,t)$
$w(x,t)$	position of c.g. of infinitesimal element Δx

Variables defined as components in the mobile $x_{c.g.}$,$y_{c.g.}$,$z_{c.g.}$ system

T_1,T_2	internal tensions
$f_{lift}(x,t)$, $f_{drag}(x,t)$	lift and drag caused by vortex shedding
$f_{damp,y}(x,t)$, $f_{damp,z}(x,t)$	damping forces caused by cylinder motion in fluid

A1.2. Determining Force Components in the Fixed Co-ordinate system (x,y,z)

There are 4 forces acting upon the infinitesimal wire of Figure A1.2. These are internal tension; fluid damping and fluctuating lift and drag forces. Tension, lift and drag force define an orthonormal set of vectors as seen in Figure A1.2. Fluid damping force is created by drag on the wire as it moves relative to the surrounding fluid. For simplicity these vectors are given in the same co-ordinates as the tension, lift drag set. These vectors are related to the global x,y,z co-ordinate set through trigonometry.

A1.2.1. Internal Tension Forces

Consider the Tension Vector T_2 in co-ordinate system (x_2, y_2, z_2) as per Figure A1.3a.

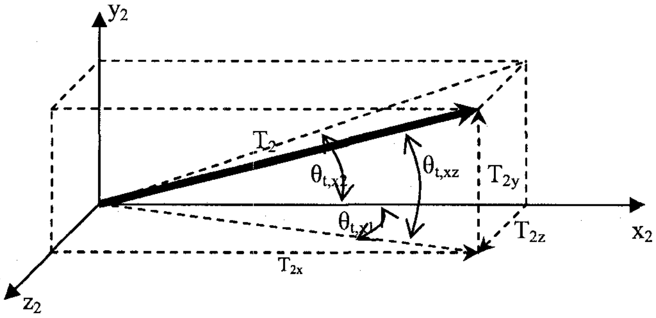

Figure A1.3: Coupled Tension Components of T_2

From Figure A1.4 we can write the T_2 components for equations 1a-c:

$$T_{2x} = T_2 \cos\theta_{t,xz} \cos\theta_{t,x1} \quad \text{[A-2a]}$$

$$T_{2y} = T_2 \sin\theta_{t,xz} \quad \text{[A-2b]}$$

$$T_{2z} = T_2 \cos\theta_{t,xz} \sin\theta_{t,x1} \quad \text{[A-2c]}$$

Knowing that T_1 is an equal and opposite vector on the infinitesimal element, we can write the T_1 component in the x_1 y_1 z_1 as

$$T_{1x} = -T_1 \cos\theta_{t,xz} \cos\theta_{t,x1} \qquad \text{[A-3a]}$$

$$T_{1y} = -T_1 \sin\theta_{t,xz} \qquad \text{[A-3b]}$$

$$T_{1z} = -T_1 \cos\theta_{t,xz} \sin\theta_{t,x1} \qquad \text{[A-3c]}$$

We can write an equation for $\cos\theta_{t,xz}$ using only the angles $\tan\theta_{t,x1}$ and $\tan\theta_{t,x2}$ these angles are special as they are defined only in the x-z and x-y planes. Using Figure A1.3 these angles can be written as follows:

$$\tan\theta_{t,x1} = \frac{T_{2z}}{T_{2x}} \qquad \text{[A-4a]}$$

$$\tan\theta_{t,x2} = \frac{T_{2y}}{T_{2x}} \qquad \text{[A-4b]}$$

The coupled relation is then:

$$\cos\theta_{t.xz} = \frac{\sqrt{T_{2x}^2 + T_{2z}^2}}{\sqrt{{T_{2x}}^2 + T_{2y}^2 + {T_{2z}}^2}} = \frac{\sqrt{1+\tan^2\theta_{t,x1}}}{\sqrt{1+\tan^2\theta_{t,x2} + \tan^2\theta_{t,x1}}} \qquad \text{[A-5a]}$$

$$\sin\theta_{t.xz} = \frac{T_{2y}}{\sqrt{{T_{2x}}^2 + T_{2y}^2 + {T_{2z}}^2}} = \frac{\tan\theta_{t,x2}}{\sqrt{1+\tan^2\theta_{t,x2} + \tan^2\theta_{t,x1}}} \qquad \text{[A-5b]}$$

Since the tension vector is aligned primarily in the x direction due to the small angles of vibration, it is reasonable to assume that:

$T_{2x} >> T_{2y}$ and $T_{2x} >> T_{2y}$

Therefore,

$$\sin\theta_{t.xz} = \frac{T_{2y}}{\sqrt{{T_{2x}}^2 + T_{2y}^2 + {T_{2z}}^2}} \cong \frac{T_{2y}}{T_{2x}} = \tan\theta_{t,x2} \qquad \text{[A-6a]}$$

$$\cos\theta_{t.xz} = \frac{\sqrt{T_{2x}^2 + T_{2z}^2}}{\sqrt{{T_{2x}}^2 + T_{2y}^2 + {T_{2z}}^2}} \cong \frac{T_{2x}}{T_{2x}} = 1 \qquad \text{[A-6b]}$$

Furthermore, vibrations amplitudes in this experiment are of very small amplitude and are not visible to the naked eye, therefore a small angle assumption can be made for $\theta_{t,x1}$ and $\theta_{t,x2}$.

$$\sin\theta_{t,x1} \cong \tan\theta_{t,x1} = \left.\frac{\partial w_z(x,t)}{\partial x}\right|_{x_1} \; ; \; \sin\theta_{t.xz} \cong \tan\theta_{t,x2} \cong \left.\frac{\partial w_y(x,t)}{\partial x}\right|_{x_1}$$

$$\sin\theta_{t,x2} \cong \tan\theta_{t,x2} = \left.\frac{\partial w_z(x,t)}{\partial x}\right|_{x_2} \; ; \; \sin\theta_{t.xz} \cong \tan\theta_{t,x2} = \left.\frac{\partial w_y(x,t)}{\partial x}\right|_{x_2} \qquad \text{[A-7]}$$

Substituting A-6 and A-7 into A-2a to c we get the decoupled T₂ tension vectors:

$$T_{2x} = T_2 \cos\theta_{t,xz} \cos\theta_{t,x1} = T_2 \qquad \text{[A-8a]}$$

$$T_{2y} = T_2 \sin\theta_{t,xz} = T_2 \tan\theta_{t,x2} = T_2 \left.\frac{\partial w_y(x,t)}{\partial x}\right|_{x_2} \qquad \text{[A-8b]}$$

$$T_{2z} = T_2 \cos\theta_{t,xz} \sin\theta_{t,x1} = T_2 \left.\frac{\partial w_z(x,t)}{\partial x}\right|_{x_2} \qquad \text{[A-8c]}$$

Substituting A-6 and A-7 into A-3a to c we get the decoupled T₁ tension vectors:

$$T_{1x} = -T_1 \cos\theta_{t,xz} \cos\theta_{t,x1} = -T_1 \qquad \text{[A-9a]}$$

$$T_{1y} = -T_1 \sin\theta_{t,xz} = -T_1 \tan\theta_{t,x2} = -T_1 \left.\frac{\partial w_y(x,t)}{\partial x}\right|_{x_1} \qquad \text{[A-9b]}$$

$$T_{1z} = -T_1 \cos\theta_{t,xz} \sin\theta_{t,x1} = -T_1 \left.\frac{\partial w_z(x,t)}{\partial x}\right|_{x_1} \qquad \text{[A-9c]}$$

A1.2.2. Fluctuating Lift and Drag Forces

Consider the lift force vector F_{lift} in co-ordinate system ($x_{c.g.}$, $y_{c.g.}$, $z_{c.g.}$).

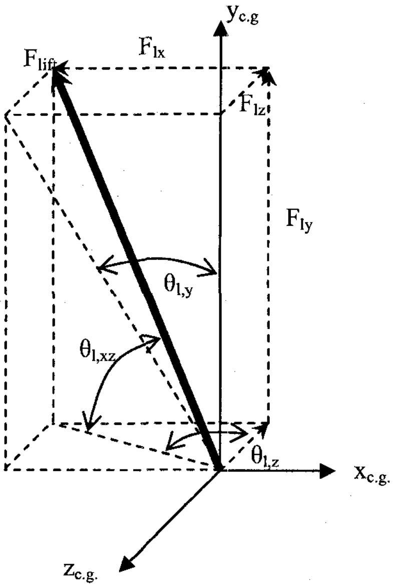

Figure A1.4: Components of Fluctuating Lift

The fluid dynamics behind $\vec{F}_{lift}$ will be discussed in Section A1.6. At this point we will say that $\vec{F}_{lift} = f\left(t, x, C_l, A_y, A_z, \mathrm{Re}_d\right)$ is a function of time, span-wise location, lift coefficient and vibration amplitude.

From Figure A1.4, the components of the Lift Force are

$$F_{lx} = F_{lift} \cos\theta_{l,xz} \sin\theta_{l,z} \qquad \text{[A-10a]}$$

$$F_{ly} = F_{lift} \sin\theta_{l,xz} \qquad \text{[A-10b]}$$

$$F_{lz} = F_{lift} \cos\theta_{l,xz} \cos\theta_{l,z} \qquad \text{[A-10c]}$$

We can write an equation for $\cos\theta_{l,xz}$ using only the angles $\tan\theta_{l,z}$ and $\tan\theta_{l,y}$ these angles are special as they are defined only in the x-z and x-y planes and show coupling. Using Figure A1.4, these angles can be written as follows:

$$\tan\theta_{l,z} = \frac{F_{lx}}{F_{lz}} \qquad \text{[A-11a]}$$

$$\tan\theta_{l,y} = \frac{F_{lx}}{F_{ly}} \qquad \text{[A-11b]}$$

The coupled relation is then:

$$\cos\theta_{l.xz} = \frac{\sqrt{F_{lx}^2 + F_{lz}^2}}{\sqrt{F_{lx}^{\ 2} + F_{ly}^2 + F_{lz}^{\ 2}}} = \frac{\sqrt{1 + \frac{1}{\tan^2\theta_{l,z}}}}{\sqrt{1 + \frac{1}{\tan^2\theta_{l,y}} + \frac{1}{\tan^2\theta_{l,z}}}} \qquad \text{[A-12a]}$$

$$\sin\theta_{l.xz} = \frac{F_{ly}}{\sqrt{F_{lx}^{\ 2} + F_{ly}^2 + F_{lz}^{\ 2}}} = \frac{\frac{1}{\tan\theta_{l,y}}}{\sqrt{1 + \frac{1}{\tan^2\theta_{l,y}} + \frac{1}{\tan^2\theta_{l,z}}}} \qquad \text{[A-12b]}$$

The lift force is primarily aligned in the transverse direction; therefore the other components will be quite small. Therefore, it is reasonable to assume that:

$F_{ly} >> F_{lx}$ and $F_{ly} >> F_{lz}$

$$\cos\theta_{l.xz} = \frac{\sqrt{F_{lx}^2 + F_{lz}^2}}{\sqrt{F_{lx}^{\ 2} + F_{ly}^2 + F_{lz}^{\ 2}}} \approx 0 \qquad \text{[A-13a]}$$

$$\sin\theta_{l.xz} = \frac{F_{ly}}{\sqrt{F_{lx}^{\ 2} + F_{ly}^2 + F_{lz}^{\ 2}}} \approx 1 \qquad \text{[A-13b]}$$

With conditions of A-13 it can be seen that the lift forces decouple into:

$$F_{lx} = F_{lift}\cos\theta_{l,xz}\sin\theta_{l,z} = 0 \qquad \text{[A-14a]}$$

$$F_{ly} = F_{lift}\sin\theta_{l,xz} = F_{y} \qquad \text{[A-14b]}$$

$$F_{lz} = F_{lift}\cos\theta_{l,xz}\cos\theta_{l,z} = 0 \qquad \text{[A-14c]}$$

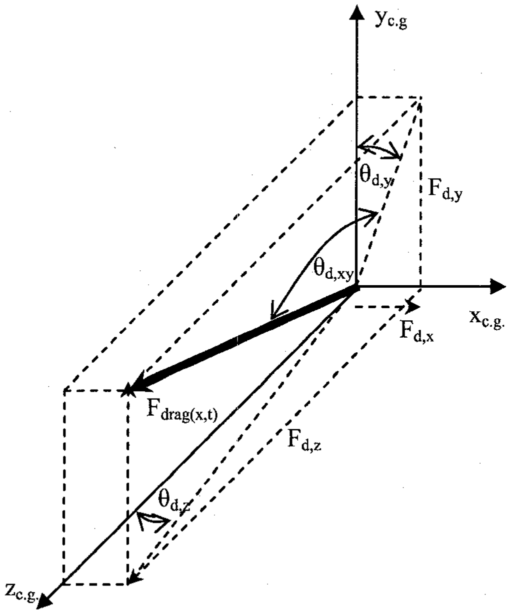

Figure A1.5: Components of Fluctuating Drag

The fluid dynamics behind $\vec{F}_{drag}$ will be discussed in section A1.6. At this point we will say that $\vec{F}_{drag} = f\left(t, x, C_d, A_y, A_z, \mathrm{Re}_d\right)$ is a function of time, span-wise location, and drag coefficient and vibration amplitude.

The components of fluctuating Drag Force are:

$$F_{dx} = F_{drag}\cos\theta_{d,xy}\sin\theta_{d,y} \qquad \text{[A-15a]}$$

$$F_{dy} = F_{drag}\cos\theta_{d,xy}\cos\theta_{d,y} \qquad \text{[A-15b]}$$

$$F_{dz} = F_{drag}\sin\theta_{d,y} \qquad \text{[A-15c]}$$

We can write an equation for $\cos\theta_{d,xy}$ using only the angles $\tan\theta_{d,z}$ and $\tan\theta_{d,y}$ these angles are special as they are defined only in the x-z and x-y planes and show coupling. These angles can be written as follows:

$$\tan\theta_{d,z} = \frac{F_{dx}}{F_{dz}} \qquad \text{[A-16a]}$$

$$\tan\theta_{d,y} = \frac{F_{dx}}{F_{dy}} \qquad \text{[A-16b]}$$

The coupled relation is then:

$$\cos\theta_{d.xy} = \frac{\sqrt{F_{dx}^2 + F_{dy}^2}}{\sqrt{F_{dx}^{\ 2} + F_{dy}^2 + F_{dz}^{\ 2}}} = \frac{\sqrt{1+\dfrac{1}{\tan^2\theta_{d,y}}}}{\sqrt{1+\dfrac{1}{\tan^2\theta_{d,y}}+\dfrac{1}{\tan^2\theta_{d,z}}}} \qquad \text{[A-17a]}$$

$$\sin\theta_{d.xy} = \frac{F_{dz}}{\sqrt{F_{dx}^{\ 2} + F_{dy}^2 + F_{dz}^{\ 2}}} = \frac{\dfrac{1}{\tan\theta_{d,z}}}{\sqrt{1+\dfrac{1}{\tan^2\theta_{d,y}}+\dfrac{1}{\tan^2\theta_{d,z}}}} \qquad \text{[A-17b]}$$

Similarly, fluctuating drag is a dominant force in the stream-wise direction. Due to the small angles of the wire deflection it is reasonable to assume that $F_{dz} >> F_{dx}$ and $F_{dz} >> F_{dy}$ so it is anticipated that:

$$\cos\theta_{d.xy} = \frac{\sqrt{F_{dx}^2 + F_{dy}^2}}{\sqrt{F_{dx}^{\ 2} + F_{dy}^2 + F_{dz}^{\ 2}}} \cong 0 \qquad \text{[A-18a]}$$

$$\sin\theta_{d.xy} = \frac{F_{dz}}{\sqrt{F_{dx}^{\ 2} + F_{dy}^2 + F_{dz}^{\ 2}}} = 1 \qquad \text{[A-18b]}$$

With this it is seen that the fluctuating drag equations A-15 a-c decouple into:

$$F_{dx} = F_{drag}\cos\theta_{d,xy}\sin\theta_{d,y} = 0 \qquad \text{[A-19a]}$$

$$F_{dy} = F_{drag}\cos\theta_{d,xy}\cos\theta_{d,y} = 0 \qquad \text{[A-19b]}$$

$$F_{dz} = F_{drag}\sin\theta_{d,y} = F_z \qquad \text{[A-19c]}$$

A1.2.3. Damping Forces

The force opposes the relative motion between the fluid and the wire. It has both structural and fluid effects. At this point we are simply talking force vectors regardless of the fluid dynamics involved.

Damping in the y direction follows the same component decomposition as would the fluctuating lift force. The major difference is that the coefficients $\vec{F}_{lift}$ and $\vec{F}_{damp,y}$ may have the different sign and quite a different magnitude. The components of the damping forces in the fixed co-ordinate system are:

$$F_{dy,x} = F_{damp,x} \cos\theta_{l,xz} \sin\theta_{l,z} \quad \text{[A-20a]}$$

$$F_{dy,y} = F_{damp,y} \sin\theta_{l,xz} \quad \text{[A-20b]}$$

$$F_{dy,z} = F_{damp,z} \cos\theta_{l,xz} \cos\theta_{l,z} \quad \text{[A-20c]}$$

Using the same decoupling arguments for $\cos\theta_{l,xz}$ that were made in equation A-13 we get the uncoupled y damping terms:

$$F_{dy,x} = F_{damp,x} \cos\theta_{l,xz} \sin\theta_{l,z} = 0 \quad \text{[A-21a]}$$

$$F_{dy,y} = F_{damp,y} \sin\theta_{l,xz} = F_{damp,y} \quad \text{[A-21b]}$$

$$F_{dy,z} = F_{damp,z} \cos\theta_{l,xz} \cos\theta_{l,z} = 0 \quad \text{[A-21c]}$$

Damping in the z direction follows the same component decomposition as would the fluctuating drag force. The major difference is that the coefficients $\vec{F}_{drag}$ and $\vec{F}_{damp,z}$ may have the different sign a quite a different magnitude.

$$F_{dz,x} = F_{damp,z} \cos\theta_{d,xy} \sin\theta_{d,y} \quad \text{[A-22a]}$$

$$F_{dz,y} = F_{damp,z} \cos\theta_{d,xy} \cos\theta_{d,y} \quad \text{[A-22b]}$$

$$F_{dz,z} = F_{damp,z} \sin\theta_{d,xy} \quad \text{[A-22c]}$$

For damping in the z direction Equations A-22 a-c decouple using the conditions derived for the fluctuating drag force in equation A-18.

$$F_{dz,x} = F_{damp,z} \cos\theta_{d,xy} \sin\theta_{d,y} = 0 \qquad \text{[A-23a]}$$

$$F_{dz,y} = F_{damp,z} \cos\theta_{d,xy} \cos\theta_{d,y} = 0 \qquad \text{[A-23b]}$$

$$F_{dz,z} = F_{damp,z} \sin\theta_{d,xy} = F_{damp,z} \qquad \text{[A-23c]}$$

A1.3. Final Force Balances of All Forces

Along the axis of the wire, T_1 and T_2 can be related to the initial tension of the wire T_0 by using a Force balance along the span of the wire (eq'n 1a). Substituting 19a and 20a into 1a we get

$$-T_1 + T_2 - 0 + 0 = \rho A \Delta x \frac{\partial^2 w_x(x,t)}{\partial t^2} \qquad \text{[A-24]}$$

We neglect any minor time varying elongation along the wire:

$$\frac{\partial^2 w_x(x,t)}{\partial t^2} \cong 0 \qquad \text{[A-25]}$$

And we get:

$$T_1 = T_2 = T \qquad \text{[A-26]}$$

Hence tension in essentially constant along the wire.

Substituting 19b, 20b, 25b and 26b into equation 1b we get a force balance for the transverse (y) direction

$$-T_1 \left.\frac{\partial w_y(x,t)}{\partial x}\right|_{x1} + T_2 \left.\frac{\partial w_y(x,t)}{\partial x}\right|_{x2} - F_{damp,y}(x,t)\Delta x + F_{lift}(x,t)\Delta x = \rho A \Delta x \frac{\partial w_y^2(x,t)}{\partial t^2}$$

[A-27]

Substituting 19c, 20c, 25c and 26c into equation 1c we get a force balance for the stream-wise (z) direction

$$-T_1\left.\frac{\partial w_z(x,t)}{\partial x}\right|_{x1}+T_2\left.\frac{\partial w_z(x,t)}{\partial x}\right|_{x2}-F_{damp,z}(x,t)\Delta x+F_{drag}(x,t)\Delta x=\rho A\Delta x\frac{\partial w_z^2(x,t)}{\partial t^2}$$

[A-28]

A1.4. Wave Equation Model with Damping

To finalize the problem model we must make use of the Taylor Series Expansion of

$$T\left.\frac{\partial w(x,t)}{\partial x}\right|_{x_2} \qquad \text{[A-29]}$$

The 2 term Taylor Series expansion of this term is:

$$T\left.\frac{\partial w(x,t)}{\partial x}\right|_{x_2} = T\left.\frac{\partial w(x,t)}{\partial x}\right|_{x_1} + \Delta x\frac{\partial}{\partial x}\left.\left(T\frac{\partial w(x,t)}{\partial x}\right)\right|_{x_1} + O(\Delta x^2) \qquad \text{[A-30]}$$

Substituting of Taylor Series for respective components gives;

$$\Delta x\frac{\partial}{\partial x}\left.\left(T\frac{\partial w_y(x,t)}{\partial x}\right)\right|_{x_1} - F_{damp,y}(x,t)\Delta x + F_{lift}(x,t)\Delta x = \rho A\Delta x\frac{\partial^2 w_y(x,t)}{\partial t^2}$$

[A-31a]

$$\Delta x\frac{\partial}{\partial x}\left.\left(T\frac{\partial w_z(x,t)}{\partial x}\right)\right|_{x_1} - F_{damp,z}(x,t)\Delta x + F_{drag}(x,t)\Delta x = \rho A\Delta x\frac{\partial^2 w_z(x,t)}{\partial t^2}$$

[A-31b]

We divide by Δx, omit the unnecessary x_1 subscript while noting that T is constant as determined from equation 27 to arrive at the non-homogeneous wave equation problem with fluid damping for each component of wire vibration

$$\rho A\frac{\partial^2 w_y(x,t)}{\partial t^2} + F_{damp,y}(x,t) - T\frac{\partial w_y(x,t)}{\partial x} = F_y(x,t,A_y,A_z,\mathrm{Re}_D) \qquad \text{[A-32a]}$$

$$\rho A\frac{\partial^2 w_z(x,t)}{\partial t^2} + F_{damp,z}(x,t) - T\frac{\partial w_z(x,t)}{\partial x} = F_z(x,t,A_y,A_z,\mathrm{Re}_D) \qquad \text{[A-32b]}$$

Accepted Damping models will be shown to follow the form:

$$F_{damp}(x,t) = \gamma\frac{\partial w}{\partial t} \qquad \text{[A-33]}$$

Defining the Wave Speed as:

$$c^2 = \frac{T}{\rho A}$$

we get equations that resemble the non-homogeneous wave equation, but with an added damping force term:

$$\frac{\partial^2 w_y(x,t)}{\partial t^2} + \frac{\gamma_y}{\rho A}\frac{\partial w_y(x,t)}{\partial t} - c^2 \frac{\partial^2 w_y(x,t)}{\partial x^2} = F_y(x,t,A_y,A_z,\mathrm{Re}_d) \qquad \text{[A-34a]}$$

$$\Delta x \frac{\partial^2 w_z(x,t)}{\partial t^2} + \frac{\gamma_z}{\rho A}\frac{\partial w_y(x,t)}{\partial t} - c^2 \frac{\partial^2 w_z(x,t)}{\partial x^2} = F_z(x,t,A_y,A_z,\mathrm{Re}_d) \qquad \text{[A-34b]}$$

A1.5. Fluid Mechanics Considerations

The first fluid dynamic consideration of note is the influences of added mass upon the wave speed. The wave speed is calculated using:

$$c = \sqrt{\frac{T}{(\rho_c + \Delta\rho_f)A}}$$

For the purposes of our study we will use the typical added mass coefficient definition:

$$\Delta\rho_f A = C_a \rho_{water} A_{cylinder}$$

Therefore the effective density for calculating the wave speed is:

$$\rho_{effective} = \rho_c + C_a \rho_{water}$$

When using air as the working fluid, the added mass term is generally negligible. However, since the density of the steel is approximately 8000kg/m^3 and the water density is nominally 1000kg/m^3 the added mass term is important. Sarpkaya (1978, 2004) shows how the added mass could be between -0.5 and 1.5 depending on the experimental conditions encountered in our experiments. Similar results are reproduced by Zhou et al (2000) and Willden and Graham (2001).

The second fluid dynamic consideration is related to fluid and structural damping. From equation A-34a and b we see the damping term:

$$\frac{\gamma}{\rho A}\frac{\partial w\,(x,t)}{\partial t}$$

The damping coefficient is actually the sum of structural and fluid damping values:

$\gamma = \gamma_s + \gamma_f$. Therefore the damping terms can be written as:

$$\frac{\gamma}{\rho A}\frac{\partial w\,(x,t)}{\partial t} = \frac{\gamma_s}{\rho A}\frac{\partial w\,(x,t)}{\partial t} + \frac{\gamma_f}{\rho A}\frac{\partial w\,(x,t)}{\partial t} \qquad \text{[A-35]}$$

The structural term, ideally, is controllable by the researcher. The fluid dynamic damping term is accounted for in the forcing terms F_z and F_y.

The third and final fluid dynamic consideration relates to the definition of the unsteady forces imposed by vortex shedding. The coupling between $F_y(x,t,A_y,A_z,\mathrm{Re}_d)$ and $F_z(x,t,A_y,A_z,\mathrm{Re}_d)$ can be quite complex. We will use force decomposition methods as developed for the mechanically oscillated cylinder (Sarpkaya, 1978) and for the 2-D VIV data of Zhou et al (2000). The method uses Fourier averages of many cycles of the pressure distribution along the cylinder to determine force transfer coefficients F_{dl} and F_{ml}. These terms are the unsteady drag, out of phase component, and inertial, in phase component of the cylinder forces as compared with the cylinder motion. The decomposition is written as:

$$F_y(t) = -F_{dl,y}\cos(\omega_{vs}t) + F_{ml,y}\sin(\omega_{vs}t)\,. \qquad \text{[A-36a]}$$

It has been shown that the cylinder vibrations is very closely related to the vortex shedding frequency for low Red and lower mass ratios less than 10 (Wilden and Graham, 2006). They showed that when the cylinder is not locked in $\omega_{vs} \approx \omega_s$. When the cylinder is locked in, they showed that the cylinder and wake respond very close to the cylinders in fluid natural frequency, $\omega_{vs} \approx \omega_n$.

For in-line vibration we can use the well known frequency doubling effect (Jauvtis and Williamson, 2004; Sarpkaya, 2004) to write:

$$F_z(x,t) = -F_{dl,z}\cos(2\omega_{vs}t) + F_{ml,z}\sin(2\omega_{vs}t)\,. \qquad \text{[A-36b]}$$

To be consistent with flexible cylinder results of Newman and Kariadakis (1996, 1997), Huarte et al (2006), and Willden and Graham (2001), we can add span-wise distribution of force which corresponds closely to the mode shape eigenfunctions $X(x)$ which is determined during the solution procedure.

$$F_y(x,t) = X(x)\left(-F_{dl,y}\cos(\omega_{vs}t) + F_{ml,y}\sin(\omega_{vs}t)\right) \qquad \text{[A-37a]}$$

$$F_z(x,t) = X(x)\left(-F_{dl,y}\cos(2\omega_{vs}t) + F_{ml,y}\sin(2\omega_{vs}t)\right) \qquad \text{[A-37b]}$$

A1.6. Final Wave Equation Model

Combining Equations A-37 a and b with Equation A-34 a and b we get the wave equation model that we will solve in section A2 of this appendix.

$$\frac{\partial^2 w_y(x,t)}{\partial t^2} + \frac{\gamma_{s,y}}{\rho A}\frac{\partial w_y(x,t)}{\partial t} - c^2\frac{\partial^2 w_y(x,t)}{\partial x^2} = \qquad \text{[A-38a]}$$
$$X(x)\left(-F_{dl,y}\cos(\omega_{vs}t) + F_{ml,y}\sin(\omega_{vs}t)\right)$$

$$\frac{\partial^2 w_z(x,t)}{\partial t^2} + \frac{\gamma_{s,z}}{\rho A}\frac{\partial w_y(x,t)}{\partial t} - c^2\frac{\partial^2 w_z(x,t)}{\partial x^2} = \qquad \text{[A-38b]}$$
$$X(x)\left(-F_{dl,z}\cos(2\omega_{vs}t) + F_{ml,z}\sin(2\omega_{vs}t)\right)$$

Appendix A2. Solution to the Wave Equation VIV Problem

Full details of the solution procedure to partial differential equations of A-38a and b can be found in many vibrations textbooks under sections dealing with systems with distributed parameter or continuous vibration. The author is referred to Inman (2001) for a very similar solution procedure derivation.

The solution procedure first starts by assuming that modal vibration solutions to these equations come in the form:

$$w_n(x,t) = X_n(x)T_n(t) \qquad \text{[A-39]}$$

Such an assumption makes use of the orthogonality condition of the eigenfunctions $X_n(x)$ to reduce the partial differential equation to two ordinary differential equations (ode). $T_n(t)$ defines the time response. It must be solved for using the non-homogeneous problems of equations A-38a and b.

A2.1. Determining the Mode Shapes of Vibration X$_n$(x)

To solve for $X_n(x)$ we can solve the model responses of the homogeneous equation of A-38a and b:

$$\frac{\partial^2 w_{y,n}(x,t)}{\partial t^2}+\frac{\gamma_y}{\rho A}\frac{\partial w_{y,n}(x,t)}{\partial t}-c^2\frac{\partial^2 w_{y,n}(x,t)}{\partial x^2}=0 \qquad \text{[A-40a]}$$

$$\frac{\partial^2 w_{z,n}(x,t)}{\partial t^2}+\frac{\gamma_z}{\rho A}\frac{\partial w_{z,n}(x,t)}{\partial t}-c^2\frac{\partial^2 w_{z,n}(x,t)}{\partial x^2}=0 \qquad \text{[A-40b]}$$

For the y vibration problem, we substitute $w_{y,n}(x,t)=X_{y,n}(x)T_{y,n}(t)$ into A-40a to get:

$$X_{y,n}(x)\frac{d^2T_{y,n}(t)}{dt^2}+\frac{\gamma_y}{\rho A}X_{y,n}(x)\frac{dT_{y,n}(t)}{dt}-c^2\frac{d^2X_{y,n}(x)}{dt^2}T_{y,n}(t)=0$$

For the y vibration problem we get:

$$X_{y,n}(x)\left[\frac{d^2T_{y,n}(t)}{dt^2}+\frac{\gamma_y}{\rho A}\frac{dT_{y,n}(t)}{dt}\right]=c^2\frac{d^2X_{y,n}(x)}{dt^2}T_{y,n}(t)$$

Moving functions of x to the right side and functions of t to the left side we get:

$$\frac{\left[\frac{d^2T_{y,n}(t)}{dt^2}+\frac{\gamma_y}{\rho A}\frac{dT_{y,n}(t)}{dt}\right]}{c^2T_{y,n}(t)}=\frac{\frac{d^2X_{y,n}(x)}{dt^2}}{X_{y,n}(x)}=-\sigma^2.$$

Hence the problem is separated into two ode. The modal equation is:

$$\frac{d^2X_{y,n}(x)}{dt^2}+\sigma^2X_{y,n}(x)=0 \qquad \text{[A-41]}$$

with boundary conditions X$_{y,n}$(0)=0, X$_{y,n}$(L)=0. The solution is:

$$X_{y,n}(x)=\sin\left(\frac{n\pi x}{L}\right). \qquad \text{[A-42]}$$

From similar analysis we can see that the z-vibration ode is in the form:

$$\frac{d^2X_{z,n}(x)}{dt^2}+\sigma^2X_{z,n}(x)=0.$$

With the boundary conditions $X_{z,n}(0)=0$, $X_{z,n}(L)=0$. The solution is identical to the y vibration mode shapes. Therefore,

$$X_n(x)=X_{y,n}(x)=X_{z,n}(x)=\sin\left(\frac{n\pi x}{L}\right).$$

A2.2. Solution to the Temporal Equation $T_n(t)$

In this section we solve the temporal response each mode shape. We first start by substituting the mode shape into the assumed solution A-39 to get:

$$w_n(x,t)=\sin\left(\frac{n\pi x}{L}\right)T_n(t) \qquad \text{[A-43]}$$

Consider the solution to temporal modal response of the n^th^ mode of the transverse vibration. The wave equation problem for the n^th^ mode is given by equation A-38a as:

$$\frac{\partial^2 w_{y,n}(x,t)}{\partial t^2}+\frac{\gamma_{s,y,n}}{\rho A}\frac{\partial w_{y,n}(x,t)}{\partial t}-c^2\frac{\partial^2 w_{y,n}(x,t)}{\partial x^2}= \qquad \text{[A-44]}$$
$$X_n(x)\left(-F_{dl,y}\cos(\omega_{vs}t)+F_{ml,y}\sin(\omega_{vs}t)\right)$$

We substitute equation A-43 into A-44 and simplify we get:

$$\sin\left(\frac{n\pi x}{L}\right)\left[T''_{n,y}(t)+\frac{\gamma_y}{\rho A}T'_{n,y}(t)-c^2\left[-\left(\frac{n\pi}{L}\right)^2\right]T_{n,y}(t)\right]= \qquad \text{[A-45]}$$
$$\sin\left(\frac{n\pi x}{L}\right)\frac{\left(-F'_{dl,y}\cos(\omega_{vs}t)+F'_{ml,y}\sin(\omega_{vs}t)\right)}{\rho A}$$

To make use of orthogonality we multiply through by $X_n(x)=\sin\left(\frac{n\pi x}{L}\right)$ and integrate over the wire span [0,L].

$$\left[T''_{n,y}(t)+\frac{\gamma_y}{\rho A}T'_{n,y}(t)-c^2\left[-\left(\frac{n\pi}{L}\right)^2\right]T_{n,y}(t)\right]\int_0^L\sin\left(\frac{n\pi x}{L}\right)\sin\left(\frac{n\pi x}{L}\right)dx=$$
$$\frac{\left(-F'_{dl,y}\cos(\omega_{ex}t)+F'_{ml,y}\sin(\omega_{ex}t)\right)}{\rho A}\int_0^L\sin\left(\frac{n\pi x}{L}\right)\sin\left(\frac{n\pi x}{L}\right)dx$$

The orthogonality condition requires:

$$\int_0^L \sin\left(\frac{n\pi x}{L}\right)\sin\left(\frac{n\pi x}{L}\right)dx = \frac{L}{2} \text{ for all n.}$$

Therefore, temporal solution to the wave equation decouples into an ordinary differential equation in t:

$$T''_{n,y}(t) + \frac{\gamma_y}{\rho A}T'_{n,y}(t) + \left(\frac{cn\pi}{L}\right)^2 T_{n,y}(t) = \frac{\left(-F'_{dl,y}\cos(\omega_{vs}t) + F'_{ml,y}\sin(\omega_{vs}t)\right)}{\rho A} \qquad \text{[A-46]}$$

To make use of existing solutions to such an ordinary differential equation, we change the ode into the standard form.

$$T''_{n,y}(t) + 2\zeta_{n,y}\omega_n T'_{n,y}(t) + \omega_n{}^2 T_{n,y}(t) = \left(-f'_{dl,y}\cos(\omega_{vs}t) + f'_{ml,y}\sin(\omega_{vs}t)\right) \qquad \text{[A-47]}$$

where:

$$\zeta_{n,y} = \frac{\gamma_y L}{2cn\pi\rho A}, \omega_n = \frac{cn\pi}{L}, f_{dl,y} = \frac{-F_{dl,y}}{\rho A}, f_{ml,y} = \frac{F_{ml,y}}{\rho A}$$

The steady state solution to this ode with arbitrary periodic input can be given as:

$$T_{n,y}(t) = X_{dl,n,y}\cos\left(\omega_{vs}t - \theta_{dl,n,y}\right) + X_{ml,n,y}\sin\left(\omega_{vs}t - \theta_{ml,n,y}\right) \qquad \text{[A-48a]}$$

where:

$$X_{dl,y} = \frac{f_{dl,y}}{\sqrt{\left(\omega_n^2 - \omega_{vs}{}^2\right)^2 + \left(2\zeta_{n,y}\omega_n\omega_{vs}\right)^2}}, \ \theta_{n,y} = \tan^{-1}\left(\frac{2\zeta_y\omega_n\omega_{vs}}{\omega_n^2 - \omega_{vs}^2}\right)$$

$$X_{ml,y} = \frac{f_{ml,y}}{\sqrt{\left(\omega_n^2 - \omega_{vs}{}^2\right)^2 + \left(2\zeta_{n,y}\omega_n\omega_{vs}\right)^2}}$$

Similarly for the z vibration:

$$T_{n,z}(t) = X_{dl,n,z}\cos\left(\omega_{vs}t - \theta_{dl,n,z}\right) + X_{ml,n,z}\sin\left(\omega_{vs}t - \theta_{ml,n,z}\right) \qquad \text{[A-48b]}$$

where:

$$X_{dl,z} = \frac{f_{dl,z}}{\sqrt{\left(\omega_n^2 - (2\omega_{vs})^2\right)^2 + \left(2\zeta_{n,z}\omega_n(2\omega_{vs})\right)^2}}, \ \theta_{n,z} = \tan^{-1}\left(\frac{2\zeta_{z,n}\omega_n(2\omega_{vs})}{\omega_n^2 - (2\omega_{vs})^2}\right)$$

$$X_{ml,z} = \frac{f_{ml,z}}{\sqrt{\left(\omega_n^2 - (2\omega_{vs})^2\right)^2 + \left(2\zeta_{n,z}\omega_n(2\omega_{vs})\right)^2}} \text{ and}$$

$$\zeta_{n,z}=\frac{\gamma_z L}{2cn\pi\rho A},\ \omega_n=\frac{cn\pi}{L},\ f_{dl,z}=\frac{-F_{dl,z}}{\rho A},\ f_{ml,z}=\frac{F_{ml,z}}{\rho A}$$

A2.3. Forming the Total Solution

Therefore, the steady state solution of the nth modes response is:

$$w_{n,y}(x,t)=\sin\left(\frac{n\pi x}{L}\right)\left(X_{dl,n,y}\cos\left(\omega_{vs}t-\theta_{dl,n,y}\right)+X_{ml,n,y}\sin\left(\omega_{vs}t-\theta_{ml,n,y}\right)\right)$$

[A-49a]

$$w_{n,z}(x,t)=\sin\left(\frac{n\pi x}{L}\right)\left(X_{dl,n,z}\cos\left(\omega_{vs}t-\theta_{dl,n,z}\right)+X_{ml,n,z}\sin\left(\omega_{vs}t-\theta_{ml,n,z}\right)\right)$$

[A-49b]

Using the expansion theorem we calculate the full steady state solution to the problems as:

$$w_y(x,t)=\sum_{n=1}^{\infty}w_{n,y}(x,t)=$$
$$\sum_{n=1}^{\infty}\left[\sin\left(\frac{n\pi x}{L}\right)\left(X_{dl,n,y}\cos\left(\omega_{vs}t-\theta_{n,y}\right)+X_{ml,n,y}\sin\left(\omega_{vs}t-\theta_{n,y}\right)\right)\right]$$

[A-50a]

$$w_z(x,t)=\sum_{n=1}^{\infty}w_{n,z}(x,t)=$$
$$\sum_{n=1}^{\infty}\left[\sin\left(\frac{n\pi x}{L}\right)\left(X_{dl,n,z}\cos\left(2\omega_{vs}t-\theta_{n,z}\right)+X_{ml,n,z}\sin\left(2\omega_{vs}t-\theta_{n,z}\right)\right)\right]$$

[A-50b]

For this problem, convergence of the expansion theorem did occur as:

$$\lim_{n\to\infty}X_{ml,dl}=0$$ [A-51]

Therefore, the expansion theorem can be used in these cases.

A2.4. General Notes on the Solution

From the 2-D VIV data of Zhou et al (2000), it is apparent that $f_{dl} << f_{ml}$ in the frequency range under consideration in this paper. Hence, the vibration responses plotted will be dominated by the inertia forces and the result will appear to the same as simple harmonic model (Blevins, 1990). In addition, the watertight fittings impart little structural damping and $\zeta_n \approx 0$ in both directions hence $\theta_n \approx 0$. Hence, the existence of mode shape $X_n(x)$ is highly dependent upon the proximity of $\omega_{vs}{}^2$ to that modes natural frequency $\omega_n{}^2$. This is seen in equation A-48 due to their relationship of these terms in the denominator of X_{ml} and X_{dl}.

The solution presented above can be converted to a rigid cylinder by summing between n=1 to 1 with:

$$X_{n,rigid}(x) = 1,\ \zeta = \frac{\gamma}{2m\omega_1},\ \omega_n = \omega_1 = \sqrt{\frac{k}{m}},\ f_{dl} = \frac{-F_{dl}}{m},\ f_{ml} = \frac{F_{ml}}{m}.$$

However, if the cylinder was mounted with uneven stiffness on the top or bottom mountings it would be possible to have a second, rotational mode. With such a design one could possibly reproduce vibration nodes on a rigid cylinder and potentially reproduce the results of this study.

References

Blevins RD (1990) Flow-Induced Vibration: Second edition. Von Nostrand Reinhold, New York.

Inman DJ (2001) Engineering Vibration: Second Edition, Prentice Hall, New Jersey pp.432-434.

Jauvtis N, Williamson CHK (2004) The Effect of two Degrees of Freedom on Vortex-Induced Vibration at Low Mass and Damping. J. Fluid Mechanics 509:23-62.

Sarpkaya T (1978) Fluid Forced on Oscillating Cylinders. J. of the waterway port coastal and ocean division WW4:275-290.

Sarpkaya T (2004) A critical review of the intrinsic nature of vortex-induced vibrations. J. Fluids and Structures 19:389-447.

Wilden RHJ, Graham JMR (2006) Three distinct response regimes for the transverse Vortex-Induced Vibrations of circular cylinders at low Reynolds numbers. J. Fluids and Structures 22:885-895.

Willden RHJ, Graham JMR (2001) Numerical prediction of VIV on long flexible circular cylinders. J. Fluids and Structures 15:659-669.

Appendix B. Unsteady Bernoulli Equation and Fluid Dynamic Similarity

In this section we develop an unsteady Bernoulli equation model for the tubing network which conveys the actuation flows from the actuator to the step. This model is used to design a fluid dynamically similar extra tube reservoir which will have minimal effect on the velocity of tubes connected to the step.

B.1. The Unsteady Bernoulli Equation

As with the use of the steady Bernoulli equation there are a few assumptions. Flow is inviscid, or is along a streamline. The unsteady Bernoulli equation between two arbitrary points A and B along a stream-line is written as:

$$P_A + \frac{\rho V_A^2}{2} + \rho g y_A = P_B + \frac{\rho V_B^2}{2} + \rho g y_b + \rho \int_A^B \frac{\partial V}{\partial t} ds \qquad \text{[B-1]}$$

The static pressure (P), the dynamic ($\rho V^2/2$) and hydrostatic pressures ($\rho g y$) are typical terms seen in the steady Bernoulli Equation, but here they are dependent on time. The new integral term is the pressure associated with fluid acceleration. We will find that this will dominate the pressure associated with actuating the tubing network.

If we write the unsteady Bernoulli equation along a stream-line between the actuator (A) and a point t_n in the bulk flow of the test section we get

$$P_A(t) + \frac{\rho V_A^2(t)}{2} + \rho g y_A = P_{tn} + \frac{\rho V_{tn}^2}{2} + \rho g y_{tn} + \rho \int_A^{tn} \frac{\partial V}{\partial t} ds \qquad \text{[B-2]}$$

Due to the relative areas of the test section to the plunger area, there is very little change in the test section velocity V_{tn} resulting from the actuation V_A. Also, time fluctuations the level y_A is not significantly affected by the rate of change of volume in the syringes. From the steady Bernoulli equation applied between the inviscid flow points 1 and tn in Figure B.2 we get:

$$P_{tn} = \frac{\rho V_1^2 - V_{tn}^2}{2} - \rho g y_{tn} \qquad \text{[B-3]}$$

Under actuated conditions y_a and y_r are slightly time dependent. Such time dependencies are due to the rate of change of volume in the syringes. These volume fluctuations are not significant enough to the free surface levels of the tunnel or reservoir. Hence, the mean values for y_a and y_r as determined through the hydrostatic pressure relation adequately describe their values during actuation:

$$\rho g y_{a,r} = P_{tn} + \rho g y_{tn} = \frac{\rho\left(V_1^2 - V_{tn}^2\right)}{2} \qquad \text{[B-4]}$$

Substituting the values for $\rho g y_A$ and P_{tn} into equation B-2 we get:

$$P_A(t)+\frac{\rho V_A^2(t)}{2}=\rho\int_A^{tn}\frac{\partial V}{\partial t}ds \qquad \text{[B-5]}$$

Similarly, the unsteady Bernoulli equation along a stream-line between the actuator (A) and the free surface of the reservoir is:

$$P_A(t)+\frac{\rho V_A^2(t)}{2}+\rho g y_A=\rho g y_r+\rho\int_A^{r}\frac{\partial V}{\partial t}ds$$

Simplifying using equation B-4 we get:

$$P_A(t)+\frac{\rho V_A^2(t)}{2}=\rho\int_A^{r}\frac{\partial V}{\partial t}ds \qquad \text{[B-6]}$$

Next we have to decompose the acceleration integral based on the various components of the tubing network.

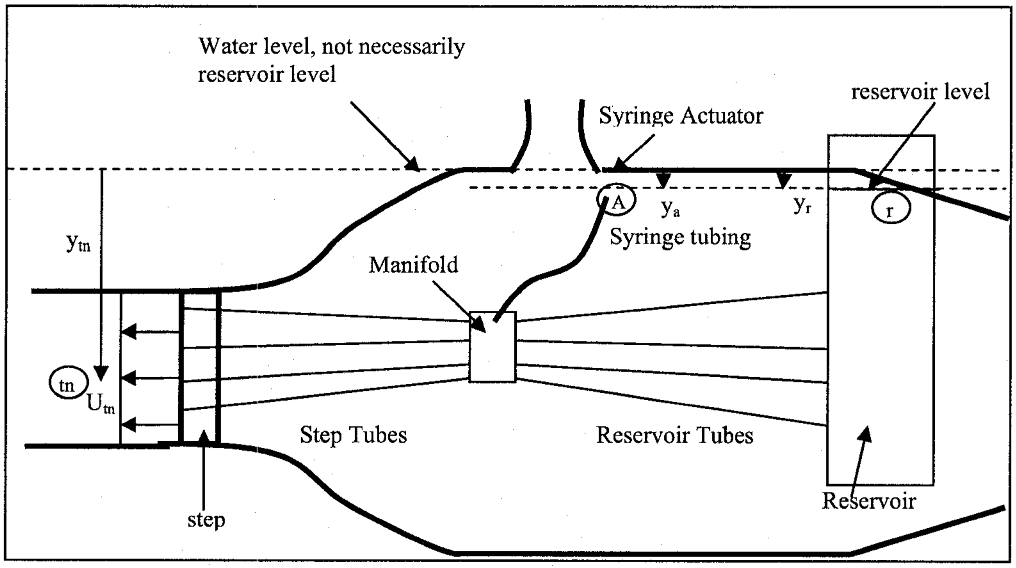

Figure B.1. Schematic of the Tubing network for 1 actuator

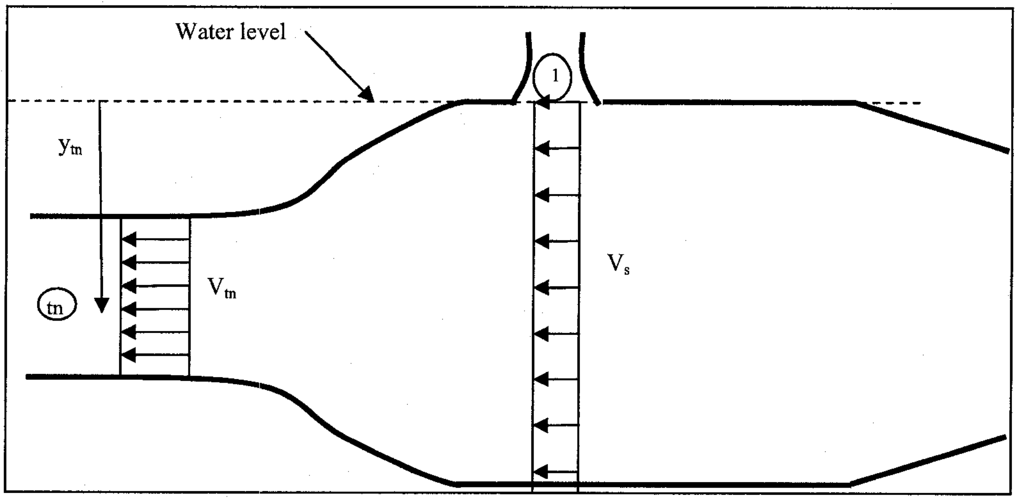

Figure B.2. Schematic of bulk Flow in the Water Tunnel

B.2. The Acceleration Term

The acceleration terms of the step network and the reservoir network are:

$$\rho\int_{A}^{tn}\frac{\partial V_s}{\partial t}ds \text{ and } \rho\int_{A}^{r}\frac{\partial V_r}{\partial t}ds.$$

They are line integrals over the entire length of streamline in the respective cases. To solve for this we break the streamline up into components. The step tube network is broken up into 13 components, and the reservoir is broken up into 14 components. Components are broken up into lengths of equal flow area and are always separated by a local change in area and flow velocity. The components are shown visually in the tubing network schematic in Figure B.3. This schematic is not to scale and the locations of components does not indicate actual experimental placement. The symbols for this schematic are described in Table B.1. Therefore we can split up the acceleration integrals into:

$$\rho\int_{A}^{tn}\frac{\partial V_s}{\partial t}ds=\sum_{j}^{12}\int_{j}^{j+1}\frac{\partial V_{j,s}}{\partial t}ds \text{ and } \rho\int_{A}^{r}\frac{\partial V_r}{\partial t}ds=\sum_{j}^{13}\int_{j}^{j+1}\frac{\partial V_{j,r}}{\partial t}ds$$

Where j denotes the component of interest where the integral is evaluated.

For the flow within a given component we further assume that the velocity is a function of time only, and not the streamline coordinate s. Therefore the integral simplifies to:

$$\int\frac{\partial V}{\partial t}ds\approx\frac{dV}{dt}\int ds$$

An assumption that is not necessarily accurate for the very short length components. For the longer lengths, which dominate the acceleration term, this assumption should be reasonable. This is because the flow within the short length component is more greatly influenced by the turbulence at its end connections. Larger length components are more greatly isolated from these end conditions and less error would be expected in this assumption.

With this assumption, the acceleration integral can be written as:

$$\rho\int_{A}^{tn}\frac{\partial V_s}{\partial t}ds=\sum_{j}^{12,s}\frac{dV_j}{dt}\int_{j}^{j+1}ds=\sum_{j}^{12,s}\frac{dV_j}{dt}L_j \text{ and}$$

$$\rho\int_{A}^{r}\frac{\partial V_r}{\partial t}ds=\sum_{j}^{13,r}\frac{dV_j}{dt}\int_{j}^{j+1}ds=\sum_{j}^{13,r}\frac{dV_j}{dt}L_j \qquad \text{[B-7]}$$

The velocity of the syringe is prescribed as $V_A(t)$. Such functions are typically differentiable giving dV_A/dt. Through continuity we can calculate the velocity in any component of the tubing network. For tubes between the syringe and the manifold the component velocities and accelerations of both the step and reservoir networks are:

$$V_j=V_A\frac{A_A}{A_j} \text{ and } \frac{dV_j}{dt}=\frac{dV_A}{dt}\frac{A_A}{A_j} \qquad \text{[B-8]}$$

After the manifold a branch flow coefficient must be introduced for the step tubes (c_s) and for the reservoir tubes (c_r) since the designs are not necessarily equal. The ideal value of these branch coefficients is 1/8, where 8 is the number of outlets on the manifold. The flow-rate in each branch can be related to the syringe actuation flow-rate by:

$$Q_{branch}=c_{s,r}V_AA_A=V_{j,s,r}A_{j,s,r} \qquad \text{[B-9]}$$

This branch equation gives the following relationship for the j^th^ components velocity in the branch:

$$V_{j,s,r}=c_{s,r}V_A\frac{A_A}{A_{j,s,r}}$$

Differentiating we get

$$\frac{dV_j}{dt}=c_{s,r}\frac{dV_A}{dt}\frac{A_A}{A_j}=c_{s,r}\frac{dV_A}{dt}\frac{A_A}{A_j}+\frac{dc_{s,r}}{dt}V_A\frac{A_A}{A_j}$$

Although we will not show the details, keeping the derivative of the branch flow coefficient results in a problem where must solve 1st order ordinary differential equation with variable coefficients to determine c_s and c_r. This problem was solved using the power series method and it showed that dc/dt is very small and periodic. Hence the fluid acceleration terms for the components after the branch can be written as:

$$\frac{dV_j}{dt} = c_{s,r} V_A \frac{A_A}{A_j} \qquad \text{[B-10]}$$

Therefore the fluid acceleration summations for the step and reservoir are:

$$\rho \int_A^{tn} \frac{\partial V_s}{\partial t} ds = \rho \frac{dV_A(t)}{dt} \left[\sum_{j=1}^{5,s} \frac{A_A}{A_j} L_j + \sum_{6}^{12,s} \frac{A_A}{A_j} L_j c_s + \sum_{13}^{13,s} \frac{A_A}{A_j} L_j \right] \qquad \text{[B-11]}$$

$$\rho \int_A^{r} \frac{\partial V_r}{\partial t} ds = \rho \frac{dV_A(t)}{dt} \left[\sum_{j=1}^{5,r} \frac{A_A}{A_j} L_j + \sum_{6}^{12,r} \frac{A_A}{A_j} L_j c_r + \sum_{13}^{14,r} \frac{A_A}{A_j} L_j \right] \qquad \text{[B-12]}$$

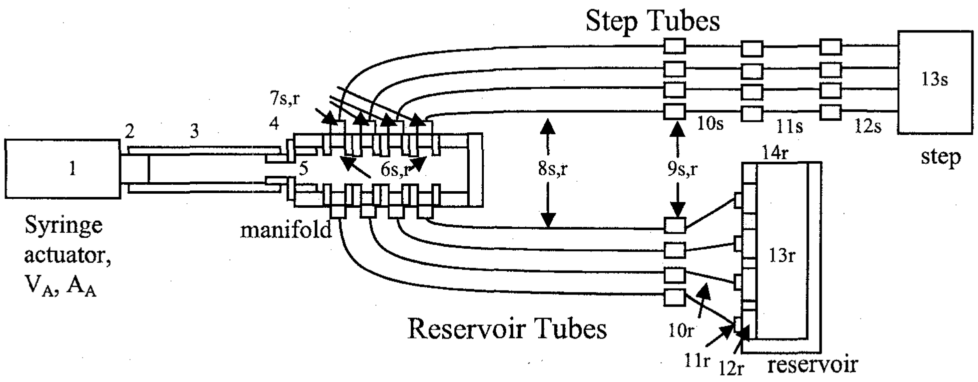

Figure B.3. Components of the Tubing Networks

Location (j)	Diameter	Length	Cr,Cs	description
Both Step and Reservoir Step tubes				
1	D_A or D_1	L_1	1	Syringe ID
2	D_2	L_2	1	Syringe Luer lock ID
3	D_3	L_3	1	3/8" tubing ID
4	D_4	L_4	1	Barbed fitting ID
5	D_5	L_5	1	Threaded fitting ID
6s,r	D_6	L_6	Cr,Cs	Threaded fitting ID
7s,r	D_7	L_7	Cr,Cs	Barbed fitting ID
8s,r	D_8	L_8	Cr,Cs	1/8" tubing ID
9s,r	D_9	L_9	Cr,Cs	1/8" to 3/32" barbed fitting ID
10s,r	D_{10}	L_{10}	Cr,Cs	3/32" tubing ID
Step Specific tube				
11s	$D_{11,s}$	$L_{11,s}$	Cs	3/32" OD Stainless steel tube
12s	$D_{12,s}$	$L_{12,s}$	Cs	Rectangular Actuation Slot
Reservoir Specific tube				
11r	$D_{11,r}$	$L_{11,r}$	Cr	Barbed fitting ID
12r	$D_{12,r}$	$L_{12,r}$	Cr	Threaded fitting ID
13r	$D_{13,r}$	$L_{13,r}$	Cr	Reservoir

Table B.1. Symbols for components in the Tubing Networks

B.3. Solution to the Branch Flow Coefficients c_s and c_r

Now we have 3 unknowns for which to solve, these unknowns are $P_A(t)$, c_s and c_r. When we subtract the one of the Bernoulli equations from the other we eliminate $P_A(t)$ and get:

$$0 = \rho \int_A^{tn} \frac{\partial V_s}{\partial t} ds - \rho \int_A^{r} \frac{\partial V_r}{\partial t} ds$$

By expanding the acceleration integral as derived in the previous section we get:

$$0 = \rho \frac{dV_A(t)}{dt} \left[\sum_{j=1}^{5,s} \frac{A_A}{A_j} L_j + \sum_{6}^{12,s} \frac{A_A}{A_j} L_j c_s + \sum_{13}^{13,s} \frac{A_A}{A_j} L_j \right]$$
$$-\rho \frac{dV_A(t)}{dt} \left[\sum_{j=1}^{5,r} \frac{A_A}{A_j} L_j + \sum_{6}^{12,r} \frac{A_A}{A_j} L_j c_r + \sum_{13}^{14,r} \frac{A_A}{A_j} L_j \right]$$

Simplifying we get:

$$0 = \left[+\sum_{6}^{12,s} \frac{A_A}{A_j} L_j c_s + \frac{A_A}{A_{13,s}} L_{13,s} \right] - \left[\sum_{6}^{12,r} \frac{A_A}{A_j} L_j c_r + \sum_{13}^{14,r} \frac{A_A}{A_j} L_j \right] \qquad \text{[B-13]}$$

We can use the branch flow-rate relation of Equation B-9 to write the full continuity relation:

$V_A A_A = N_s c_s V_A A_A + N_r c_r V_A A_A$ which simplifies to:

$$1 = N_s c_s + N_r c_r \text{ or } c_s = \frac{1 - N_r c_r}{N_s} \qquad \text{[B-14]}$$

Where N_s and N_r are the number of tubes connected to the step and reservoir respectively. $N_s + N_r \equiv 8$ for our design.

Equation B-13 together with Equation B-14 gives a 2 equation system of linear equations with 2 unknowns.

Solving this system for c_s and c_r give:

$$c_r = \frac{\sum_{6}^{12,s} \frac{A_A}{A_j} L_j - N_s \sum_{13}^{14,r} \frac{A_A}{A_j} L_j}{N_s \sum_{6}^{12,r} \frac{A_A}{A_j} L_j + N_r \sum_{6}^{12,s} \frac{A_A}{A_j} L_j} \qquad \text{[B-15]}$$

$$c_s = \frac{\sum_{6}^{12,r} \frac{A_A}{A_j} L_j + N_r \sum_{13}^{14,r} \frac{A_A}{A_j} L_j}{N_s \sum_{6}^{12,r} \frac{A_A}{A_j} L_j + N_r \sum_{6}^{12,s} \frac{A_A}{A_j} L_j} \qquad \text{[B-16]}$$

B.4. Fluid Dynamic Similarity

To force c_s to be very close to its ideal value we must ensure the following conditions occur.

$$\sum_{13}^{14,r} \frac{A_A}{A_j} L_j \approx 0 \qquad \text{[B-17]}$$

$$\sum_{6}^{12,r} \frac{A_A}{A_j} L_j = \sum_{6}^{12,s} \frac{A_A}{A_j} L_j \qquad \text{[B-18]}$$

To satisfy the condition in [B-17], we simply select the area of the reservoir A_j to be very large relative compared with the area of the syringe piston A_A. To satisfy the condition in [B-18] we can cut the 3/32 inch reservoir tubes a slightly different length than the step tubes.

An equation for the required length of reservoir 3/32 inch tubing can be derived from the condition as:

$$L_{10,r} = \frac{A_{10,r}}{A_A} \left(\sum_{j=6,s}^{12,s} \frac{A_A}{A_j} L_j - \sum_{j=6,r;j \neq 10,r}^{12,r} \frac{A_A}{A_j} L_j \right) \qquad \text{[B-19]}$$

Appendix C: Backward-Facing Step Assembly Drawings

In this appendix, we present assembly drawings for the various components of the experiment. In this section we will not denote drawings as figures. Instead, we will use the commonly used drafting convention of giving each plot and a drawing name. Although it is not recommended by the Faculty of Graduate Studies and Research at the University of Alberta, landscaped paper format is also chosen for the display of engineering drawings, as it is the standard method for displaying orthographic projections of 3 dimensional objects.

Drawings in this Appendix:

Total Assem 1, Total Step Assembly

This drawing shows the connection of the watertight window assembly to the step module. This drawing also shows the insertion of the hydrogen bubble wire attachment.

Total Assem 2, Step Assembly Details

This drawing shows the connection of the solid step spline portion with the dye reservoir assembly (Dye Res 1) and the actuator slot assembly (Slot 1). It also shows the spacing between the bolts used in the attachment of the various components

Window 1, Window Assembly

In this drawing the details for connecting the actuator tubing are given and the methods for creating a watertight test section window are explained.

Dye Res 1, Dye Reservoir Assembly

The details for assembling the dye reservoir are given in this drawing. It also specifies the nominal dye slot width.

Slot 1, Actuator Assembly

The various pieces of the actuator slots are shown in this drawing. The slots are created by milling 128 channels approximately 2.5 mm in width by 1 mm deep. The slots are then covered with a double sided adhesive tape to prevent water from moving between adjacent slots. A sealing plate applies pressure to the tape.

RAP 1, Rack and Pinion Assembly

This drawing shows the various components of the rack and pinion actuator used to create the time dependent fluid actuation velocities.

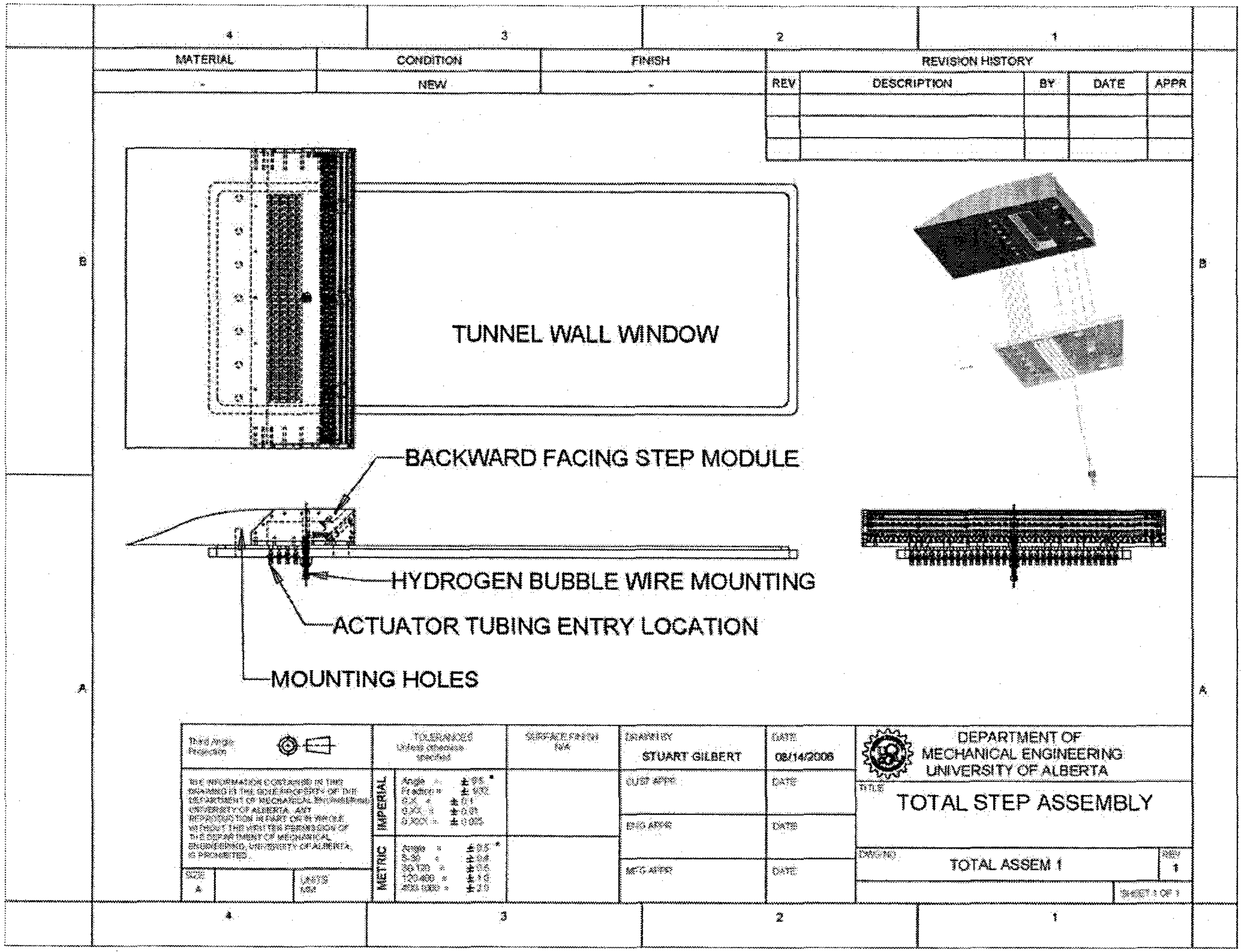

MATERIAL	CONDITION	FINISH
-	NEW	-

REVISION HISTORY

REV	DESCRIPTION	BY	DATE	APPR

DRAWN BY	STUART GILBERT
DATE	08/14/2006
CUST APPR	
DATE	
ENG APPR	
DATE	
MFG APPR	
DATE	

Third Angle Projection

TOLERANCES Unless otherwise specified

SURFACE FINISH N/A

SIZE A

UNITS MM

DEPARTMENT OF
MECHANICAL ENGINEERING
UNIVERSITY OF ALBERTA

TITLE: TOTAL STEP ASSEMBLY

DWG NO: TOTAL ASSEM 1

REV 1

SHEET 1 OF 1

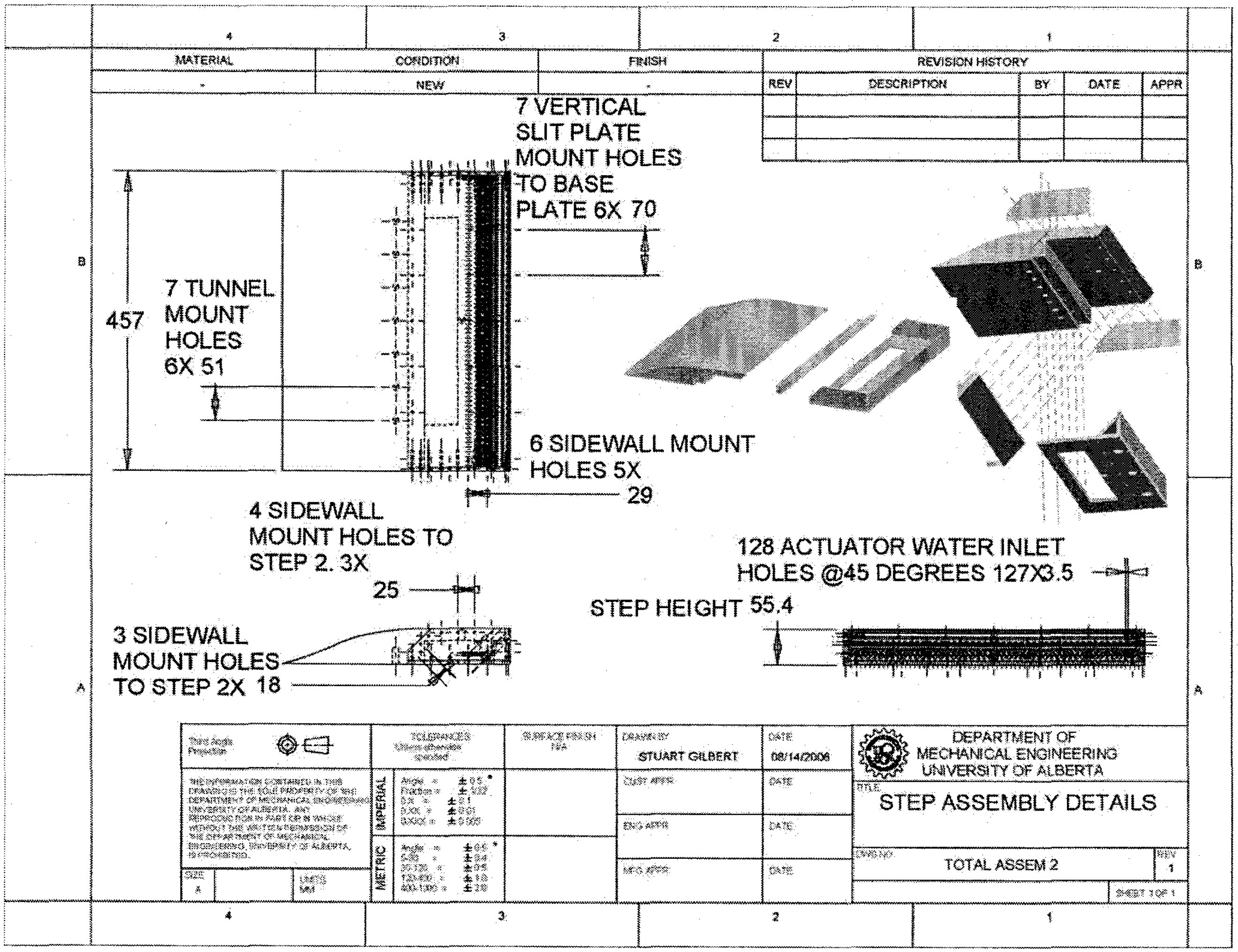
4
3
2
1
MATERIAL
-
CONDITION
NEW
FINISH
-
REVISION HISTORY
REV
DESCRIPTION
BY
DATE
APPR
B
A
7 VERTICAL SLIT PLATE MOUNT HOLES TO BASE PLATE 6X 70
457
7 TUNNEL MOUNT HOLES 6X 51
6 SIDEWALL MOUNT HOLES 5X
29
4 SIDEWALL MOUNT HOLES TO STEP 2. 3X
25
128 ACTUATOR WATER INLET HOLES @45 DEGREES 127X3.5
STEP HEIGHT 55.4
3 SIDEWALL MOUNT HOLES TO STEP 2X 18
Third Angle Projection
TOLERANCES
Unless otherwise specified
SURFACE FINISH
N/A
DRAWN BY
STUART GILBERT
DATE
08/14/2006
CUST APPR
DATE
ENG APPR
DATE
MFG APPR
DATE
IMPERIAL
METRIC
SIZE
A
UNITS
MM
DEPARTMENT OF MECHANICAL ENGINEERING UNIVERSITY OF ALBERTA
TITLE
STEP ASSEMBLY DETAILS
DWG NO
TOTAL ASSEM 2
REV
1
SHEET 1 OF 1

MATERIAL	CONDITION	FINISH
-	NEW	-

REVISION HISTORY				
REV	DESCRIPTION	BY	DATE	APPR

NOTES:
1) BARBED FITTINGS SURROUNDED BY GASKET OR SILICON SEALING AGENT TO ENSURE A WATERTIGHT WALL

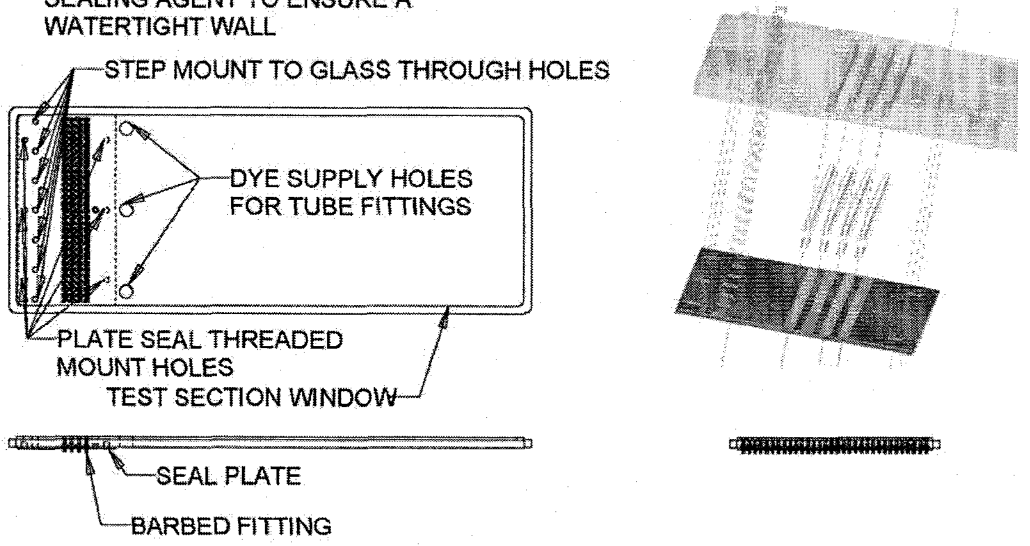

Third Angle Projection	TOLERANCES Unless otherwise Specified	SURFACE FINISH N/A	DRAWN BY STUART GILBERT	DATE 08/14/2006
THE INFORMATION CONTAINED IN THIS DRAWING IS THE SOLE PROPERTY OF THE DEPARTMENT OF MECHANICAL ENGINEERING UNIVERSITY OF ALBERTA. ANY REPRODUCTION IN PART OR IN WHOLE WITHOUT THE WRITTEN PERMISSION OF THE DEPARTMENT OF MECHANICAL ENGINEERING, UNIVERSITY OF ALBERTA, IS PROHIBITED.	IMPERIAL Angle = ± 0.5 ° Fraction = ± 1/32 0.X = ± 0.1 0.XX = ± 0.01 0.XXX = ± 0.005		CUST APPR	DATE
			ENG APPR	DATE
SIZE A UNITS MM	METRIC Angle = ± 0.5 ° 5-30 = ± 0.4 30-120 = ± 0.5 120-400 = ± 1.0 400-1000 = ± 2.0		MFG APPR	DATE

DEPARTMENT OF
MECHANICAL ENGINEERING
UNIVERSITY OF ALBERTA

TITLE
WINDOW ASSEMBLY

DWG NO. WINDOW 1
REV 1
SHEET 1 OF 1

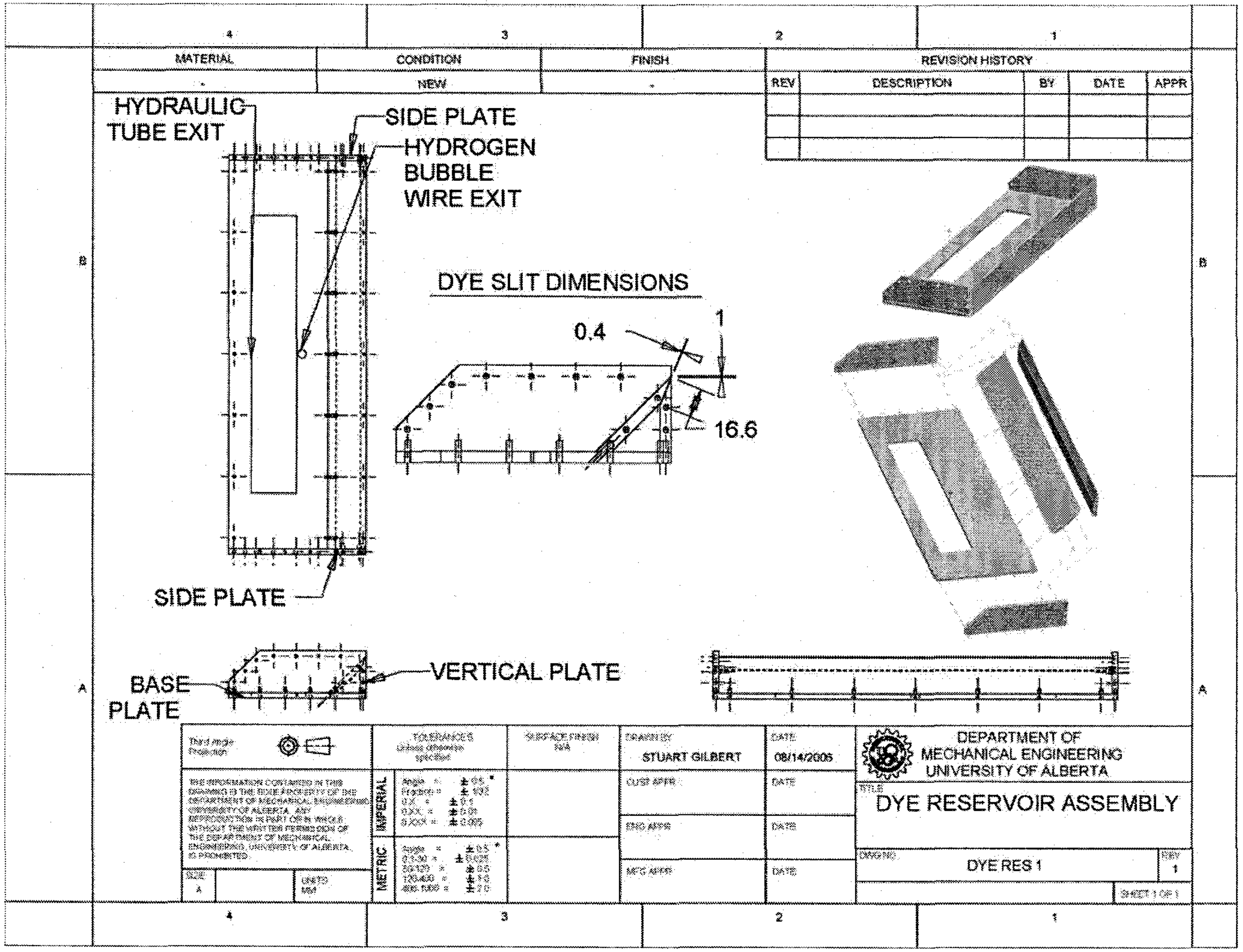

MATERIAL	CONDITION	FINISH
-	NEW	-

REVISION HISTORY

REV	DESCRIPTION	BY	DATE	APPR

THE INFORMATION CONTAINED IN THIS DRAWING IS THE SOLE PROPERTY OF THE DEPARTMENT OF MECHANICAL ENGINEERING, UNIVERSITY OF ALBERTA. ANY REPRODUCTION IN PART OR IN WHOLE WITHOUT THE WRITTEN PERMISSION OF THE DEPARTMENT OF MECHANICAL ENGINEERING, UNIVERSITY OF ALBERTA, IS PROHIBITED.

TOLERANCES Unless otherwise specified

IMPERIAL
Angle = ± 0.5 °
Fraction = ± 1/32
0.X = ± 0.1
0.XX = ± 0.01
0.XXX = ± 0.005

METRIC
Angle = ± 0.5 °
0.1-30 = ± 0.025
30-120 = ± 0.5
120-400 = ± 1.0
400-1000 = ± 2.0

SURFACE FINISH N/A

SIZE A

UNITS MM

DRAWN BY STUART GILBERT

DATE 08/14/2005

CUST APPR

DATE

ENG APPR

DATE

MFG APPR

DATE

DEPARTMENT OF MECHANICAL ENGINEERING
UNIVERSITY OF ALBERTA

TITLE DYE RESERVOIR ASSEMBLY

DWG NO. DYE RES 1

REV 1

SHEET 1 OF 1

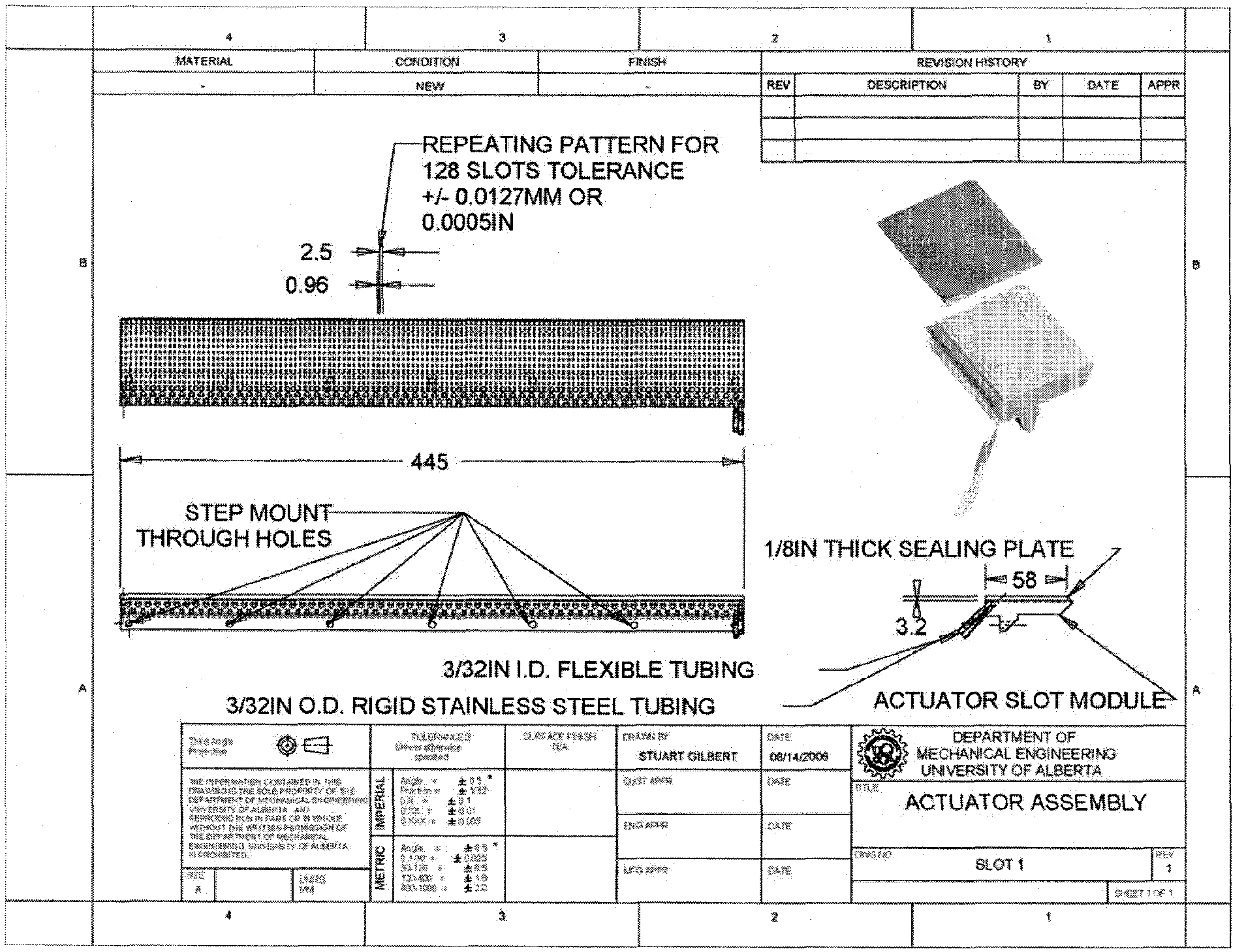
4
3
2
1
MATERIAL
-
CONDITION
NEW
FINISH
-
REVISION HISTORY
REV
DESCRIPTION
BY
DATE
APPR
REPEATING PATTERN FOR 128 SLOTS TOLERANCE +/- 0.0127MM OR 0.0005IN
2.5
0.96
B
445
STEP MOUNT THROUGH HOLES
1/8IN THICK SEALING PLATE
58
3.2
3/32IN I.D. FLEXIBLE TUBING
3/32IN O.D. RIGID STAINLESS STEEL TUBING
ACTUATOR SLOT MODULE
A
Third Angle Projection
TOLERANCES
IMPERIAL
METRIC
DRAWN BY
STUART GILBERT
DATE
08/14/2006
DATE
DATE
DATE
DEPARTMENT OF MECHANICAL ENGINEERING UNIVERSITY OF ALBERTA
TITLE
ACTUATOR ASSEMBLY
DWG NO.
SLOT 1
REV
1
SHEET 1 OF 1

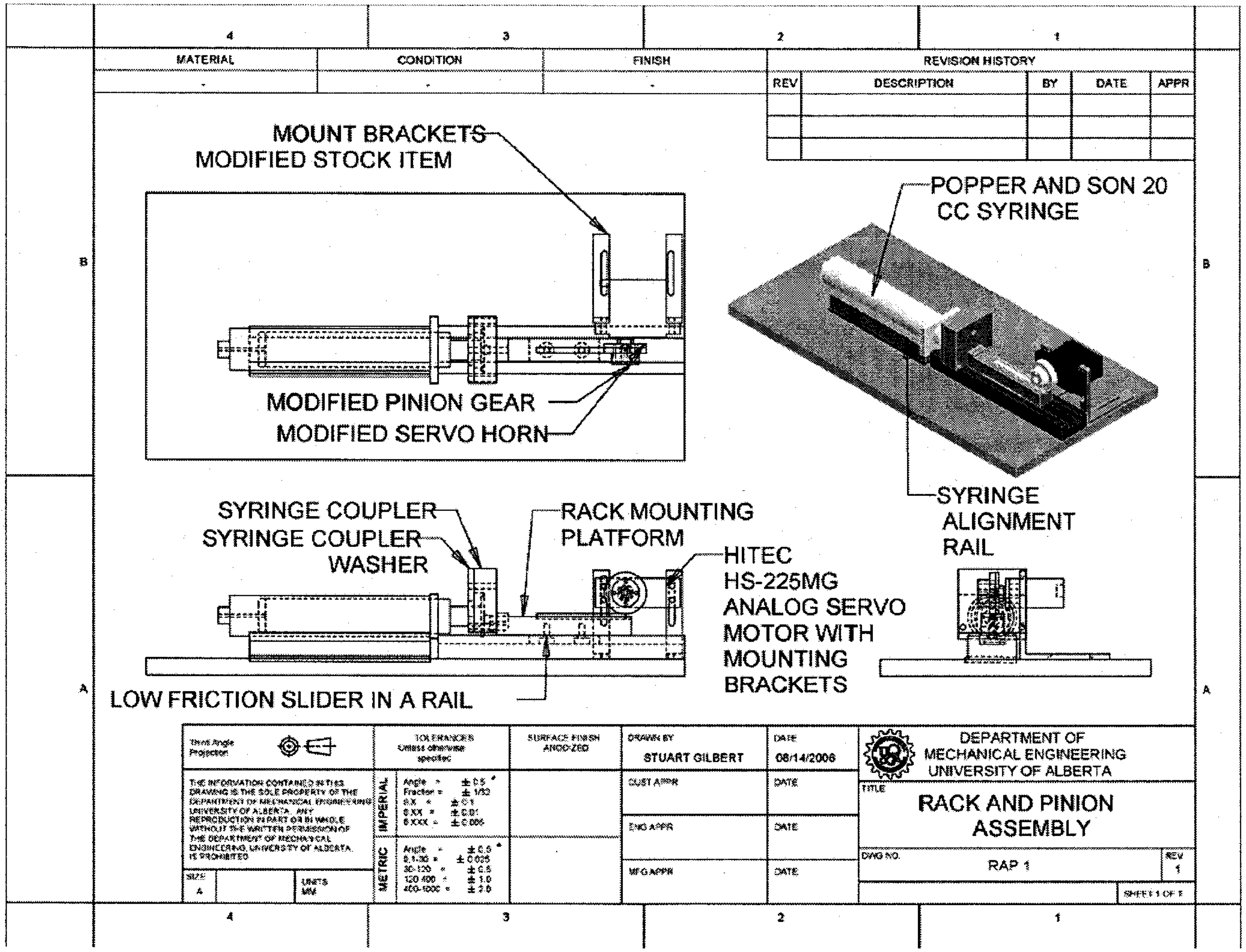
4
3
2
1
MATERIAL
CONDITION
FINISH
REVISION HISTORY
REV
DESCRIPTION
BY
DATE
APPR
MOUNT BRACKETS
MODIFIED STOCK ITEM
POPPER AND SON 20 CC SYRINGE
B
MODIFIED PINION GEAR
MODIFIED SERVO HORN
SYRINGE ALIGNMENT RAIL
SYRINGE COUPLER
SYRINGE COUPLER WASHER
RACK MOUNTING PLATFORM
HITEC HS-225MG ANALOG SERVO MOTOR WITH MOUNTING BRACKETS
A
LOW FRICTION SLIDER IN A RAIL
Third Angle Projection
TOLERANCES Unless otherwise specified
SURFACE FINISH ANODIZED
DRAWN BY
STUART GILBERT
DATE
08/14/2006
DEPARTMENT OF MECHANICAL ENGINEERING UNIVERSITY OF ALBERTA
THE INFORMATION CONTAINED IN THIS DRAWING IS THE SOLE PROPERTY OF THE DEPARTMENT OF MECHANICAL ENGINEERING UNIVERSITY OF ALBERTA. ANY REPRODUCTION IN PART OR IN WHOLE WITHOUT THE WRITTEN PERMISSION OF THE DEPARTMENT OF MECHANICAL ENGINEERING, UNIVERSITY OF ALBERTA IS PROHIBITED
IMPERIAL
Angle = ± 0.5°
Fraction = ± 1/32
0.X = ± 0.1
0.XX = ± 0.01
0.XXX = ± 0.005
METRIC
Angle = ± 0.5°
0.1-30 = ± 0.025
30-120 = ± 0.5
120-400 = ± 1.0
400-1000 = ± 2.0
CUST APPR
DATE
ENG APPR
DATE
MFG APPR
DATE
TITLE
RACK AND PINION ASSEMBLY
DWG NO.
RAP 1
REV
1
SIZE
A
UNITS
MM
SHEET 1 OF 1